Oil & Natural Gas Technology

Geomechanical Performance of Hydrate-Bearing Sediment in Offshore Environments

Final Scientific/Technical Report

Start date 10/01/05
End date 03/31/08

Principal Authors
Stephen A. Holditch – Texas A&M University
Tad Patzek – University of California, Berkeley
Jonny Rutqvist and George Moridis – Lawrence Berkeley National Laboratory
Richard Plumb – Schlumberger

July 2008
Revised November 2008

DOE Award No.: DE-FC26-05NT42664
CFDA Number: 81.089 (Fossil Energy Research and Development)

Submitted by:
Texas Engineering Experiment Station
3000 TAMU
College Station, TX 77843-3000

Prepared for:
United States Department of Energy
National Energy Technology Laboratory

Office of Fossil Energy

GEOMECHANICAL PERFORMANCE OF HYDRATE-BEARING SEDIMENTS IN OFFSHORE ENVIRONMENTS

Final Scientific/Technical Report

Start date 10/01/05
End date 03/31/08

Principal Authors
Stephen A. Holditch – Texas A&M University
Tad Patzek – University of California, Berkeley
Jonny Rutqvist and George Moridis – Lawrence Berkeley National Laboratory
Richard Plumb – Schlumberger

July 2008
Revised November 2008

DOE Award Number: DE-FC26-05NT42664
CFDA Number: 81.089 (Fossil Energy Research and Development)

Submitted by:
Texas Engineering Experiment Station
3000 TAMU
College Station, TX 77843-3000

Prepared for:
United States Department of Energy
National Energy Technology Laboratory

TABLE OF CONTENTS

Disclaimer

Abstract

The objective of this multi-year, multi-institutional research project was to develop the knowledge base and quantitative predictive capability for the description of geomechanical performance of hydrate-bearing sediments (hereafter referred to as HBS) in oceanic environments. The focus was on the determination of the envelope of hydrate stability under conditions typical of those related to the construction and operation of offshore platforms. We have developed a robust numerical simulator of hydrate behavior in geologic media by coupling a reservoir model with a commercial geomechanical code. We also investigated the geomechanical behavior of oceanic HBS using pore-scale models (conceptual and mathematical) of fluid flow, stress analysis, and damage propagation.

The objective of the UC Berkeley work was to develop a grain-scale model of hydrate-bearing sediments. Hydrate dissociation alters the strength of HBS. In particular, transformation of hydrate clusters into gas and liquid water weakens the skeleton and, simultaneously, reduces the effective stress by increasing the pore pressure. The large-scale objective of the study is evaluation of geomechanical stability of offshore oil and gas production infrastructure.

At Lawrence Berkeley National Laboratory (LBNL), we have developed the numerical model TOUGH + Hydrate + FLAC3D to evaluate how the formation and disassociation of hydrates in seafloor sediments affects seafloor stability. Several technical papers were published using results from this model. LBNL also developed laboratory equipment and methods to produce realistic laboratory samples of sediments containing gas hydrates so that mechanical properties could be measured in the laboratory. These properties are required to run TOUGH + Hydrate + FLAC3D to evaluate seafloor stability issues.

At Texas A&M University we performed a detailed literature review to determine what gas hydrate formation properties had been measured and reported in the literature. We then used TOUGH + Hydrate to simulate the observed gas production and reservoir pressure field data at Messoyakha. We simulated various scenarios that help to explain the field behavior. We have evaluated the effect of reservoir parameters on gas recovery from hydrates. Our work should be beneficial to others who are investigating how to produce gas from a hydrate capped gas reservoir. The results also can be used to better evaluate the process of producing gas from offshore hydrates.

The Schlumberger PETREL model is used in industry to the description of geologic horizons and the special distribution of properties. An interface between FLAC3D and Petrel was built by Schlumberger to allow for efficient data entry into TOUGH + Hydrate + FLAC3D.

LIST OF FIGURES

LIST OF TABLES

Executive Summary

The objective of this multi-year, multi-institutional research project was to develop the knowledge base and quantitative predictive capability for the description of geomechanical performance of hydrate-bearing sediments (hereafter referred to as HBS) in oceanic environments. The focus was on the determination of the envelope of hydrate stability under conditions typical of those related to the construction and operation of offshore platforms. We have developed a robust numerical simulator of hydrate behavior in geologic media by coupling a reservoir model with a commercial geomechanical code. We also investigated the geomechanical behavior of oceanic HBS using pore-scale models (conceptual and mathematical) of fluid flow, stress analysis, and damage propagation.

We used data from the literature and we conducted laboratory studies to generate data to (i) evaluate the conceptual pore-scale models, (ii) calibrate the mathematical models, (iii) determine dominant relations and critical parameters defining the geomechanical behavior of HBS, and (iv) establish relationships between the geomechanical status of HBS and the corresponding geophysical signature. Four organizations, Texas A&M University (TAMU), University of California at Berkeley (UCB), Lawrence Berkeley National Laboratory (LBNL), and Schlumberger (SLB), who were involved in this project..

Pore Scale Modeling by UCB

The objective of the UC Berkeley work was to develop a grain-scale model of hydrate-bearing sediments. Hydrate dissociation alters the strength of HBS. In particular, transformation of hydrate clusters into gas and liquid water weakens the skeleton and, simultaneously, reduces the effective stress by increasing the pore pressure. The large-scale objective of the study is evaluation of geomechanical stability of offshore oil and gas production infrastructure. The output of the micro-scale model described here will be used in the numerical simulations of coupled flow and rock mechanics at reservoir scale.

We modeled the mechanical deformation of HBS or, more generally, of a granular medium, by numerical simulations of a pack of elastic spherical grains. Although this approach cannot entirely displace laboratory tests as the ground truth, it offers some opportunities which may be not available otherwise. Grain-scale simulations provide unique insights into the processes and phenomena underlying the classical continuum-medium models.

A grain-scale model of granular material has been verified against available experimental data and numerical simulations by others. The model is based on the principle of quasi-static equilibrium, and uses physical parameters as input data, with no adjustments for calibration. Variational approach made possible development of efficient numerical algorithms.

After successful verification, the model has been applied to quantitative estimates of the impact of hydrate dissociation on the mechanical strength of hydrate-bearing sediments.

The results have been reported in journal publications, presented at a number of scientific conferences and invited seminars.

Summary of TOUGH+/FLAC3D Model Development by LBNL

Lawrence Berkeley National Laboratory researchers 1) submitted a topical report entitled "Approach to Forming Hydrate Bearing Samples in Fine-Grained Material", 2) designed and completed fabrication of a geomechanical properties and geophysical signature test cell, 3) tested seismic transducers to be used in the test cell, and 4) attended and made two presentations at the DOE Program Review.

The topical report entitled "Approach to Forming Hydrate Bearing Samples in Fine-Grained Material", summarized methods to make methane hydrate for the geomechanical tests to be performed, in the types of sediments recommended by Texas A&M University. These sediments were described as (1) 100% sand sized particles (100 microns), (2) 50% silt-sized particles (10 microns) mixed with 50% clay-sized particles (1 micron), and (3)100% clay sized particles.

The method proposed follows these steps and the method was accepted by DOE in July, 2007.

- Mix dry mineral components until visually homogeneous
- Add water using a pipette (for sand), by equilibrating in a humidified chamber (silt or clay), or by stirring in flakes of frost ice (samples containing clay) and mix thoroughly
- Pack moistened material into the sleeve
- Rapidly evacuate air from the sample
- Chill sample to the appropriate temperature
- Pressurize sample with methane gas, and monitor T, P until hydrate is formed.
- Saturate with water

Simulation of Gas Production from Hydrates Using TOUGH+Hydrate by TAMU

To simulate geomechanical stability in subsea hydrate bearing sediments, it is important to understand the fundamental concepts of gas production from gas hydrates or free gas zones beneath gas hydrates. The flow of gas and water are inherently coupled with the mechanical properties of the hydrate bearing sediments. To model a field scale geomechanical failure or response, one should clearly understand the field scale flow concepts in a hydrate bearing sediment.

Once the **TOUGH+Hydate** had the FLAC3D model added as a subroutine, we conducted simulation work to investigate how gas production from gas hydrate zones affects the formation mechanical properties and seafloor slope stability. To be certain we are simulating the gas flow from gas hydrate deposits correctly, we decided to use **TOUGH+Hydate** to analyze data from the one known gas hydrate field that has been

produced. As such, we used the **TOUGH+Hydrate** simulator to reproduce some important observations and pressure behavior at Messoyakha. Through our modeling study of Messoyakha, we evaluated different reservoir/rock properties which are important for response of hydrate bearing sediments/rocks. This study has actually helped us understand how to accurately model flow in hydrate bearing sediment.

We have used **TOUGH+Hydrate** to simulate the observed gas production and reservoir pressure field data at Messoyakha. We simulated various scenarios that help to explain the field behavior. We have evaluated the effect of various reservoir parameters on gas recovery from hydrates. Our work should be beneficial to others who are investigating how to produce gas from hydrate capped gas reservoir. We were able to generate results that are very similar to the reported flow rates and pressure behavior in the Messoyakha Field. The value of absolute permeability in the hydrate layer and the lower free gas layer substantially affects the continued dissociation of hydrates during shut-down. We also modeled the formation of secondary hydrates near the wellbore that can cause reduced gas flow rates. The important parameters affecting the gas production are the formation permeability in the gas layer, the effective gas vertical permeability in the hydrate layer, the location of the perforations, and the gas hydrate saturation.

Summary of Petrel-FLAC3D Data Exchange by Schlumberger

The PETREL model contained, among other things, the description of horizons and the special distribution of properties. An interface between FLAC3D and Petrel was built by Schlumberger to allow for efficient data entry into TOUGH + Hydrate + FLAC3D during Phase III of this project. However, Phase III was cancelled by the DOE.

Chapter 1 – Overview of the Project

Objective

The main objective of this research project has been to develop the knowledge base and quantitative predictive capability for the description of geomechanical performance of hydrate-bearing sediments in oceanic environments. There are two main areas where our geomechanics research results can be applied. First, we have developed a better understanding of how gas hydrate deposits affect seafloor stability under conditions typical of those related to the construction and operation of offshore platforms. Second, we have determined how the production of natural gas from hydrate deposits in deep water as an energy resource affects the mechanical stability of the seafloor and the development planning for such deposits.

Scope of Work

To achieve the objectives of the project, the following approach was employed:

- The geomechanical behavior of oceanic hydrate bearing sediments (hereafter referred to as HBS) was investigated using pore-scale models (conceptual and mathematical) of fluid flow, stress analysis, and damage propagation.

- Laboratory studies were conducted to (i) evaluate the conceptual pore-scale models, (ii) calibrate the mathematical models, (iii) determine dominant relations and critical parameters defining the geomechanical behavior of HBS, and (iv) establish relationships between the geomechanical status of HBS and the corresponding geophysical signature.

- A robust numerical simulator of hydrate behavior in geologic media was coupled with a commercial geomechanical code, thus developing a numerical code for the stability analysis of HBS under mechanical and thermal stresses.

- Numerical studies were conducted to analyze the HBS stability performance under conditions (i) representative of an offshore platform installation and operation, and (ii) typical of oceanic hydrate accumulations under production.

- A thorough literature review was done to document all of the reservoir and geologic data in the public domain for marine hydrate deposits that have been evaluated during recent scientific cruises.

- An evaluation of the reservoir mechanisms associated with the gas production from the Messoyahka gas hydrate reservoir was accomplished using the TOUGH + Hydrate model.

- An interface between FLAC3D and Petrel was built by Schlumberger to allow for efficient data entry into TOUGH + Hydrate + FLAC3D during Phase III of this project. However, Phase III has been cancelled by the DOE.

Project Participants

The project was managed by Dr. Stephen A. Holditch, the Head of the Department of Petroleum Engineering at Texas A&M University. There are 3 other organizations involved in this project. Lawrence Berkeley National Laboratory (LBNL) developed software and conducted laboratory measurements. Dr. George Moridis was the main participant at LBNL. The University of California at Berkeley (UCB) developed pore scale models using the discrete element method. The work at UCB was under the direction of Dr. Tad Patzek. Schlumberger was our industry participant and their work was lead by Dr. Richard Plumb with the assistance of Pat Hooyman. Schlumberger provided in-kind contributions to include manpower, data and software.

List of Individual Tasks by Phase

PHASE I (Budget Period I) – Initial Fundamental Studies and Model Development

Task 1.0 – Research management plan
Task 2.0 – Technology Status Assessment
Task 3.0 – Fundamental Studies Part I
Subtask 3.1 - Fundamental studies of pore-scale geomechanical behavior of hydrates in porous media
Subtask 3.2 Development of Interface between Petrel and FLAC3D
Subtask 3.3 – Description of hydrate-bearing zones as documented by the Ocean Drilling Program and the Chevron-DOE Gulf of Mexico JIP to determine typical gas hydrate bearing sample characteristics
Task 4.0 – Development of the coupled geomechanical numerical model

Milestones for Phase I

TAMU	Compile literature survey on typical sediments containing gas hydrates in the ocean	Completed
TAMU	Develop recommendations on how to create sediments in the laboratory	Completed
TAMU	Demonstration that typical sediments can be created in a repeatable manner in the laboratory and gas hydrates can be created in the pore space	Was completed in Phase II
UCB	Development of a conceptual pore-scale model based on available data and reports	Completed
UCB	Testing the developed concepts on simple configurations and verification of the result against known measurements and observations	Completed
LBNL	Completion of FLAC3D routines	Completed

LBNL	Completion of TOUGH-Fx/HYDRATE modifications and extensions	Completed
LBNL	Completion of the TOUGH-Fx/FLAC3D interaction interface	Completed
LBNL	Component integration and final testing of the coupled geomechanical numerical model TFxH/FLAC3D	Completed
SLB	Demonstration that Petrel can be used to develop an earth model for providing data to the TOUGH-Fx/FLAC3D	Completed

PHASE II (Budget Period II) – Modeling and Laboratory Measurements

a)

Task 5 – Revised research management plan

Task 6 – Fundamental studies of pore-scale geomechanical behavior Part II

Task 7 – Laboratory studies of basic rock properties in oceanic hydrate bearing sediments

Subtask 7.1 – Definition of methodology for creation of Synthetic Hydrate-Sediment mixture samples

Subtask 7.2 Analysis of the basic thermodynamic and kinetic behavior of the hydrates in oceanic environments

Subtask 7.3 Production of large-scale cores of artificial hydrate-bearing sediments using the techniques developed by LBNL

Subtask 7.4 Study the geomechanical properties in high-P, low-T triaxial cells, with simultaneous CT X-ray imaging

Subtask 7.5 Determine the geophysical signature of hydrates in porous media, and the effects of thermal and loading stresses

Task 8 – Developing Data Sets for Hydrate Deposits in Deep Water

Milestones for Phase II

TAMU	Demonstration that typical sediments can be created in a repeatable manner in the laboratory and gas hydrates can be created in the pore space	Completed
UCB	Fundamental studies of pore-scale geomechanical behavior	Completed
LBNL	Develop TOUGH + Hydrate + FLAC3D and begin laboratory mechanical properties testing	Completed
SLB	An interface between FLAC3D and Petrel was built to allow for efficient data entry into TOUGH + Hydrate + FLAC3D	Completed

DECISION TO FORGO PHASE III

Following a DOE-NETL held peer review of hydrate program projects in late 2007 and subsequent internal NETL evaluation of peer review feedback and other relevant project

related information, it was decided that his project would not be continued beyond the completion of project Phase II. As such, activities planned under project Phase III (integration of models and data generated during Phase I and II) were not carried out under this cooperative agreement.

The work done during Phases I and II of this contract were to develop a model that could be used to study seafloor stability in the present of natural gas hydrate deposits, to conduct laboratory testing to generate reliable data for use in the model, and put together the data sets for the model by reviewing the literature and understanding all of the measurements and data that have been published in the public domain from offshore gas hydrate expeditions

The goal of the originally planned Phase III was to use the models and data generated in Phases I and II to assess issues of seafloor stability in areas of known natural occurrence of gas hydrate, due to DOE decision not to continue the effort beyond Phase II many of the activities planned for Phase III were not conducted. However, some activities (performance of predictive studies of hydrate bearing sediments geomechanical behavior) related to planned Phase III work were continued, but under the other existing LBNL field work proposals (ESD05-048 and G308).

PHASE III (Budget Period III) – Integration of Models and Data
Note: Due to DOE decision not to continue this project beyond Phase II, these activities were not conducted under this cooperative agreement.

Task 9 – Revised research management plan
Task 10 – Predictive studies of hydrate bearing sediment stability performance under conditions representative of an offshore platform installation and operation

Subtask 10.1 Effect of structure weight on the geomechanical properties and stability performance of HBS in oceanic sub-floors in the immediate vicinity of platform anchors and/or foundations.

Subtask 10.2 Effect of heat exchange with non-insulated fluid production pipes on the geomechanical properties and stability performance of HBS.

Subtask 10.3 Effect of gas production from oceanic hydrate accumulations on the HBS geomechanical stability, with particular emphasis on sloping oceanic terrains.

Subtask 10.4 Long-term potential damage to wells and pipes located within HBS as a result of the geomechanical properties and displacement tendencies of HBS, and the effects of the issues discussed in subtasks 8.1 – 8.3.

Subtask 10.5 Integration of the localized studies in Tasks 8.1 to 8.4 in the evaluation of the large-scale stability of the hydrate-bearing oceanic sub-floor formations.

Subtask 10.6 Hydrate Stability Performance During Production and Its Impact on Borehole Stability and Well Casings

Chapter 2 – Numerical Studies on the Geomechanical Performance of Hydrate-Bearing Sediments

Introduction

This chapter describes the LBNL activities within the framework of the larger joint project entitled "Geomechanical Performance of Hydrate-Bearing Sediments in Offshore Environments" with participation by Texas A&M University (TAMU), the University of California at Berkeley (UCB) and Lawrence Berkeley National Laboratory (LBNL), and Schlumberger (SLB). The overall objective is to develop the necessary knowledge base and quantitative predictive capability for the description of geomechanical performance of hydrate-bearing sediments (hereafter referred to as HBS).

In this report we describe LBNL activities and the current status of geomechanical studies related to HBS under this cooperative agreement. The description of FY06 and FY07 work related to numerical studies on the geomechanical performance of the HBS is divided into the following tasks:

Task 06-1: Development of a Coupled Geomechanical Numerical Model
Task 06-2: Laboratory Studies of Geomechanical Behavior of HBS
Task 06-3: Predictive Studies of HBS Geomechanical Behavior and of the Corresponding Geophysical Signature
Task 07-1: Laboratory Studies of Geomechanical Behavior in Oceanic HBS
Task 07-2: Validation of Coupled Geomechanics/Flow Code by Using Data From a Geomechanical Lab Experiment
Task 07-3: Project Integration

Task 06-1: Development of a Coupled Geomechanical Numerical Model

This task was completed. The numerical simulator developed within this project has been described in detail in previous reports and is only briefly described here. The simulator was developed by coupling of the TOUGH+HYDRATE simulator (hereafter referred to as T+H) with a commercial geomechanical code (FLAC3D) (Figure 2-1). The capabilities of the T+H code are well known as being one of the most-advanced codes currently available for the simulation of system behavior in geological media containing gas hydrates. FLAC3D is a code widely used (several thousand licensed worldwide) for studies related to soil- and rock mechanics in both academia and engineering.

FLAC3D has built-in constitutive mechanical models suitable for soil and rocks, including various elastoplastic models for quasistatic yield and failure analysis, and viscoplastic models for time dependent (creep) analysis, that could be used directly or modified for analysis of geomechanical behavior of HBS. Moreover, the FLAC3D contains built in programming capabilities enabling with access to internal parameters enabling the coupling with an external simulator, such as T+H. As a result of the select approach, the numerical simulator for studies of geomechanical performance of the HBS could be devel-

oped and tested within a year and has already been applied to study geomechanical performance of both offshore (oceanic) and onshore (permafrost) HBS as will be described below.

In general, numerical studies of geomechanical performance of an HBS with T+H begins with analysis of the system behavior using T+H without considering geomechanical effects. Then the GEOMECHANICS option is invoked in the T+H input file and the coupled T+H and FLAC3D simulation runs seamlessly without user interference. We are in close contact with the ITASCA Company in Minnesota who develops the FLAC3D code and they have added several features to the FLAC3D code specifically for an increased efficiency of coupled T+H and FLAC3D simulations. They do this work for free, obviously realizing the future benefits of being part of one of the most advanced and useful simulator for the analysis of geomechanical performance of HBS.

The numerical simulator was first presented at the OTC 2007 symposium (Rutqvist and Moridis, 2007) in Houston, May 4-8 2007, and was also be presented at the 42nd US Rock Mechanics Symposium in San Francisco June 29-July 2, 2008 (Rutqvist and Moridis, 2008).

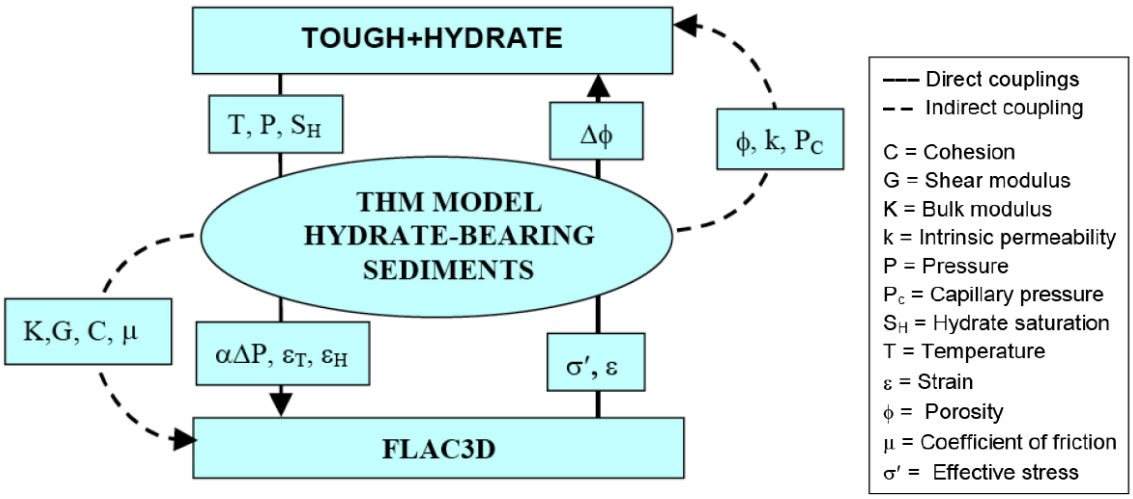

Figure 2-1 – Couplings of TOUGH+HYDRATE and FLAC3D for the analysis of geomechanical behavior of hydrate bearing sediments.

Task 06-2: Laboratory Studies of Geomechanical Behavior of HBS

The laboratory studies formed a continuous two-year effort. The results for FY06 and FY07 are described together, under Task 07-1 in a subsequent section.

Task 06-3: Predictive Studies of HBS Geomechanical Behavior and of the Corresponding Geophysical Signature

Studies of Offshore (Oceanic) HBS

The first comprehensive numerical study of geomechanical performance of oceanic HBS was presented in Rutqvist and Moridis (2007), at the 2007 Offshore Technology Conference (OTC 2007). In this study we investigated in three cases of coupled hydraulic, thermodynamic and geomechanical behavior of oceanic hydrate-bearing sediments. The first involved hydrate heating as warm fluids from deeper conventional reservoirs ascend to the ocean floor through uninsulated pipes intersecting the HBS. The second case described system response during gas production from a hydrate deposit, and the third involved mechanical loading caused by the weight of structures placed on the ocean floor overlying hydrate-bearing sediments.

Our simulation results indicated that the stability of HBS in the vicinity of warm pipes might be significantly affected, especially if the sediments are unconsolidated and more compressible. Figure 2-2 presents the three-dimensional model domain for this case, which includes detailed representation of a layers HBS and intersecting wellbore assembly. Figure 2-3 presents results of the evolution of volumetric strain, in which the red contours with volumetric strain exceeding 10% being associated with irreversible mechanical failure of the sediment. This failure was caused by heating and dissociation of the hydrates that in turn lead to a significant pressure increase essentially fracturing and shearing the formation around the heated well bore. Gas production from oceanic deposits may also affect the geomechanical stability of HBS under the conditions that are deemed desirable for production. Conversely, the increased pressure caused by the weight of structures on the ocean floor increases the stability of underlying hydrates.

The second numerical study on oceanic HBS was presented at OTC 2008 (Rutqvist et al. 2008a), focusing on geomechanical behavior of oceanic HBS, during depressurization-induced gas production, and in particular the potential well-bore instability and casing deformation. We investigated the geomechanical changes and wellbore stability for two alternative cases of production using horizontal well in a Class 3 deposit and vertical well in a Class 2 deposit (Figure 2-4).

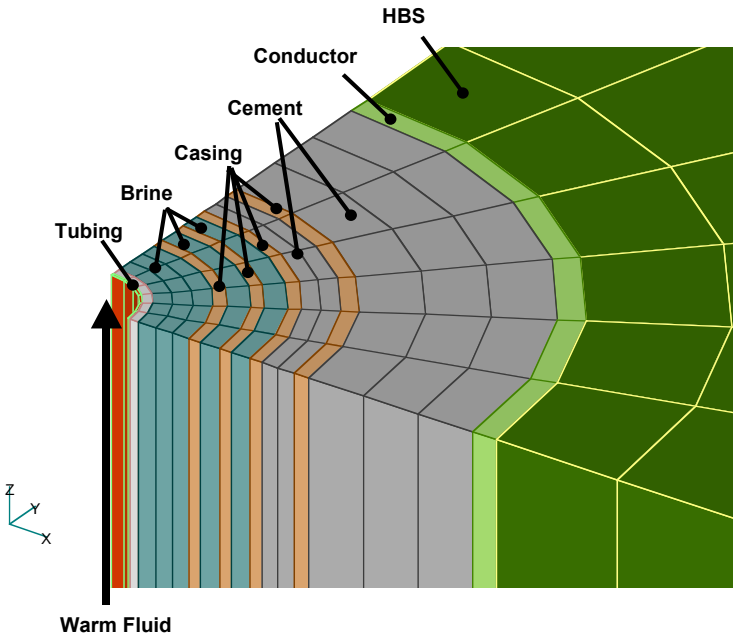

Figure 2-2 – Quarter-symmetric 3D model used in the analysis of geomechanical stability during hydrate heating as warm fluids from deeper conventional reservoirs ascend to the ocean floor through uninsulated pipes intersecting the HBS.

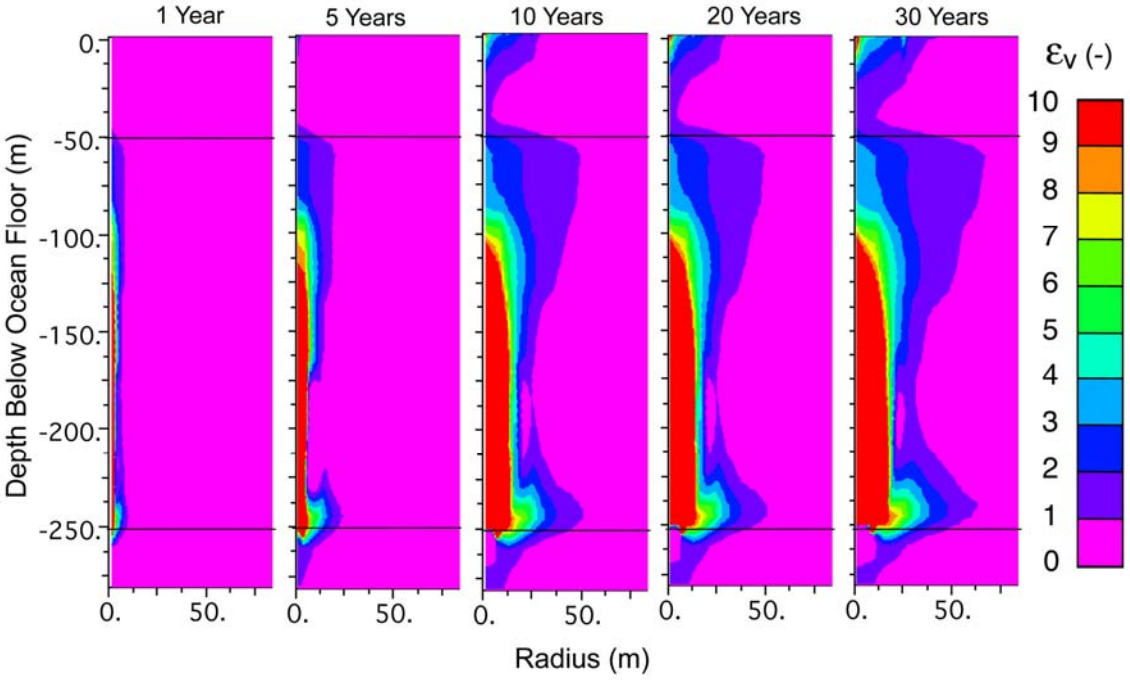

Figure 2-3 – Evolution of the spatial distribution of volumetric strain (indicating areas of significant plastic yield of the geological formations) in Problem 1 during 30 years of thermal loading.

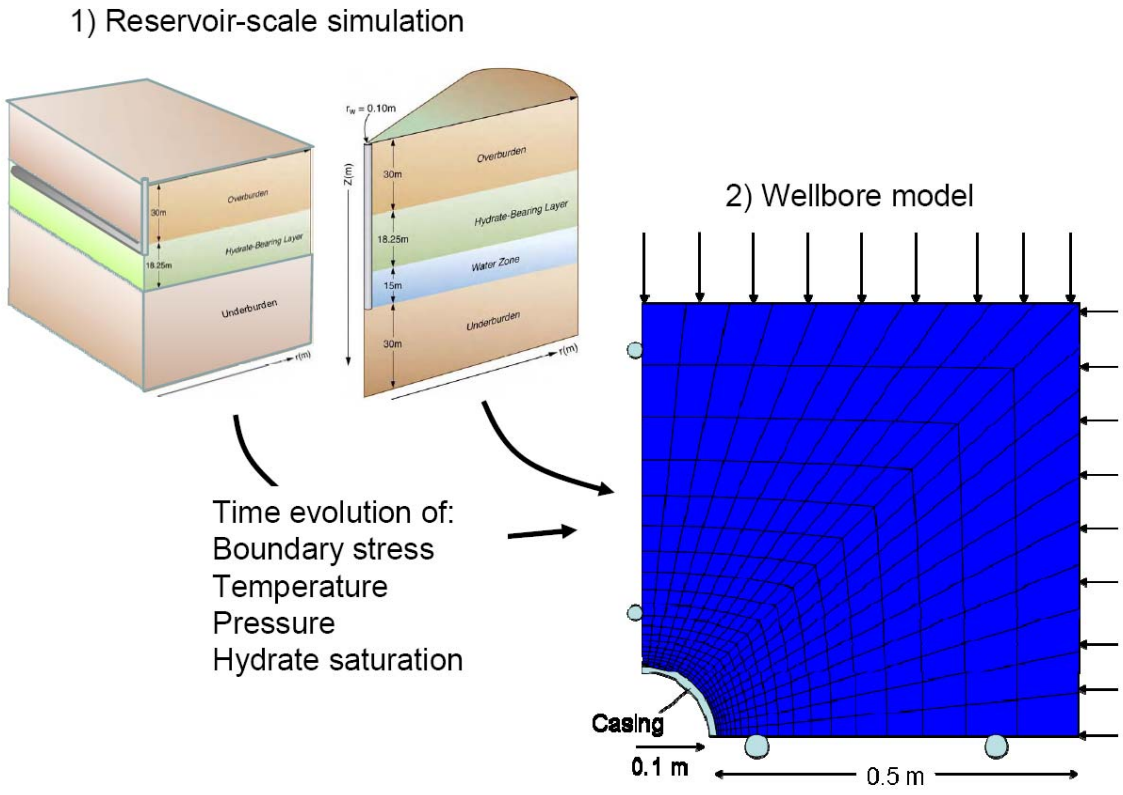

Figure 2-4 – Simulations of geomechanical performance of HBS and wellbore and casing stability for horizontal and vertical production wells during depressurization production from the Tigershark formation, Gulf of Mexico.

We compared the geomechanical responses and the potential adverse geomechanical effects for the two different cases. Our analysis showed that geomechanical responses during depressurization-induced gas production from oceanic hydrate deposits is driven by the reservoir-wide pressure decline, which is in turn is controlled by the induced pressure decline near the wellbore. Because any change quickly propagates within the entire reservoir, the reservoir wide geomechanical response can occur within a few days of production induced pressure decline. Our study showed that there is a major difference in the geomechanical performance around horizontal and vertical wells. In the case of production from horizontal wells, the anisotropic stress induced by the general reservoir depressurization can cause shear failure near the wellbore adjacent to the perforation. For production from a vertical well on the other hand, the formation will be unloaded uniformly in a plane normal to the axis of the wellbore. Therefore, the load on the wellbore casing will decrease and failure of the formation around the perforation is prevented. This result is shown in Figure 2-5, where it is apparent that formation failure does not occur near the well bore although failure occurs away from the wellbore, especially in the water zone below the HBS.

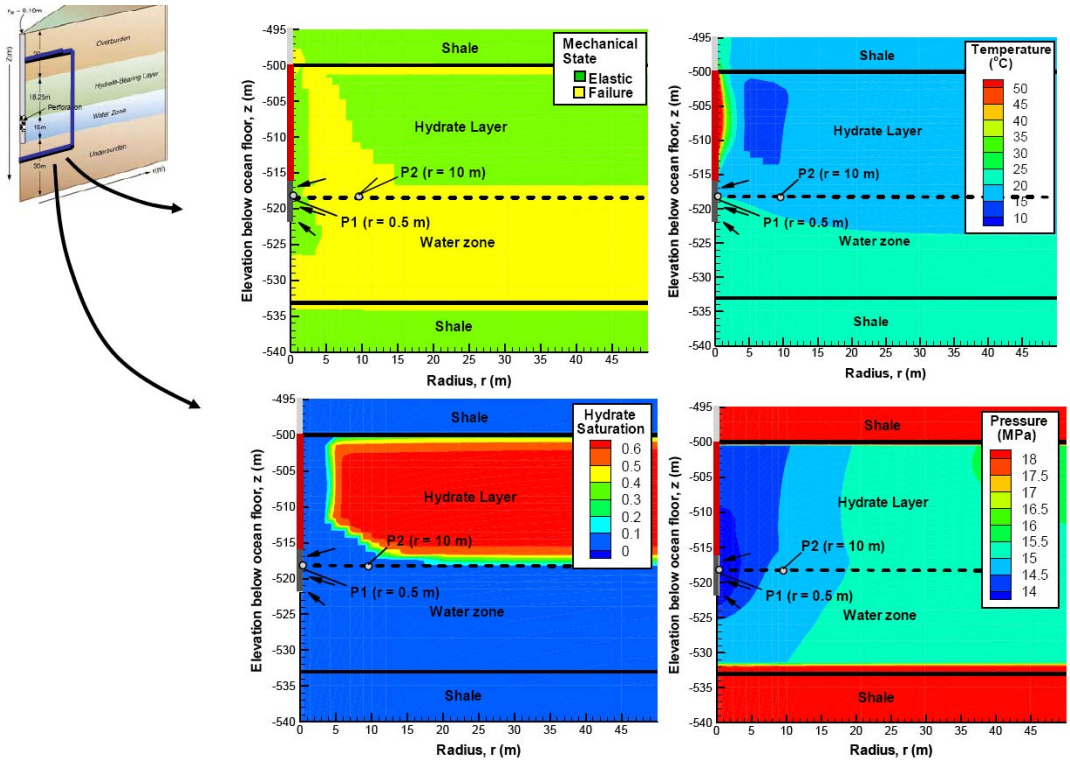

Figure 2-5 – Simulation results of geomechanical performance for production from a vertical well after 6 months of constant rate production.

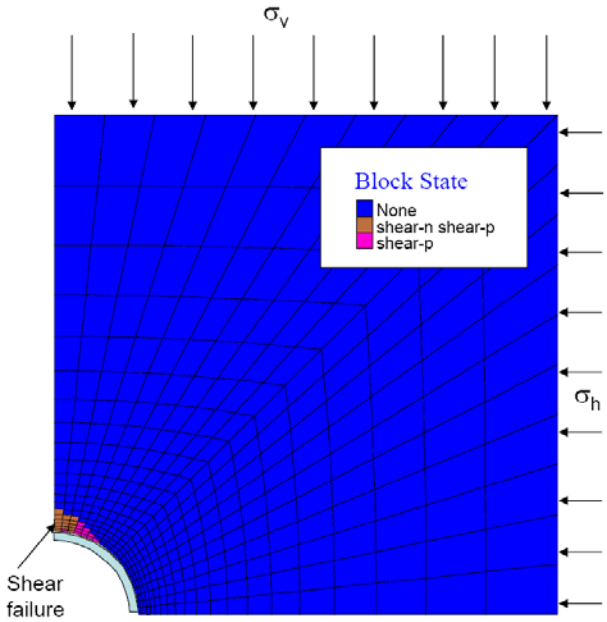

Figure 2-6 – Simulation results of shear failure occurring near the casing around a horizontal production well.

In the case of a horizontal well, the main concern is increased compression (load) against the upper part of the well bore casing caused by the compacting reservoir. This compressive load first caused local shear failure (yielding) in the formation (Figure 2-6). Such shear failure may lead to loss of bonding between grains, which in turn could result in production of solid sediment particles and formation of cavities around the perforation. Our analysis shows that for reasonable strength properties of an oceanic HBS, there is a very high potential for such localized shear failure. In the case of a vertical well, the main concern is the vertical settlement of the formation, which may be substantial, especially in the vicinity of the well where pressure is the lowest.

Studies of Onshore (Sub-Permafrost) HBS

The first-ever assessment of the impact of production on the well stability and the likelihood of formation failure in a sub-permafrost HBS was presented at the upcoming International Conference on Gas Hydrates (ICGH 2008), Vancouver, British Columbia, CANADA, July 6-10, 2008 (Rutqvist et al. 2008b). In this simulation study, we analyzed the geomechanical response of two known Class 3 permafrost deposits: the Mallik (Northwest Territories, Canada) deposit and Mount Elbert (Alaska, USA) deposit. Gas was production from these deposits was simulated at constant pressure using horizontal wells placed at the top of the hydrate layer (HL). Figure 2-7a presents the model geometry whereas Figure 2-7b shows a profile of sonic velocities that were used to define the mechanical properties of the HBS and overlying permafrost zone.

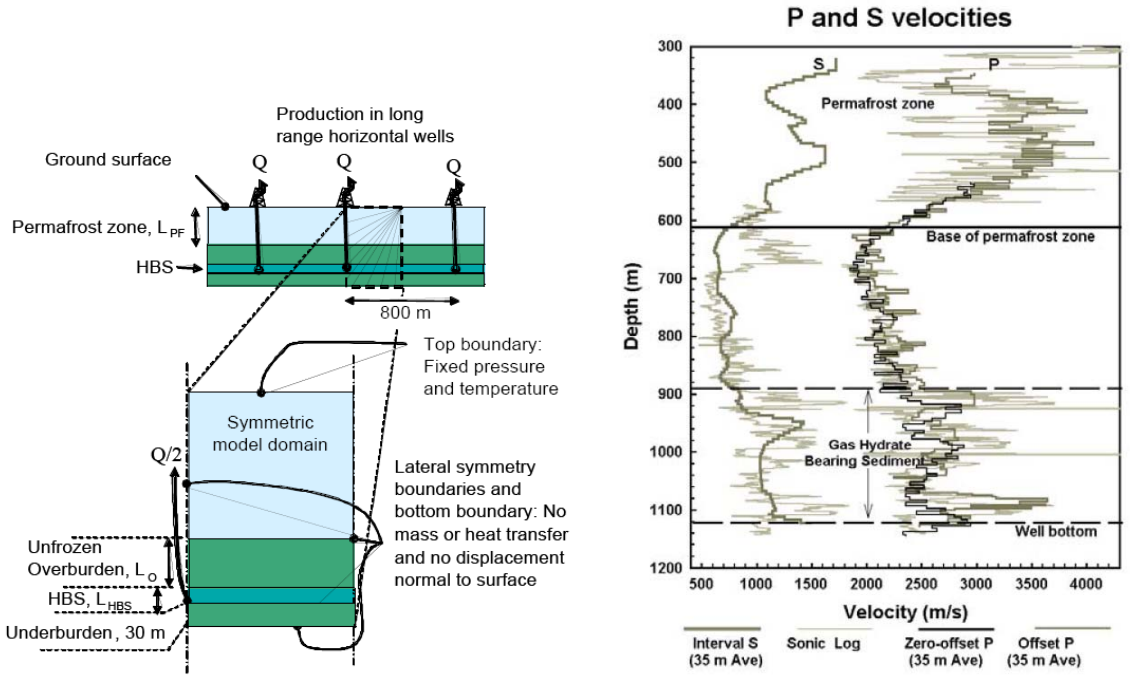

(a) (b)

Figure 2-7 – (a) Simulation domain geometry and (b) sonic velocity profiles across the Mallik deposit.

Figure 2-8 presents the calculated distribution of temperature, pressure, hydrate saturation, and volumetric strain after 3 years of production. The numerical analysis showed that the depressurization-induced dissociation begins at the well bore, and then spreads laterally mainly along the top of the HL. The depressurization results in an increased shear stress within the body of the receding hydrate, and causes a vertical compaction of the reservoir. However, its effects are partially mitigated by the relatively stiff permafrost overburden, and compaction is limited to less than 0.5%.

The increased shear stress may lead to shear failure in the hydrate-free zone that is bounded by the HL overburden and the downward-receding upper dissociation interface. This zone undergoes complete hydrate dissociation, and the cohesive strength of the sediment is low. We determined that the likelihood of shear failure depends on the initial stress state, as well as on the geomechanical properties of the reservoir. The Poisson's ratio of the hydrate-bearing formation is a particularly important parameter that determines whether the evolution of the reservoir stresses will increase or decrease the likelihood of shear failure.

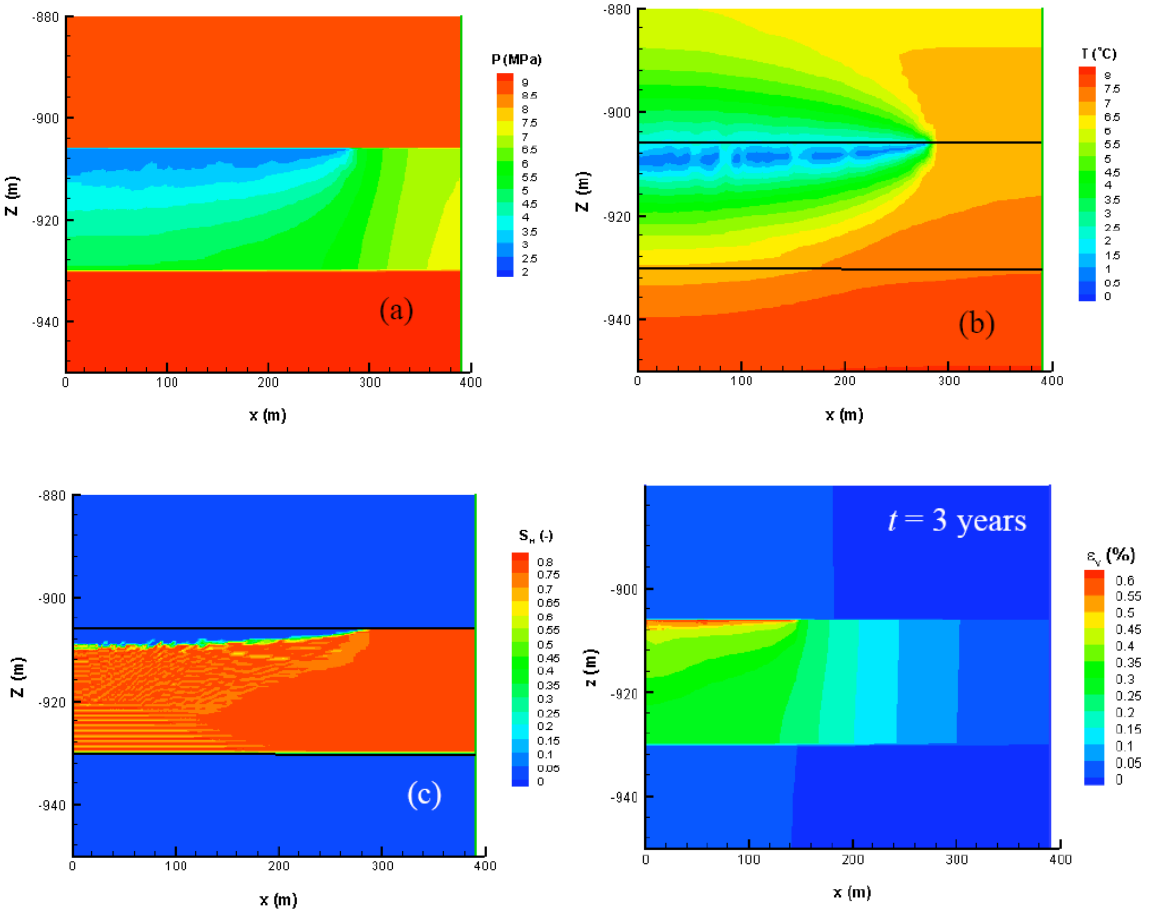

Figure 2-8 – Pressure, temperature, hydrate saturation and volumetric strain after 3 years of simulated constant pressure production at Mallik.

Task 07-1: Laboratory Studies of Geomechanical Behavior in Oceanic HBS

This task was completed. Understanding the geomechanical and geophysical properties of oceanic HBS is critical for successful engineering of subsea equipment platforms and for well placement and design. Changes in hydrate abundance will change the strength of the medium, necessitating changes in design, and will impact geophysical signals, relevant to monitoring. A suite of measurements of geophysical and geomechanical properties of tetrahydrofuran (THF) hydrate-bearing sediments have been made by others, with THF hydrate being an analog for methane hydrate. Verification and validation of this analogy using methane hydrate is needed to allow for unconstrained use of the existing data.

To address these issues, LBNL designed and built a unique pressure vessel capable of forming methane hydrate in the pore space of sediments, applying a confining stress and independently applying an axial load, while allowing simultaneous measurements of the compressive and shear wave velocities, sample length, and spatially resolved sample density using x-ray CT scanning to observe sample structure. A schematic of the vessel is presented in Figure 2-9.

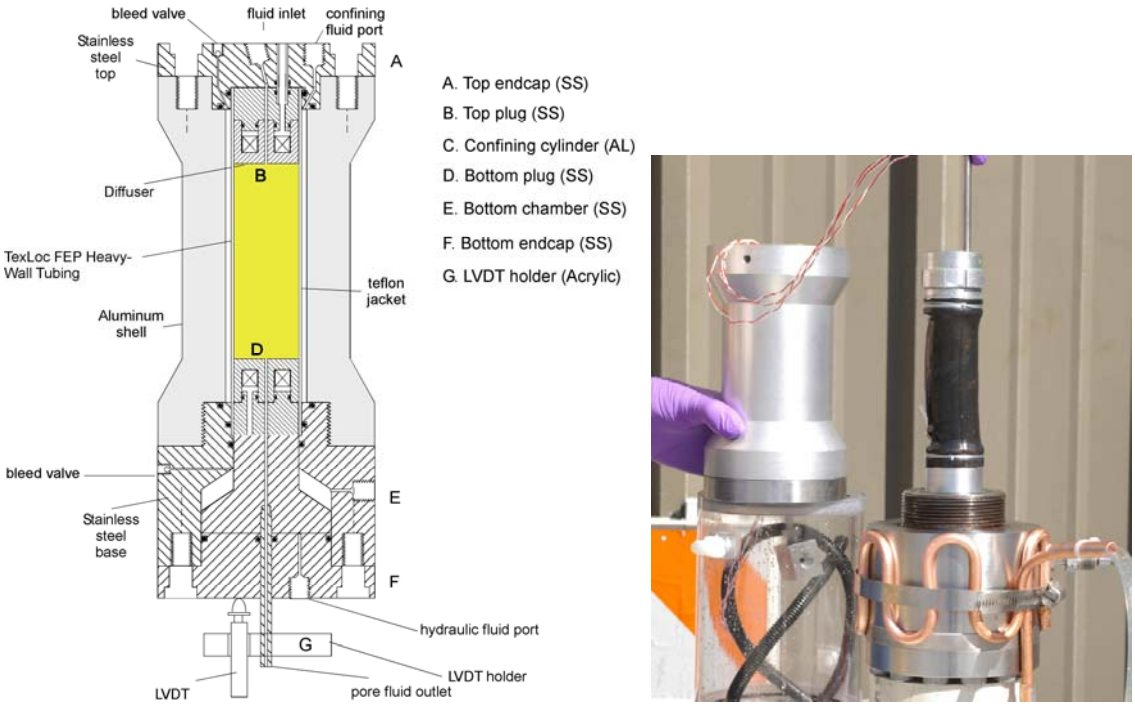

Figure 2-9. Cell schematic and photo showing assembly

Test of Acoustic System

Elements used in the geomechanical cell were assembled and independently tested prior to assembly in the cell. One critical component is the seismic (acoustic) source and receiver installed within the loading pistons (Figure 2-10). Seismic measurements will provide data regarding the mechanical property changes in test cores during hydrate formation and a loading test, which will augment and compliment x-ray CT imaging.

One common problem when conducting S-wave measurements in a long core sample is the degradation of wave quality due to P-waves (which travel faster than S-waves) and conversions into surface or flexural waves (which causes waveform dispersion). To mitigate this problem, S-waves in our test cell uses are generated via the torsion mode rather than commonly used polarized shear mode. The quality of the seismic signal was tested across an acrylic cylinder, using lead foil between the acrylic and the platens to aid in contact (Figure 2-11).

Using the seismic transducers, two types of source excitation methods were used. The first method drove the source element with a square-shaped high-voltage pulse. By choosing an optimal pulse width, the piezoelectric element is brought to resonance, generating large-amplitude seismic waves. This method has an advantage of generating large amplitudes. However, the waves are limited to relatively high frequencies (~200 kHz). Examples of P- and S-wave signals using the resonant-mode excitation are shown in Figure 2-12.

An alternative method is to drive the source quasi-statically using electric signals with arbitrary shapes. This has an advantage of generating waves with a broad band of frequencies, though the resulting signal amplitudes are generally small. For testing attenuating (high-loss) materials, the amplitude loss of high-frequency waves during propagation may be more disadvantageous than the initial small amplitude of low-frequency waves. Using this technique, we have identified the optimal excitation frequencies to be used for the measurements, based upon the quality of measured seismic pulses. For P-waves, this was 200 kHz, and for S-waves, 50 kHz. The relatively long wavelength resulting from the S-wave's lower frequency should help to reduce expected degradation of signal quality due to scattering by heterogeneities within a hydrate-bearing sediment core.

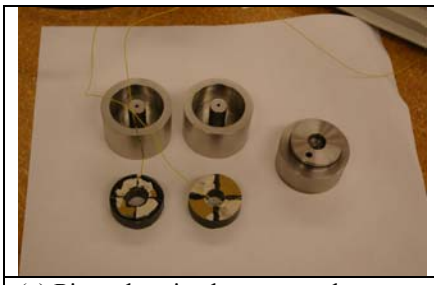

(a) Piezoelectric elements and transducer housing

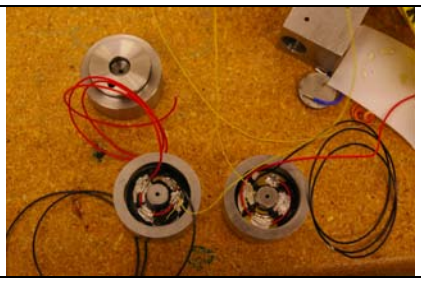

(b) Installed in the housing. Electrodes attached.

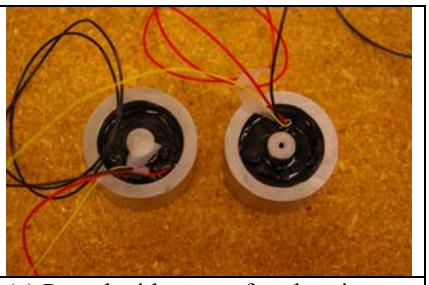

(c) Potted with epoxy for electric insulation and mechanical stability

Figure 2-10. Construction of piezoceramics-based seismic (acoustic) transducers

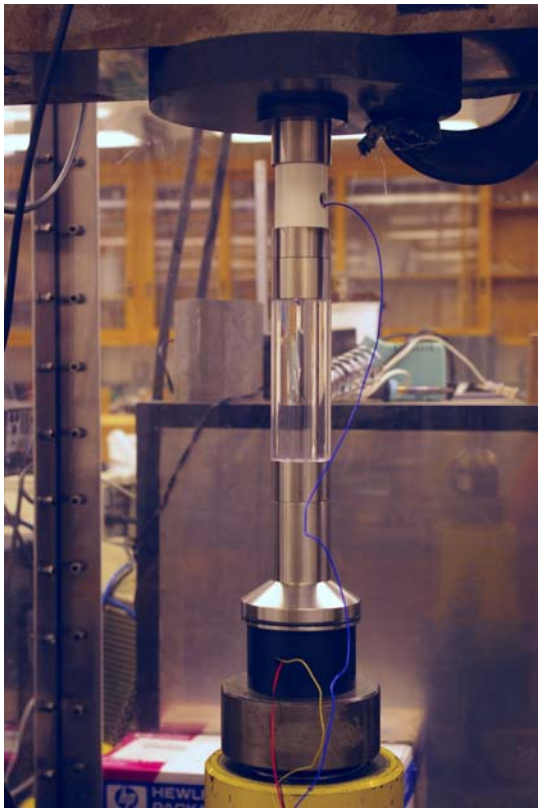

Figure 2-11. Testing seismic signal quality using an acrylic core. The stainless steel cylinders at the top and the bottom of the sample house piezoelectric elements and serve as transducers. These are the actual components of the new hydrate-testing cell under construction.

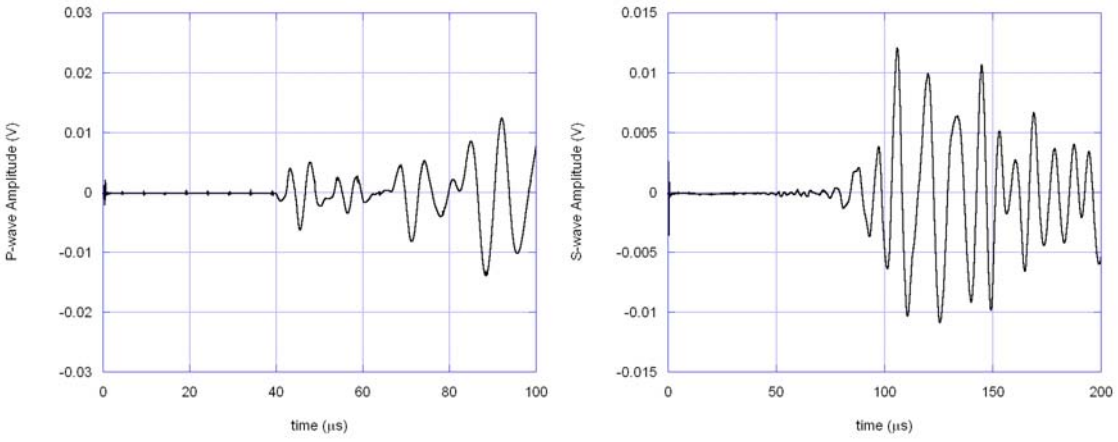

(a) P-wave signals (1st arrival~40 □s) (b) S-wave signals (1st arrival~77 □s)

Figure 2-12. Seismic signals measured using resonant-mode excitation of the source.

Three samples were tested in the vessel to develop the procedure. These samples were composed of THF hydrate in US Silica F110 silica sand. The THF hydrate was used in

place of methane hydrate while safety computations on the pressure vessel were being performed. The three samples had different hydrate saturations and formation procedures to address different issues. The first sample was fully saturated with a mixture of water and THF in a ratio such that nearly all of the pore space would be filled with hydrate. The second sample was fully saturated with a different mix of THF and water and hydrate was formed at a lower temperature such that 50% of the pore space was filled with hydrate, and the remaining pore space was filled with THF and some water. The third sample was formed by moistening sand with a THF-water mixture to attempt to form hydrate in 50% of the pore space leaving the remaining pore space filled with gas. We hypothesized that because of formation technique, Samples 2 should result in pore-filling hydrate, and Sample 3 should result in grain-cementing hydrate. Each of the samples were prepared away from the CT scanner, and then mounted to the CT table (Figure 2-13).

Sample 1 was tested by applying an increasing stress on the sample and measuring strain. Samples 2 and 3 were tested by applying increasing strain on the sample and monitoring the stress required to attain that strain. Two locations are highlighted on each curve in Figure 2-14. The square on each curve indicates the separation of the "quasi-elastic" region (stress-strain region beneath the grain-scale failure point) from the large-strain region. The second location on each curve, shown by the circles, identifies the maximum stress the sample withstood.

	Sample#1	Sample#2	Sample#3
Porosity	36%	34%	38%
Sample Volume (from CT)	120.01 cc	122.15 cc	134.98 cc
THF hydrate Saturation	100%	50%	40%
THF (liquid) Saturation	0%	50%	~0%
Cooling temp. (hydrate formation temp.)	+1°C (4.4°C)	-12°C (-10°C)	+1°C (4.4°C)

Cementation model

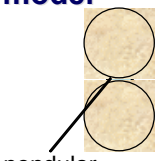

pendular THF+water

Pore-filling model

Table 2-1. Experiment conditions

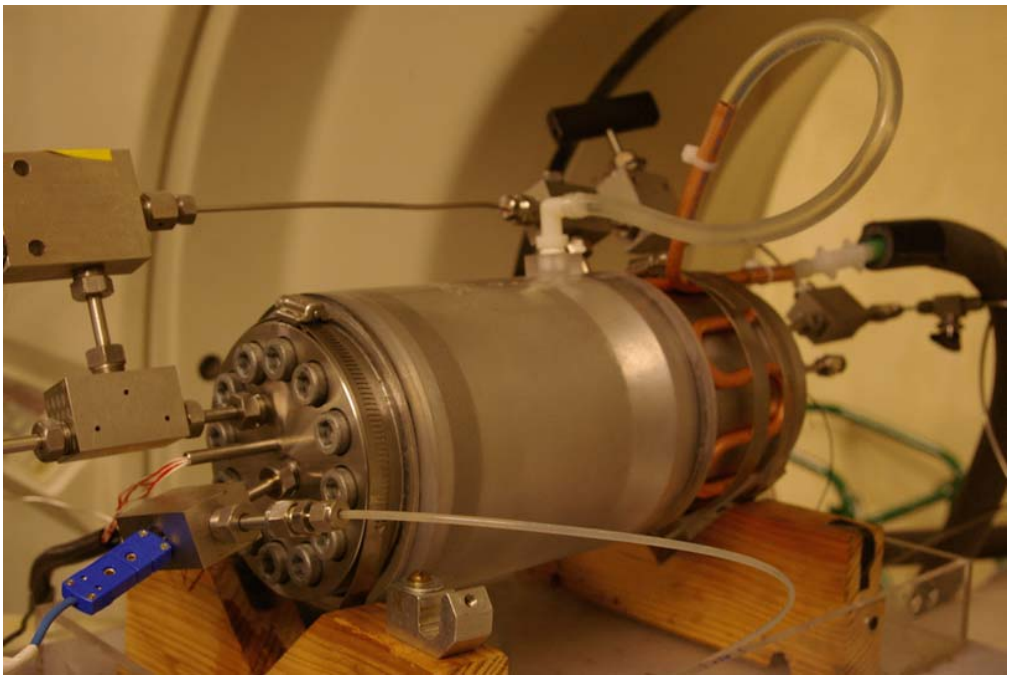

Figure 2-13. Pressure vessel containing sample mounted on x-ray CT scanner.

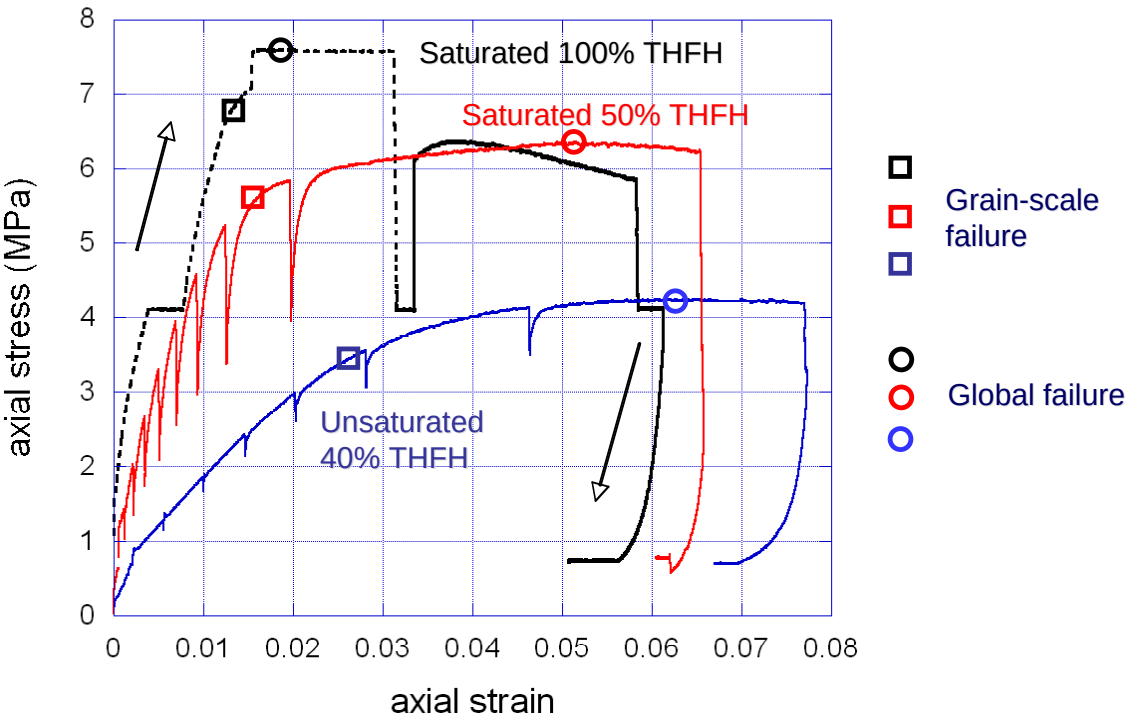

Figure 2-14. Results of initial tests.

Figure 2-15 shows the spatial density along an axial plane selected to most clearly show the sample changes that occurred on loading. For samples 1 and 2, hydrate formation induced very small changed in the sample density, however packing Sample 3 resulted in a heterogeneous distribution. Loading Samples 1 and 2 resulted in regions of shear localization and dilation, having lower density where failure occurred. Sample 3 however, behaved entirely differently. This sample was packed in lifts, resulting in initial density heterogeneity. Where the porosity was lower, the liquid saturation would be higher due to capillary imbibition. When hydrate formed, this heterogeneity was enhanced. Upon loading, the sample showed much greater dilation with perhaps some shear localization.

An example of compression and shear wave behavior is shown in Figure 2-16 for Sample 1, with sequential curves shifted downwards. With the sand/fluid system (top curves), waves become more distinct and speeds increase with increasing axial load. When hydrate formed, there was a very large increase in both amplitude and velocity. With increased axial stress, velocities increase until failure, and then begin to decrease on additional loading.

Our attempt to observe the difference between the cementing and pore-filling hydrate indicated that heterogeneity on a scale larger that the grain scale strongly influenced the behavior of the material. Hydrate-bearing sediment with this mesoscale heterogeneity exhibited much smaller strength and seismic velocities than an HBS sample with uniform distribution of hydrate (which can be pore filling and possibly grain cementing), for similar hydrate saturations.

Vessel Redesign

Engineering calculations on the pressure vessel identified possible elevated stress concentrations in the vessel, resulting in a re-design and remanufacture of the vessel prior to testing any methane hydrate bearing samples. Figure 2-17 shows an engineering schematic of the redesigned vessel. Locations of stress concentrations have been minimized, while retaining the valuable features of the previous vessel. Measurements using the new vessel will begin upon completion and shake down.

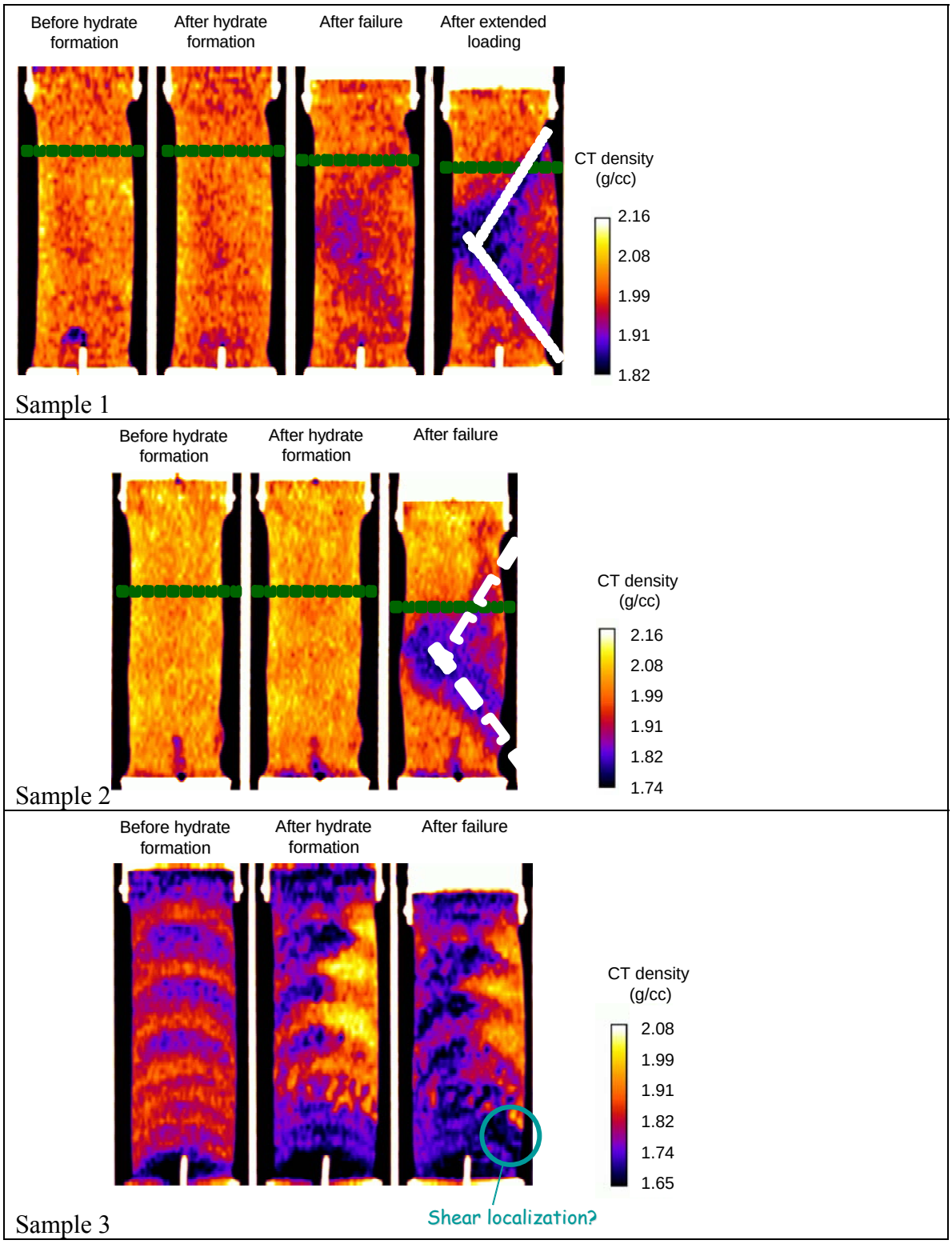

Figure 2-15. Cross sections of CT images for Samples 1, 2, and 3 showing the initial condition, density following hydrate formation, failure, and shear localization (following extended loading in Sample 1 only).

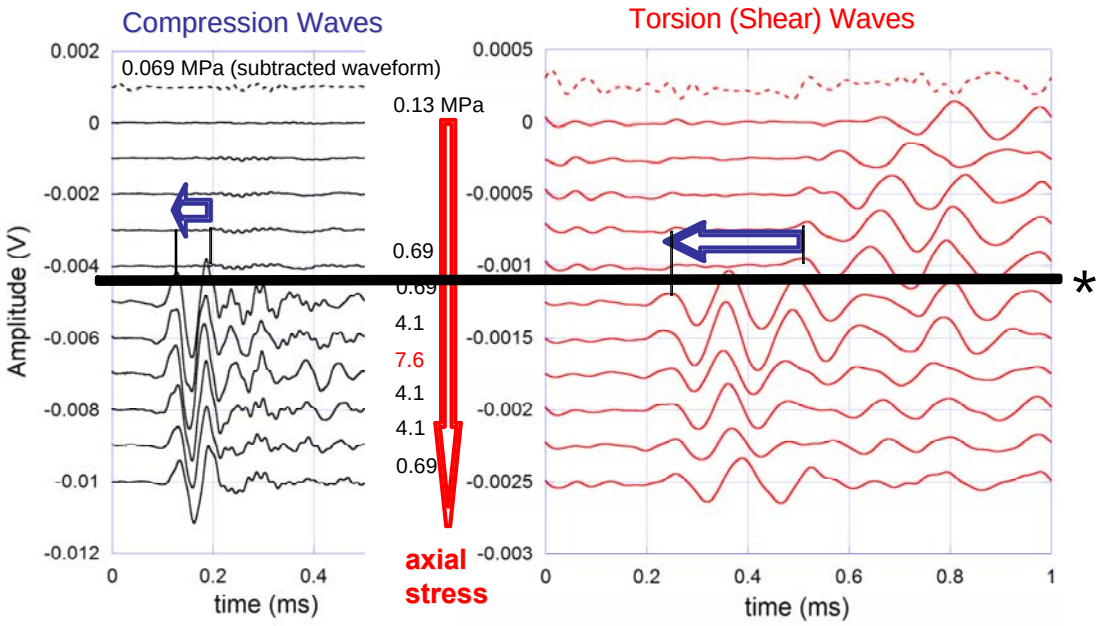

Figure 2-16. Compression and shear wave behavior in Sample 1. Hydrate formation is indicated by *.

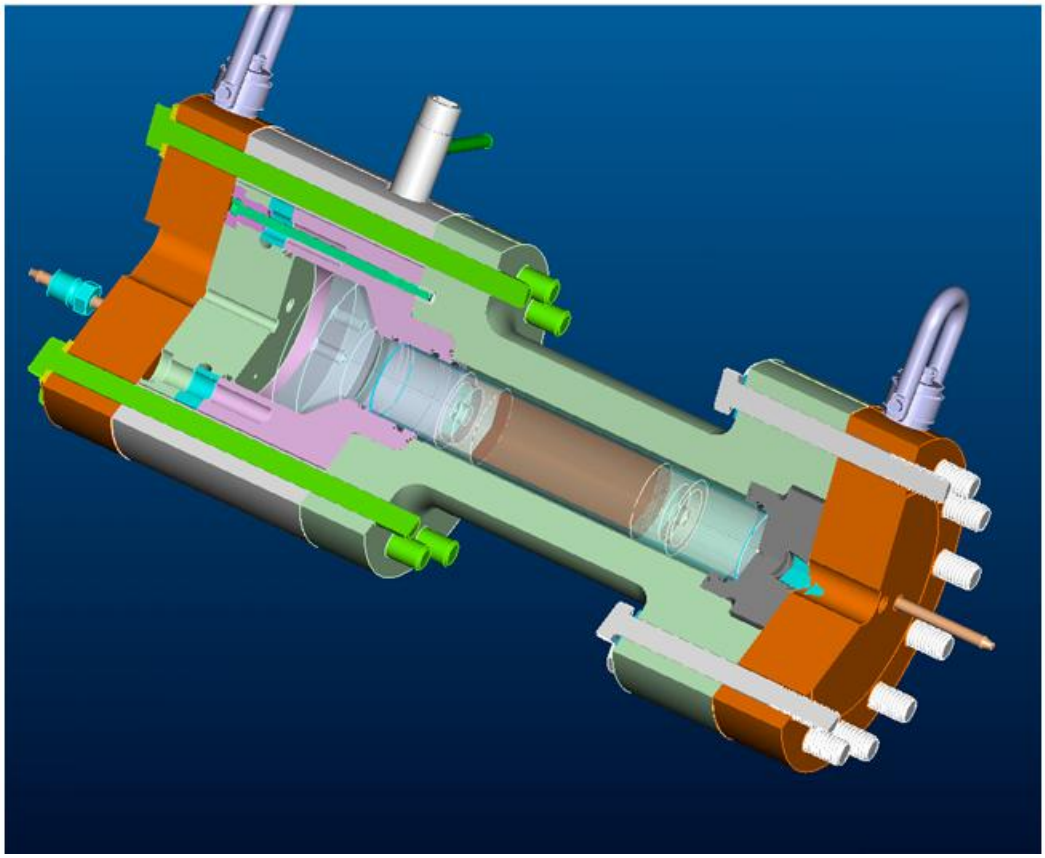

Figure 2-17. Schematic of redesigned vessel.

Task 07-2: Validation of Coupled Geomechanics/Flow Code by Using Data From a Geomechanical Lab Experiment

This task was completed in FY2008 instead of FY2007 at no additional cost to the project. In FY2007, the original vessel could not be used because of safety concerns (possible stress concentrations), and had to be remanufactured. Upon completion of the remanufacturing process, laboratory data were used to validate the coupled geomechanics/flow model. The data and results related in the validation effort are included in a scientific paper under preparation for presentation in an upcoming scientific conference.

Task 07-3: Project Integration

This task was completed. The integration effort represented interaction between LBNL and TAMU through the training and supervision of students working on the subject, and includes the identification and description (in terms of geological models) of problems to be investigated. Deliverables included:

(1) A TAMU student trained in the use of T+H/FLAC.
(2) A minimum of two problems identified for further analysis, with development of the corresponding geological models and of the necessary input files (activity completed by TAMU student with LBNL supervision).
(3) Contribution of information to Texas A&M University as required to meet reporting requirements of the associated cooperative agreement (DE-FC26-05NT42664) with respect to activities conducted under this field work proposal.
(4) Four conference papers and four conference presentations on the subject, with one paper additionally submitted to a refereed journal for publication.

Concluding Remarks

Presently we have developed a novel simulator for analysis of geomechanical performance of HBS and we already applied the simulator on studies related to the geomechanical behavior of both offshore (oceanic) and onshore (sub-permafrost) hydrate deposits. In these studies we have addressed the questions about the geomechanical performance of the HBS and the potential for well bore instability and casing deformation. The next step will be to expand our analysis to two-way coupled effects, i.e. investigating the effect of compaction-induced changes in porosity and permeability on the production performance. Moreover, additional geomechanical studies related to geomechanical performance of soft oceanic sediments and seafloor stability will be considered.

The results of these studies have been presented at several conferences, and all the corresponding scientific papers are under review for publication in peer-reviewed journals:

Nakagawa, S., T.J. Kneafsey, and G.J. Moridis (2008). Mechanical Strength and Seismic Property Measurements of Hydrate-Bearing Sediments (HBS) During Hydrate Formation and Loading Tests. OTC 19559. Paper presentation at the 2008 Off-

shore Technology Conference held in Houston, Texas, U.S.A., 4–8 May 2008. doi 10.4043/19559-MS.

Rutqvist J. and Moridis G. (2007). Numerical Studies on the Geomechanical Stability of Hydrate-Bearing Sediments. OTC-18860. Paper presentation at the 2007 Offshore Technology Conference held in Houston, Texas, U.S.A., 30 April–3 May 2007.

Rutqvist J., Moridis G., Grover T., and Holditch S. (2008a). Coupled Hydrological, Thermal and Geomechanical Analysis of Wellbore Stability in Hydrate-Bearing Sediments. OTC-19572. Paper presentation at the 2008 Offshore Technology Conference held in Houston, Texas, U.S.A., 4–8 May 2008.

Rutqvist J. and Moridis G. (2008). Development of a Numerical Simulator for Analyzing the Geomechanical Performance of Hydrate-Bearing Sediments. Proceedings of the 42th U.S. Rock Mechanics Symposium, San Francisco, California, USA, June 29-July 2, 2008: American Rock Mechanics Association ARMA, Paper No. 139.

Rutqvist J., Moridis G., Grover T., and Collett T. (2008b). Geomechanical response of known permafrost hydrate deposits to depressurization-induced production. Proceedings of the 6th International Conference on Gas Hydrates (ICGH 2008), Vancouver, British Columbia, CANADA, July 6-10, 2008.

Chapter 3 – Natural Gas Hydrates – Issues for Gas Production and Geomechanical Stability

This chapter describes the activities at Texas A&M University within the framework of the larger joint project entitled "Geomechanical Performance of Hydrate-Bearing Sediments in Offshore Environments" with participation by Texas A&M University (TAMU), the University of California at Berkeley (UCB) and Lawrence Berkeley National Laboratory (LBNL), and Schlumberger (SLB). The overall objective is to develop the necessary knowledge base and quantitative predictive capability for the description of geomechanical performance of hydrate-bearing sediments (hereafter referred to as HBS).

In this report we describe recent activities on geomechanical studies related to HBS and our analysis of the gas production from the Messoyahka Gas Hydrate Reservoir in Russia.

Some of the results of this work have already been presented or are about to be presented at several conferences and in a Doctor of Philosophy Dissertation by Tarun Grover. These documents are listed below:

Rutqvist J., Moridis G., Grover T., and Holditch S. (2008a). Coupled Hydrological, Thermal and Geomechanical Analysis of Wellbore Stability in Hydrate-Bearing Sediments. OTC-19572. Paper presentation at the 2008 Offshore Technology Conference held in Houston, Texas, U.S.A., 4–8 May 2008.

Grover T., Moridis G., and Holditch, S.A. (2008a). Analyis of Reservoir Performance of the Messoyakha Gas Hydrate Field. Proceedings of the 18th International Offshore and Polar Engineering Conference (ISOPE 2008), Vancouver, British Colombia, CANADA, July 6-11, 2008.

Rutqvist J., Moridis G., Grover T., and Collet T. (2008b). Geomechanical response of known permafrost hydrate deposits to depressurization-induced production. Proceedings of the 6th International Conference on Gas Hydrates (ICGH 2008), Vancouver, British Columbia, CANADA, July 6-10, 2008.

Grover T., Moridis G., and Holditch S.A. (2008b). Analysis of Reservoir Performance of the Messoyahka Gas Hydrate Reservoir. Proceedings of the 2008 Annual Technical Conference and Exhibition of the Society of Petroleum Engineers (SPE), Denver, Colorado to be held 21-24 September 2008.

Grover T. (2008c). Natural Gas Hydrates – Issues for Gas Production and Geomechanical Stability. A Dissertation for a Doctor of Philosophy Degree at Texas A&M University, August 2008.

Introduction to Study of Gas Production at Messoyahka

Natural gas hydrates have been the subject of active research in the oil and gas industry since their role in blocking fluid flow in oil and gas pipelines was demonstrated by Hammerschmidt (1934). Later, Makogon (1965) proposed that naturally occurring gas hydrates could exist in the earth's subsurface. Since 1965, a number of research projects have been performed to estimate and quantify the volume of naturally occurring gas hydrates. Although there is uncertainty over the quantity and distribution of naturally occurring hydrates in the earth, there is general agreement that substantial volumes of gas hydrates do exist in nature (Sloan and Koh, 2008). According to the latest data gathered by various expeditions for hydrates, the gas resource in hydrate ranges from 10^5 to 10^6 Tcf (US Department of Energy, 2007).

Natural gas hydrates (NGH) are crystalline compounds formed by the association of molecules of water with natural gas. NGHs are a subset of substances known as clathrates, which means "cage like structures". The formation of natural gas hydrates depends upon pressure, temperature, gas composition, and the presence of inhibitors such as salts. NGHs are found in the subsurface in two distinct types of settings. One is within and below the permafrost in arctic regions and the second is in deepwater marine environments.

The volume of gas present in the form of hydrates around the world has been estimated to range from 10^5 to 10^6 Tcf (US Department of Energy, 2007). The characterization of hydrate deposits involves collection and interpretation of geological, geophysical, geochemical, sedimentological, reservoir, and thermal data. Hydrates can be dissociated by the following three fundamental mechanisms (Makogon, 1966):

1. reducing the reservoir pressure;
2. increasing the reservoir temperature; and
3. using chemicals to change the equilibrium conditions.

The first instance of finding gas hydrates was in the Messoyakha field on the eastern border of Siberia. This discovery was published by Makogon and his co-workers (1970; 1971b). The Messoyakha gas field has been described as a gas reservoir overlain by gas hydrates and underlain by an aquifer of unknown strength. Many observed phenomena at the Messoyakha Field during its production operations appear to indicate the presence of gas hydrates (Makogon, 1981). Important observations reported by Makogon (1981) included:

1. An increase in the average reservoir pressure when the field was shut-in for several years;
2. No change in the elevation of the gas-water contact during the last 30 years of production;
3. The wells completed within the hydrate layer flowed at very low rates compared to the wells completed in the free gas zone; and
4. Methanol injection into low-producing wells resulted in significantly increased production at higher wellhead pressures

The main objective of this study was to use a special reservoir simulation model called Tough + Hydrate to simulate the Messoyakha reservoir behavior during the initial production and shut-in period. This project was designed to reconcile the available data on the Messoyakha Field with conceptual and fundamental knowledge of hydrates. The reconciliation study essentially was important to delineate the uncertainties in the available data. These uncertainties prompted us to develop a series of 2D cylindrical models that can be used to study the characteristics of the Messoyakha Field. Additional detail can be found in the dissertation by Grover (2008).

The Messoyakha Field - Thermodynamic State

Figure 3-1 shows the thermodynamic state at the top and bottom of the Messoyakha gas reservoir with respect to the equilibrium Pressure – Temperature curve that describes the coexistence of the gas, aqueous and hydrate phases. Figure 3-1 indicates a typical Class 1 deposit (Moridis and Collett, 2002), with the upper part of the hydrate layer deeply in the hydrate stability zone, equilibrium conditions at the bottom of the hydrate layer (which coincides with the bottom of the stability zone), and a zone with free mobile gas (outside the hydrate stability zone) below the gas hydrate layer.

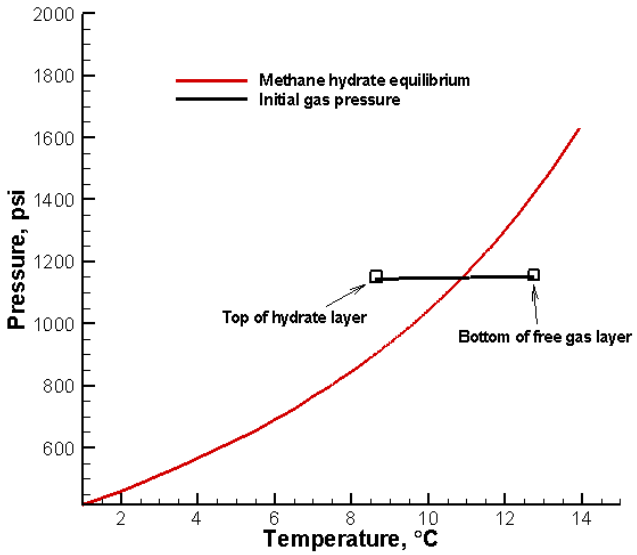

Figure 3-1 – Initial thermodynamic state of the Messoyakha reservoir

The Geology

A cross-sectional schematic of the Messoyakha field is shown in Figure 3-2 (Makogon et al., 2005). The Messoyakha gas field is enclosed in an anticlinal structural trap and is overlain by a 420 to 480 m thick permafrost zone. The producing intervals are located in the Dolgan formation (sandstone) which is sealed by an overlying shale layer. The Dolgan formation is frequently interbedded with shale streaks (Makogon, 1981; Krason and Ciesnik, 1985; Krason and Finley, 1992; Makogon, 1997) which can result in a low value of vertical permeability.

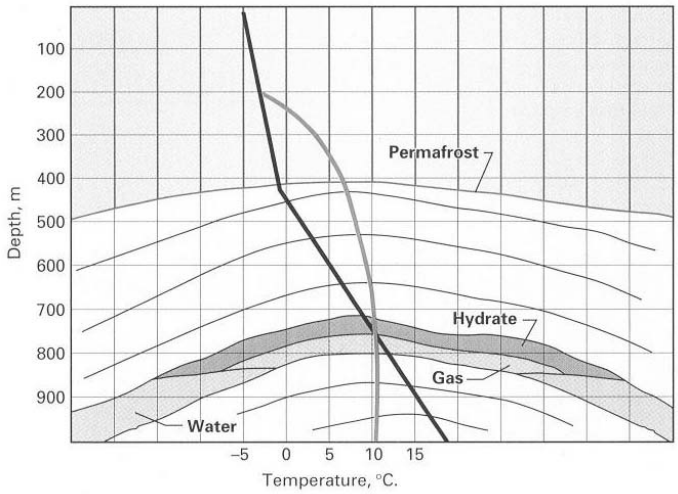

Figure 3-2 – Cross section of the Messoyakha reservoir (from Makogon et al., 2005)

The structural enclosure of the field is 84 meters and the areal extent of the field is 12.5 km x 19 km (Makogon et al., 2005). A contour map of the top of the Cenomanian Dolgan Formation at the Messoyakha field is shown in Figure 3-3 (Krason and Finley, 1992). The depths (in meters) refer to the elevation below mean sea level.

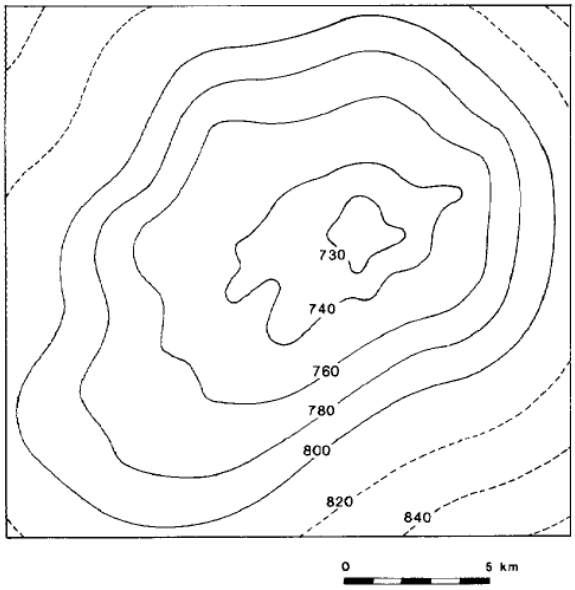

Figure 3-3 – Contour map of the Messoyakha field (from Sapir et al., 1973)

Operations

More than 60 wells have been drilled in this field on a pattern that was essentially a 500 m x 1000 m well spacing. Production began in 1970 and continued until 1977. Initial production rates per well was reported to range from 111 Mscf/day to 6,275 Mscf/day.

The production in the Messoyakha field was reduced to zero from 1979-82. While the field was shut-in, the reservoir pressure increased. This pressure increase was interpreted to have been caused by the continued dissociation of hydrates (Makogon, 1981). Figure 3-4 (Makogon et al., 2005) shows the reservoir pressure behavior and the corresponding gas production history at the Messoyakha Field. Figure 3-4 illustrates that since the production rates were reduced beginning in 1979, the average pressure has continued to increase.

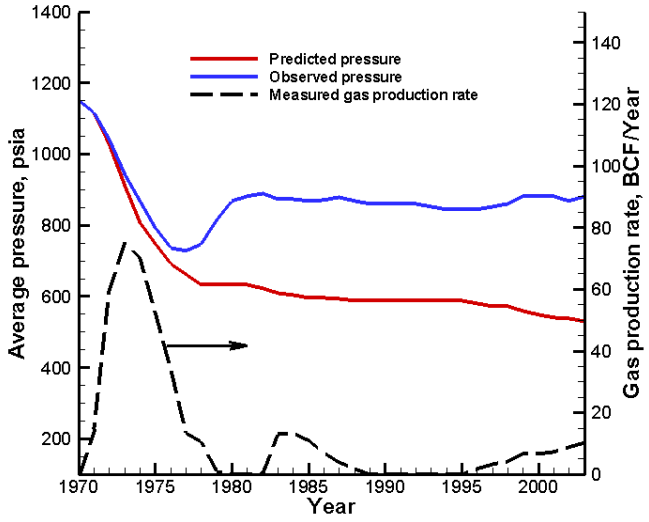

Figure 3-4 – Production behavior at the Messoyakha (from Makogon et al., 2005)

Gas reserves

The volumetric gas reserves (free gas + hydrated gas) in the Messoyakha field has been estimated by different individuals and ranges from 1.3 to 14 Tcf, as shown in Figure 3-5 (Krason and Finley, 1992). There is significant uncertainty in the estimates of gas trapped in the hydrate layer of the Messoyakha Field. Sheshukov (1973) calculated that 2.2 Tcf of gas was in hydrate form in upper portion of Messoyakha and 0.6 Tcf gas present as free gas in the lower portion of the Messoyakha. Makogon et al. (2005) reported that initial in-place gas (free-gas) at Messoyakha was 848 Bcf and the producible reserves from hydrate state were 424 Bcf. Figure 3-5 illustrates the uncertainty in the total gas reserves (free gas + hydrate gas) at the Messoyakha field.

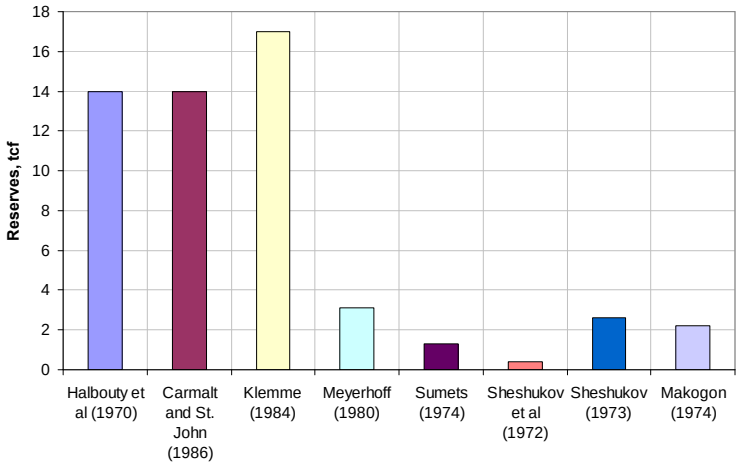

Figure 3-5 – Various estimates of gas in place in the Messoyakha field (data from Krason and Finley, 1992)

Production

The production rates from the wells that were completed within the hydrate layer were significantly lower than those from the wells that had been perforated deeper in the free gas zone of the reservoir. Table 3-1 shows the gas production rates from selected wells (Makogon et al., 1971a), as well as the location of the corresponding perforated intervals with respect to the original elevation of the base of the hydrate layer. The wells that were completed in the hydrate zone were stimulated by using chemicals such as calcium chloride and methanol. These chemicals inhibit the formation of gas hydrate, by causing the equilibrium curve to shift. After injecting the solvents, the wells could operate at higher wellhead pressures because of higher effective permeability in the vicinity of the perforations. Figure 3-6 (Makogon et al., 1971a) demonstrates the effect of methanol injection on the production rate Q_p of one of the wells in the Messoyakha Field.

Table 3-1 – Production from various perforation locations at the Messoyakha (from Makogon et al., 1971b)

Well No.	Percentage of perforations in hydrate zone (%)	Distance from perforations to hydrate-gas interface (m)	Production rate (1000 m^3/D)
121	100	+64	26
109	100	+6	133
150	81	-6	413
131	0	-59	1000

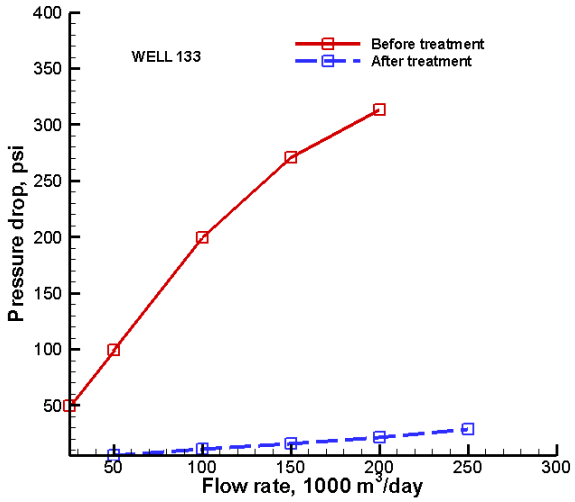

Figure 3-6 – Effect of chemical stimulation for Well 133 (data from Makogon et al., 1971)

Gas-water contact

The depth of the gas-water contact as reported in the literature (Krason and Finley, 1992) has been estimated to be between -779 to -819 m. According to Makogon et al. (2005) and Makogon (2007), the gas-water contact has not moved during the entire period of gas production at the Messoyakha Field.

Rock and Fluid Properties

The rock and fluid properties we used for the Messoyakha Field simulations are shown in Table 3-2 (Makogon et al., 1971a; Meyerhoff, 1980; Krason and Ciesnik, 1985; Krason and Finley, 1992; Makogon et al., 2005). The gas composition at Messoyakha is 98.8% methane.

Table 3-2 – Reservoir properties at the Messoyakha (from Makogon et al., 2005)

Property	Range
Porosity	16-38%
Permeability	10 to 1000 md
Geothermal gradient	4.2 °C/100m
Residual water saturation	29 to 50%
Initial reservoir pressure at "hydrate-free gas" interface	7.92e6 Pa (1150 psi)

Saturation Distribution

The only data available on saturation distribution of water, gas and hydrates in the respective zones (the upper hydrate zone and the lower free gas zone) is from Makogon et al. (2005). Average water saturation was described to be about 40%, salinity to be 1.5%,

and initial hydrate saturation to be about 20%. The saturation data discussed in Makogon et al. (2005) is tabulated in Table 3-3. If these saturations do occur during the initial "undisturbed" state of the reservoir, the hydrostatic pressures should exactly follow the equilibrium hydration pressure at each point within the hydrate layer. However, if methane and water coexist in a 3-phase regime, they are expected to react and form hydrate until the exhaustion of one of the two. The only possibility of occurrence of three phases in the hydrate layer is a finely balanced salt distribution, which would be next to impossible to maintain over long periods (as this would mean effective elimination of molecular diffusion). Because of the difficulty (if not impossibility) of meeting all these conditions, the coexistence of all 3 phases can not occur in the hydrate layer at the Messoyakha Field.

Table 3-3 – Average saturations at the Messoyakha (from Makogon et al., 2005)

Saturations	Hydrate layer	Free gas layer
S_H	20	0
S_A	40	40
S_G	40	60

The Messoyakha Field is a typical representative of a Class 1G hydrate deposit. Class 1G means that the hydrate layer consists of hydrate and gas and the lower free gas layer consists of gas and water. Such deposits are the most attractive targets for gas production, because while the free gas can be produced by conventional methods, the hydrate dissociation will keep recharging the gas into the reservoir and will contribute to the overall gas production.

In our opinion, the most reasonable description of the initial state of the Messoyakha field includes (a) a hydrate layer characterized by a 2-phase (gas and hydrate) regime, and (b) an underlying 2-phase zone of mobile fluids that include gas and water (often referred to as the "free gas zone").

Reservoir Modeling - Model Set-up

To simulate the Messoyakha field, we used the Tough + Hydrate model developed by Moridis (2003). We did not have enough data on all the wells to run a full field model. Instead, we used a series of 2-D cylindrical models representative of one of the wells in the Messoyakha Field.

Figure 3-7 illustrates the cylindrical domain used in this simulation study. The model radius was 400 m, resulting in a system with a volume equal to that of the Messoyakha well spacing of 500 x 1000 m. The thickness of the reservoir was 90 m. The model was discretized into 100 radial elements and 135 layers (a total of 13500 elements). The fine discretization scheme was necessary to capture the sharp front and rapid saturation changes occurring in the hydrate layer and in the vicinity of the well bore. The base case in this

study used an impermeable shale overburden and underburden, and no water drive. The input parameters for the base case are shown in Table 3-4.

Table 3-4 – Base case input parameters in T+H for the Messoyakha study

Property	Hydrate layer	Free gas layer
Thickness, m	50	40
Porosity, fraction	0.35	0.35
Gas production rate	6 MMscf/day	
Absolute permeability, md	500 md	500 md
Initial hydrate saturation, S_H	0.5	0
Initial gas saturation, S_G	0.5	0.5
Water saturation, S_A	0	0.5
Irreducible water saturation	0.28	0.28

Table 3-5 – Aquifer parameters for no hydrate case

Aquifer type	Aquifer permeability (k_{aqu})
Strong	500 md (Same as free gas layer)
Intermediate	1 md
Weak	0.001 md

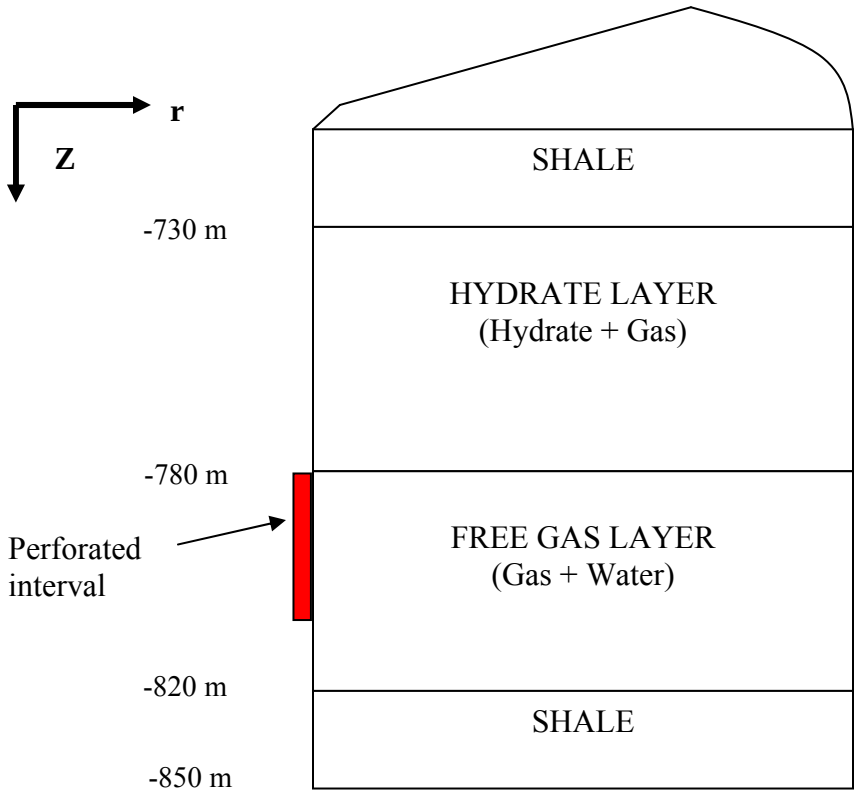

Figure 3-7 – Simulation model for the Messoyakha reservoir

Model Initialization

The initialization process in Tough + Hydrate has been discussed in detail in Moridis and Kowalsky (2005). The following assumptions were made to initialize the model:

1. Salinity was assumed to be zero. Since the upper portion of the reservoir includes only gas and hydrate, we cannot define salinity in this system. In other words, neither the "gas phase" nor the "hydrate phase" can account for salt. This is a reasonable approach, given that it is not known where the 1.5% salinity reported in Makogon et al (2005) was measured.
2. The initial pressure at the hydrate-gas interface is 7.92e6 Pa (1150 psia) which corresponds to the hydrostatic pressure at the base of the hydrate layer at the Messoyakha field. Based on the pressure at the base of the hydrate layer, the temperature is about 10.88°C (for 3-phase methane-hydrate-water) equilibrium which is close to 10°C isotherm defined in (Makogon et al., 2005).

The initialization process involves the determination of the correct initial pressure and temperature distribution along a single column that is used as a stencil for the entire domain. Figure 3-8 shows the initial conditions for base case in the model. The shale boundaries at the top and bottom of the reservoir in the model were 30 meters thick. This thickness was based in the earlier scoping studies by (Moridis, 2003; Moridis and Kowalsky, 2005) and "was sufficient to accurately represent heat exchange with the hydrate deposit"(Moridis and Kowalsky, 2005). More detail on the initialization process can be found in the dissertation by Grover (2008).

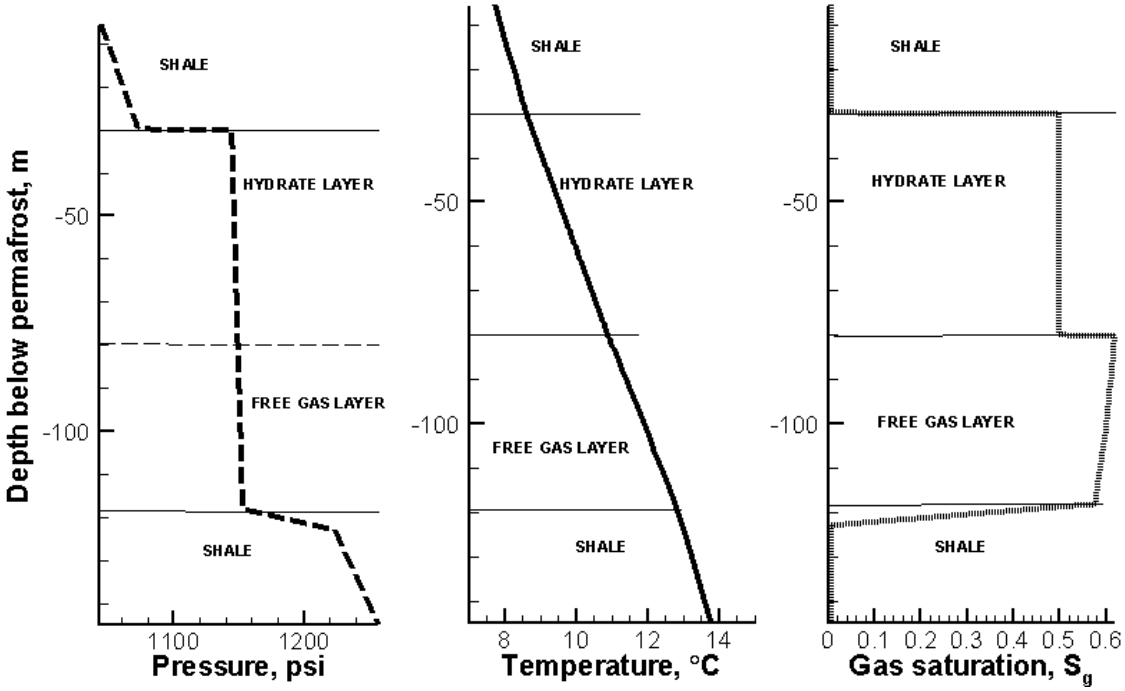

Figure 3-8 – Initial conditions for the base case in Tough + Hydrate

Production Parameters

Gas was produced at a volumetric flow rate of 6 MMscf/day. The well was completed from 0.5 m below the base of hydrate layer (BHL) to 16.5 m below the BHL (thickness of the perforated interval is 16 m).

Contribution of hydrates to overall gas production

Moridis and Kowalsky (2005) introduced the concept of "Rate Replenishment Ratio (RRR)" and "Volume Replenishment Ratio (VRR)" for production from Class 1 hydrate deposits. These two are defined as follows:

$$RRR = \frac{Q_r}{Q_p}$$

$$VRR = \frac{V_r}{V_p} = \frac{\int_0^t Q_r(t)dt}{\int_0^t Q_p(t)dt}$$

where Q_r is the CH_4 release rate in the reservoir, Q_p is the CH_4 production rate at the well, V_r is the cumulative volume of CH_4 released and V_p is the cumulative volume of CH_4 produced.

Base Case Results and Analysis - Base Case with No Water Drive

We ran the base case for 8 years at a constant production rate and then shut in the well for 3 years. The results showing the reservoir pressure and temperature during the 8 years of production are presented in Figures 3-9 and 3-10, respectively. The gas-phase pressure distribution (along the z-axis at r = 50 m) in Figure 3-9 indicates that, when gas production begins, the gas pressure is essentially uniform in both the hydrate layer and the underlying free gas zone. Figure 3-10 shows that the temperature in the reservoir decreases because of the dissociation of hydrates. The decreasing temperature exhibits the "bottleneck" to gas production from hydrates because less heat is available to transfer to hydrates for continued dissociation.

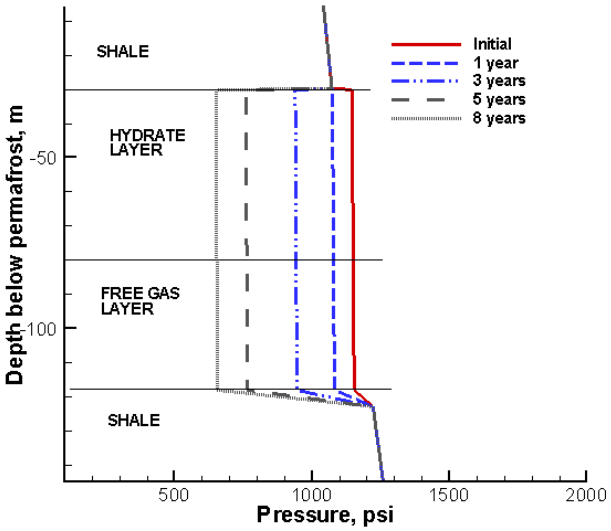

Figure 3-9 – Evolution of the pressure distribution of the gas phase along the z-axis at r = 50 m for the base case run

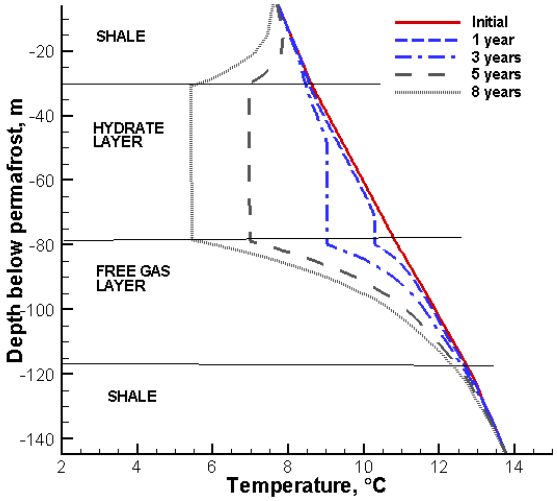

Figure 3-10 – Evolution of the temperature distribution along the z-axis at r = 50 m in the base case of the Messoyakha study

Figure 3-11 shows the thermodynamic path at the bottom and at the top of the hydrate layer, at r = 50 m from the wellbore. Initially, the hydrate-gas interface is at the equilibrium curve and the top of the hydrate layer is away from the equilibrium curve. When the gas is produced from the free gas portion of the reservoir, gas hydrate in the hydrate layer dissociates due to depressurization and starts charging the free gas portion of the reservoir. The pressure and temperature regime in the hydrate layer follows the equilibrium curve as production continues until the hydrate is completely dissociated. The hydrate becomes completed dissociated at the base of hydrate layer after slightly over 3 years of production. After production stops at t = 8 years, the temperature begins to increase because of (a) continuous geothermal heat flow from the top and bottom boundaries towards the hydrate zone, (b) drastic reduction of dissociation with the interruption of

production, and (c) practical elimination of flow, and of the corresponding Joule-Thomson cooling. In addition, the pressure increases because of temperature increase in a system with a fixed volume, pressure equilibration within the reservoir, and continued net hydrate dissociation.

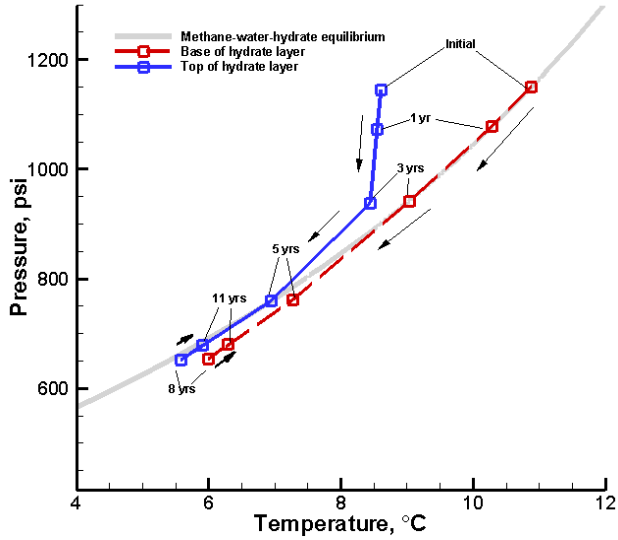

Figure 3-11 – Thermodynamic path during gas production for the base case

Figure 3-12 shows the methane release rate from the hydrate dissociation in the reservoir. The spikes in the methane release rates in Figure 3-12 are related to the gridding in the model and indicate that a hydrate layer in the model has dissociated completely. As the gas is produced (at a constant rate) from the free gas portion, the gas release rate continues to increase. The increase in gas release rate means that the gas hydrates are dissociating more vigorously as time advances. At 2880 days of gas production, the gas release rate in the reservoir (Q_r) reaches about 2.5 MMscf/day. The gas production rate at the well Q_p is 6 MMscf/day. Hence, the rate replenishment ratio (RRR) at the end of 2880 days is about 42%. The VRR reaches about 22% after 8 years of production.

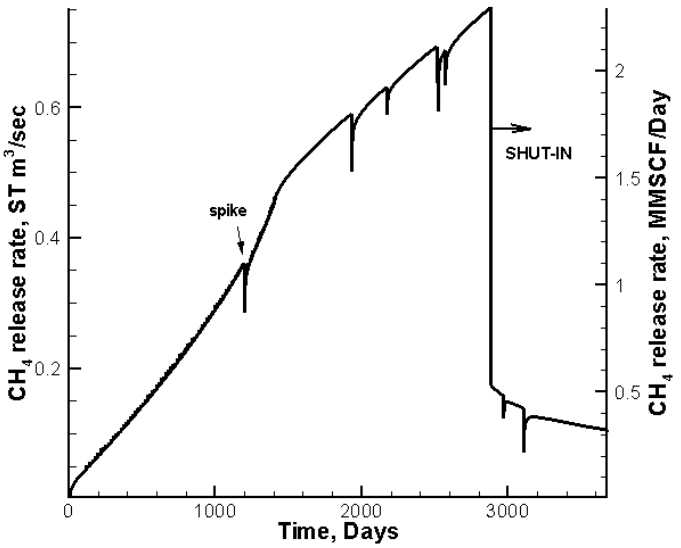

Figure 3-12 – Methane release rate for the base case

Another important effect observed in the simulations was the formation of secondary hydrates in the vicinity of the top of the perforations close to the hydrate-gas interface. In the base case, the top of the perforated interval is about 0.5 m away from the hydrate-gas interface. When gas is produced, cooling occurs because of the endothermic nature of the gas-releasing hydrate dissociation, and because of Joule-Thomson cooling caused by depressurization and high gas velocities near the well. The availability of gas and water (either native or originating from hydrate dissociation) and the continuing cooling lead to the formation of secondary hydrate near the well, where the gas velocity is at its highest and the temperature at its lowest level in the reservoir. The formation of secondary hydrates can lead to higher pressure drops around the perforations and eventually choking of the well causing essentially complete blockage of flow. The formation of secondary hydrates is illustrated in Figure 3-13, which shows such hydrates around the well after 180 days of production. However, for the base case, the effect was not important later during the production because of fluid mixing with the warmer gas from the free gas portion of the reservoir. The perforations very close to the hydrate-gas interface may exhibit secondary hydrate formation around the well during initial the early stages of production.

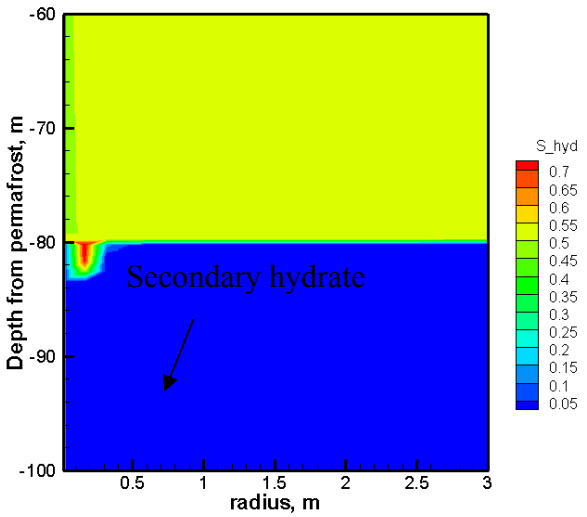

Figure 3-13 – Formation of secondary hydrate for base case at 180 days

Base Case with Water Drive

The literature is not clear about the strength of the aquifer at Messoyakha. Makogon et al. (2005) suggests that the gas-water contact has not moved during the last 30 years of production. However, water influx is a potential mechanism that could cause the reservoir pressure to increase during the time the field was shut-in, so we decided to simulate the addition of an aquifer to our base case. To model the effects of an aquifer, we had to develop and initialize a new modeling grid. Figure 3-14 shows the initial pressure and temperature conditions in the reservoir. The capillary pressure parameters were changed to give the initial gas saturation and water saturation profiles shown in Figure 3-15.

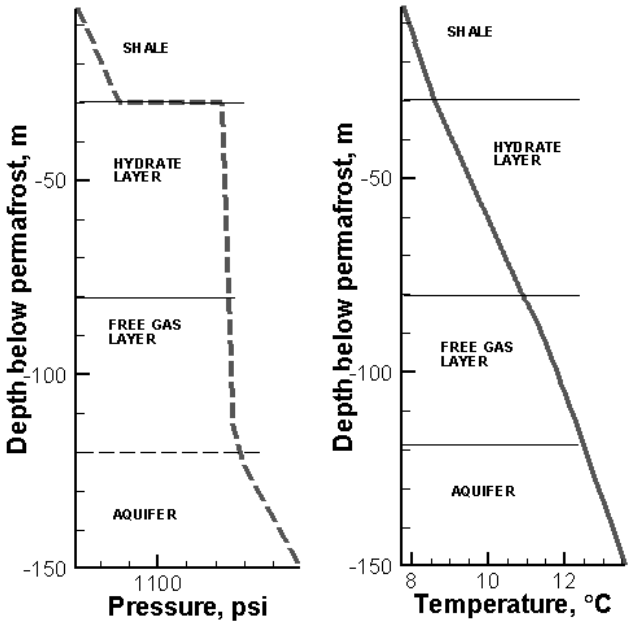

Figure 3-14 – Initial pressure and temperature conditions for water drive case

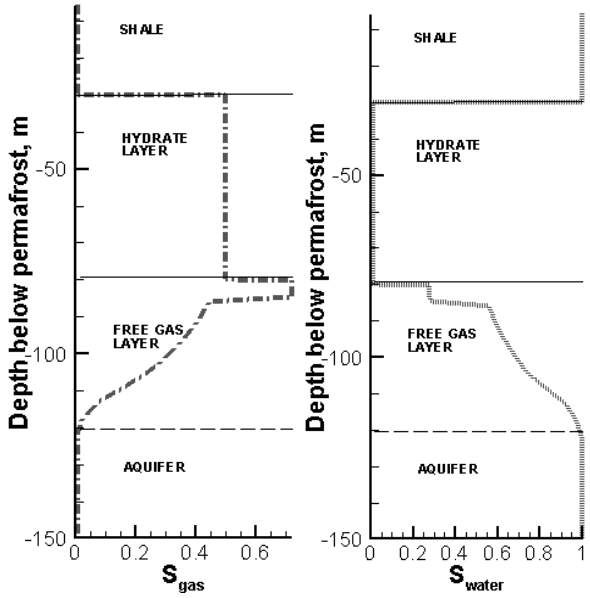

Figure 3-15 – Initial gas saturation and water saturation profiles for water drive case

If the aquifer was modeled as a strong aquifer, the water from the aquifer displaced the free gas near the well bore very quickly. Because of the low temperature and the increased availability of water, secondary hydrates form near the well, and reach saturations that are sufficiently high to block flow, thus resulting in the cessation of production (Figure 3-16). When Q_p = 6 MMscf/day, it takes about 10 days for gas hydrates to form at the perforations and block gas flow. The formation of secondary hydrates around the perforations occurs in the presence of strong water drive. Moreover, in the simulation

results, it was observed that the rapidly rising water from the aquifer, starts forming more hydrate in the hydrate layer.

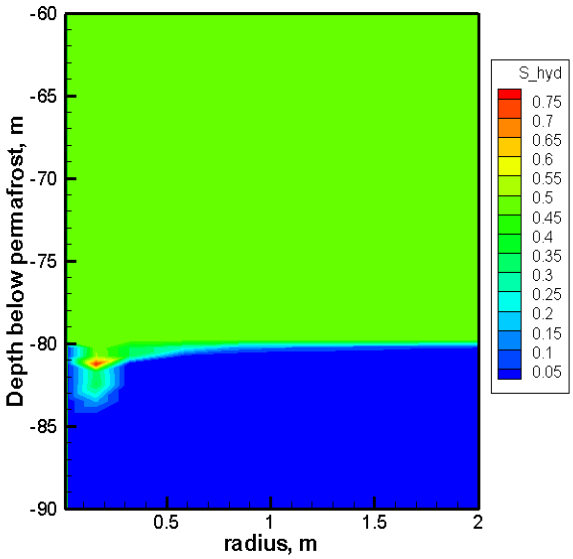

Figure 3-16 – Pressure map for the water drive case after 10 days

Comparing the simulation results for various strength aquifers and the observations of Makogon that no movement in the gas-water contact has occurred, we concluded that the aquifer at the Messoyakha has to be weak and does not play any significant role during the gas production from the Messoyakha field.

Sensitivity analysis

In the dissertation by Grover (2008), a large number of sensitivity cases were run to investigate how gas hydrates could have affected gas production in the Messoyakha field. Results of the most pertinent of these sensitivity studies is described below.

Sensitivity to hydrate layer permeability

As this research progressed, it was clear that lower intrinsic permeability in the hydrate layer tended to result in enhanced reservoir pressure increase after the well was shut-in. By determining the pressure response of the system to various levels of permeability in the hydrate layer, it was also possible to test the suggestion of Makogon et al (2005) that the reservoir pressure continued to increase in Messoyakha after the wells were shut-in and the pressure increase was due to continued gas hydrate dissociation.

All reservoir and fluid parameters, other than the permeability in the gas hydrate layer, remained the same as in the base case. We looked at three cases, Cases 2A, 2B, and 2C where the permeability in the gas hydrate layer was 0.01, 0.1 and 1.0 md., respectively. These low values of vertical permeability can easily be explained by the thin shale layers that are known to exist in the Dolgan formation. Figure 3-17 shows the thermodynamic path of conditions at the top and bottom of the hydrate layer for Case 2B at r = 50 m from

the well. When compared with the thermodynamic path for base case, it can be seen that as the production continues, the pressure difference (Δp_t) between the top of the hydrate layer and the bottom of the hydrate layer continues to increase. Δp_t is the result of very low effective gas permeability in the hydrate. Because of lower effective permeability in the hydrate layer for Case 2B, as compared to that of base case, the gas flow through the hydrate layer is reduced. At the bottom of the hydrate layer (and in the free gas layer), the gas flows much easily because of high effective permeability.

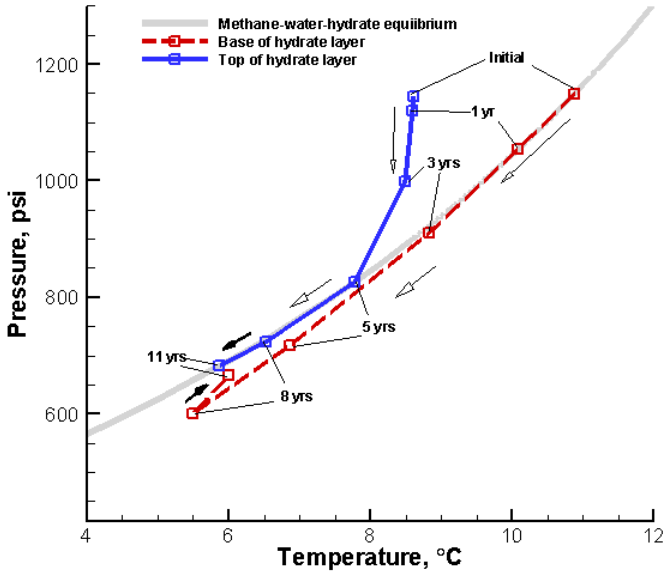

Figure 3-17 – Thermodynamic path of conditions at two points at r = 50 m during gas production where khydrate = 0.1 md

The bottom of the hydrate layer (h_{bottom}) dissociates in less than 3 years and the thermodynamic conditions for h_{bottom} start to deviate away from the equilibrium curve. The thermodynamic conditions of top of the hydrate layer (h_{top}) are still on the 3-phase equilibrium curve. After 3 years of shut-in (at time = 11 years) the conditions of h_{bottom} moved very close to the equilibrium curve (Figure 3-17). The temperature increases because of the heat flow during the shut-in period, which results in continued hydrate dissociation and hence pressure increases in the h_{bottom} and free gas layer. The conditions of h_{top} are such that after shut-in, the pressure and temperature still follows the equilibrium curve downwards (solid arrow) and pressure and temperature continues to decrease at h_{top}. The permeability is so low in the hydrate layer that a pressure gradient persists between the top and the bottom of the hydrate layer, leading to flow and continuing dissociation. The temperature profile (Figure 3-18) for Case 2B, where the permeability in the gas hydrate layer is 0.1 md., is such that after the shut-in of the well, the temperature differential between h_{top} and h_{bottom}, results in more dissociation at h_{top} and charging of that gas towards h_{bottom}.

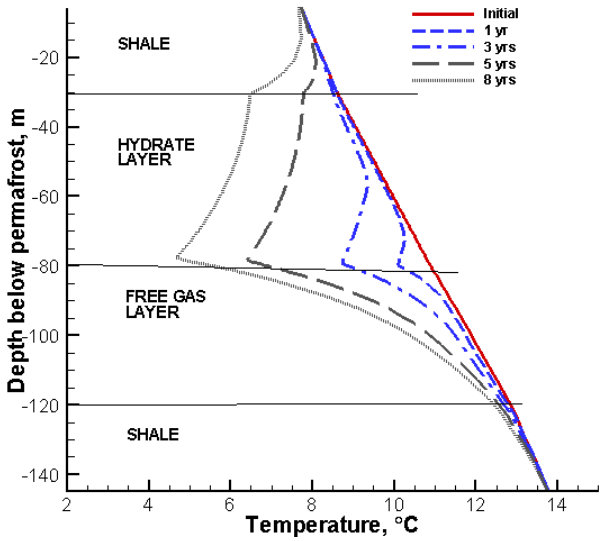

Figure 3-18 – Evolution of the temperature distribution along the z-axis at r = 50 m where khydrate = 0.1 md of the Messoyakha study

Figure 3-19 illustrates the average pressure (p_{avg}) in the free gas layer plotted as a function of time. p_{avg} increases when the well is shut-in and the permeability of the hydrate layer is lower than that of the free gas zone. When the well is shut-in, there is a substantial pressure differential between the hydrate layer and the free gas layer below keeps hydrates dissociating vigorously even after shut-in. **For the cases where the vertical permeability is either 0.01 or 0.1 md, the pressure increase after shut-in is similar to the pressure behavior observed at Messoyakha field.** Even if only a portion of the hydrate bearing layer at the Messoyakha Field has low permeability, due to thin shale layers or some other factor, it could have led to higher measured pressures in the free gas layer during the shut-in.

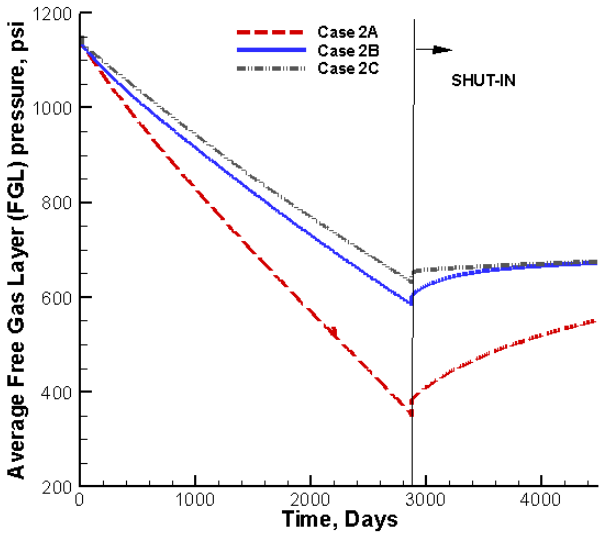

Figure 3-19 – Average free gas layer pressure (pavg) profiles for Cases 2A, 2B and 2C

Figure 3-20 shows the methane release rate in the reservoir during production and after shut-in for Cases 2A, 2B and 2C, where the permeability in the gas hydrate layer was 0.01, 0.1 and 1.0 md., respectively. All three curves show that as much as 15 – 20% of the gas produced at Messoyakha could have come from the gas hydrate zone.

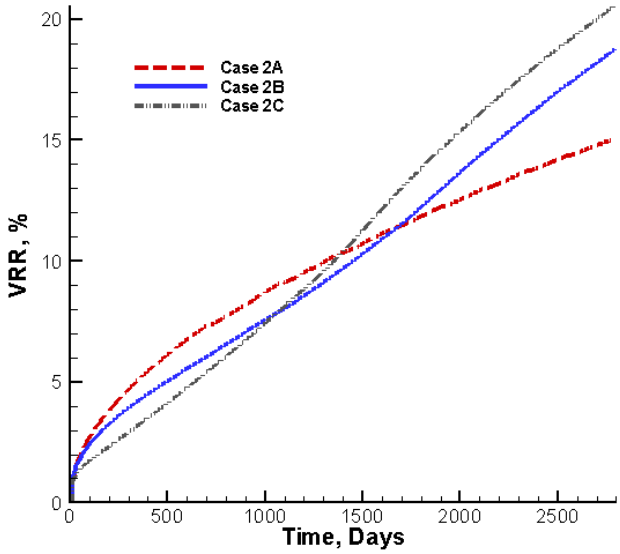

Figure 3-20 – Volumetric Release Rates for Cases 2A, 2B and 2C

Other Sensitivity Analyses

In the dissertation by Grover (2008), additional sensitivity cases were also run to investigate how gas production from the Messoyakha has been affected by the presence of the gas hydrate layer above the free gas zone. Sensitivity cases were run to investigate the following parameters:

- absolute permeability in free gas layer,
- hydrate saturation,
- the well completion interval,
- the gas flow rates, and
- the case where no gas hydrate existed.

For the case where we simulated Messoyakha with no gas hydrate, we wanted to test if the pressure response at the Messoyakha can be reproduced if it is assumed that there were no hydrates present in the reservoir. To simulate the no hydrate case, it was necessary to initialize the model differently. Gas and water were assumed to be present, overlain by shale and underlain by an aquifer. In the analysis of the reservoir sensitivity to the aquifer strength when no hydrates are present, we investigated three cases. In these run, we could manage to model the pressure decrease during production and the pressure increase during shut-in as observed in Messoyakha. However, if one accepts the observation that the gas-water contact at Messoyakha has not moved during the life of the field, then the cases with an aquifer and no gas hydrates can not be accepted as plausible.

Conclusions

On the basis of our reservoir simulation results for a reservoir with properties similar to the Messoyakha Field, we present the following conclusions:

1. Our simulation results indicate that the published description of the Messoyakha Field as a hydrate layer, underlain by a free gas layer, and a weak aquifer is the correct description.
2. As the gas in the free gas layer was produced, the pressure and temperature declined, and as much as 15-20% of the gas produced during the early years at Messoyakha came from gas hydrate dissociation.
3. We simulated the reservoir pressure increase after the wells were shut-in in 1979 by decreasing the vertical permeability in the gas hydrate zone to 0.01 to 0.1 md. These values of vertical permeability are likely caused by the thin shale layers that exist in the Dolgon formation.
4. Our modeling shows that if the perforations are close to the hydrate-gas interface, the rapid cooling due to both hydrate dissociation and the Joule-Thomson cooling effect will lead to the formation of secondary hydrates around the perforation (perforation choking). The formation of secondary hydrates will lead to reduction in permeability (essentially a damaged zone) that can lead to a rapid decrease in gas flow rates. The damage can be removed by injecting solvents or heat to melt the secondary gas hydrates.
5. We need to know for sure if the gas-water contact at Messoyakha has moved during the life of the field. If we believe that the gas-water contact has not moved with time, the increase in pressure due to continued hydrate dissociation after shut-in is a plausible scenario. Otherwise, the increase of reservoir pressure can be simulated using an intermediate strength aquifer.

Chapter 4 – Offshore Hydrate Deposits

Introduction

Gas hydrates are distributed around the Continental margins. Figure 4-1 illustrates various areas around the world where hydrates are thought to exist (Makogon et al., 2007).

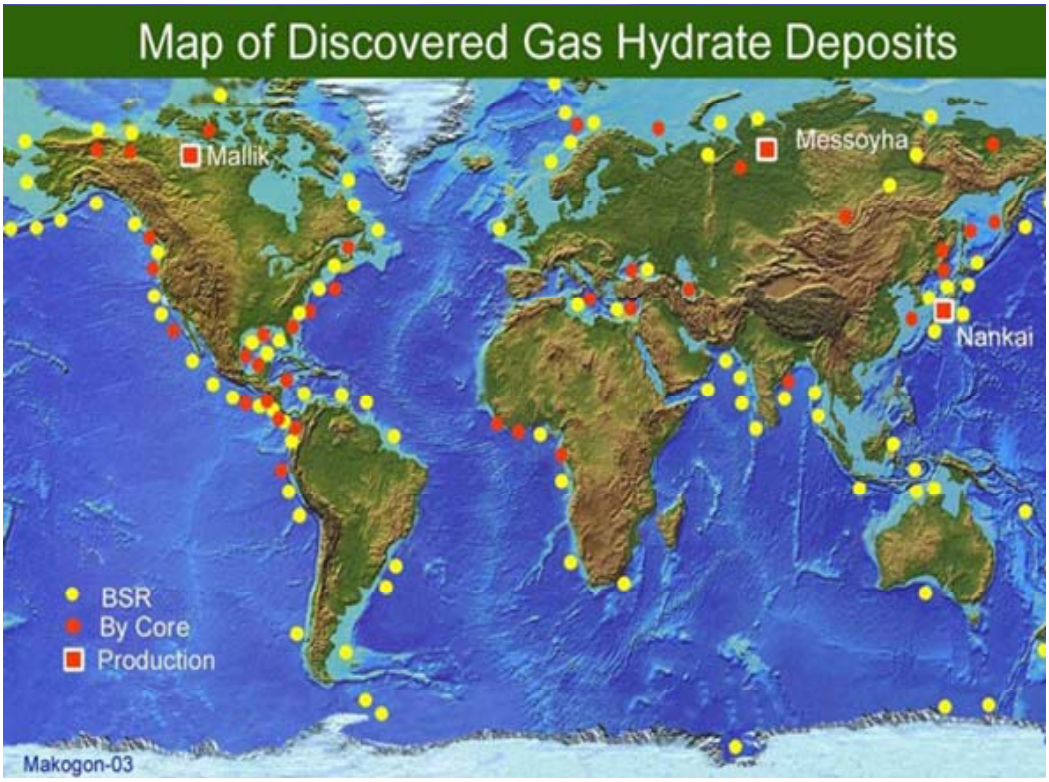

Figure 4-1 – Distribution of hydrates around the world (from Makogon et al., 2007).

The known gas hydrate deposits were discovered either from a BSR or by drilling wells into the sediments. The oceanic hydrate resource is believed to be huge as compared to onshore hydrates in or below the arctic permafrost (Sloan and Koh, 2008).

Oceanic hydrates have been found in different geological settings such as convergent and divergent margins (Milkov, 2005). Although numerous small expeditions conducted have studied the-near-seafloor hydrates, only a limited number of expeditions have been conducted where deep boreholes were drilled and have acquired samples from various depths. There is still a great deal of uncertainty surrounding the location and volume of gas hydrate deposits in the ocean. We know where some deposits exist because we have found them. However, most of the ocean is unexplored for gas hydrates.

Important data such as water depths, geothermal gradients, gas compositions and sediment properties has been collected from various literature sources for the offshore gas

hydrate deposits. Efforts wee concentrated on offshore hydrate deposits because of project focus on studying the seafloor stability issues in hydrate bearing sediments. The most relevant data are described in the following sections.

Various hydrate expeditions have been carried out by the Ocean Drilling Program (ODP), the Japanese Government (Nankai Trough) and the Chevron/US Department of Energy (DOE) joint industry project (JIP) (Gulf of Mexico). The lithological and mineralogical details are reported for the hydrate bearing sediments in the following sections.

Blake Ridge

The Carolina rise, particularly along the Blake Ridge, was one of the areas where marine gas hydrate was first identified on the basis of bottom simulating reflector (BSR) data.

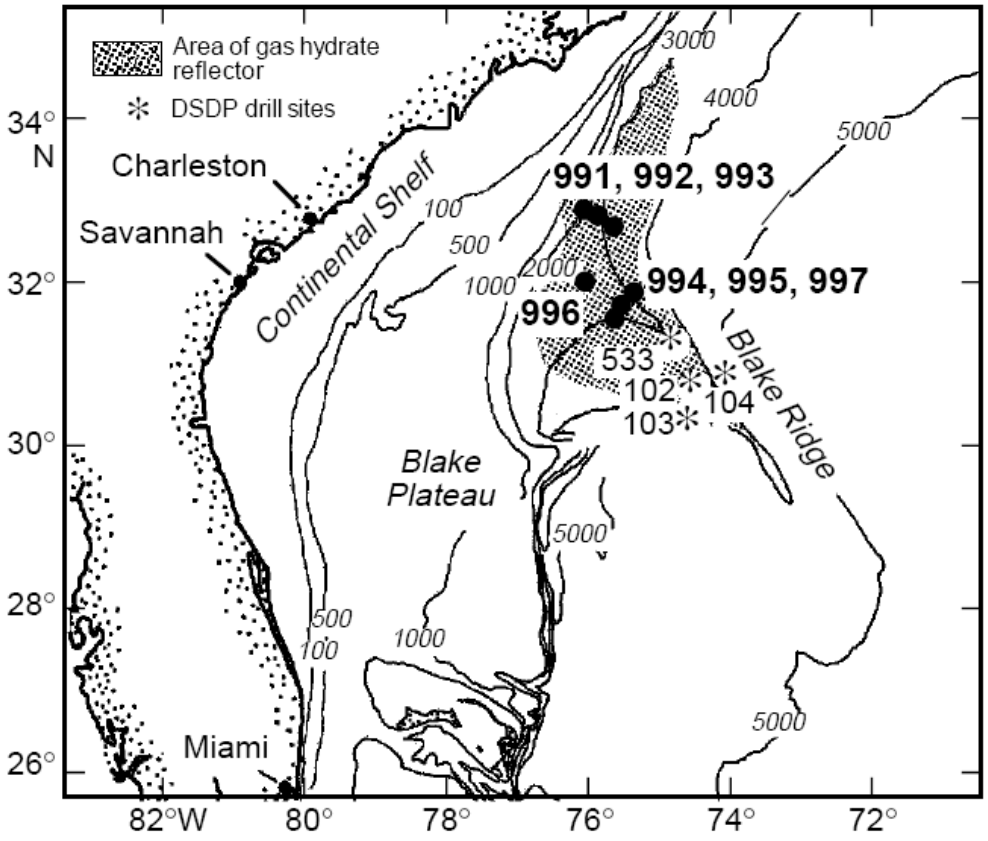

Figure 4-2 – Map of the Blake Ridge (from Shipboard Scientific Party, 1996).

Figure 4-2 shows the map of the possible area of gas hydrate occurrence on the basis of where the BSR can be identified from seismic. A total of seven sites (991 to 997) and 17 wells were drilled in the Blake Ridge region. A number of large solid gas hydrates samples were recovered from sites 994, 996, and 997. The samples from sites 994 and 997 were either nodular or thick massive pieces of gas hydrate. X-ray computed tomography, diffraction, nuclear magnetic resonance and Raman spectroscopy gave results that indi-

cated the gas was essentially 100% methane. Thermal conductivity values of gas hydrates from Blake Ridge range from 0.3 to 0.5 W/m/K. Equilibrium dissociation indicated that the equilibrium curve is almost the same as that of pure synthetic methane hydrate.

A large amount of microbial gas was encountered at the previous Deep Sea Drilling Project (DSDP) drill sites on the Blake Ridge and no indications of thermogenic gases were noted in these holes. At site 994, the sediments were very gassy. The probability of finding gas hydrate in this hole was high (>50%) at depths from 100 to 450 meters below the sea floor (mbsf) because of low chlorinity values in the pore water. The average geothermal gradient in this area was found to be 35.4 °C/km. The gas hydrates were recovered from nanofossil-rich clay at a sub-bottom depth of 260 to 330 m, about 200 to 120 meters above the BSR. The traditional method of core description does not work for gas hydrates because the hydrates are unstable at surface conditions. For this reason, different proxy techniques were used for the estimation of hydrate concentration in the pores. Using the chloride values, the gas hydrate concentration of some samples was as high as 14%. On the average, the values of 1.3%, 1.8% and 2.4% of the sediment above 450 mbsf was filled with gas hydrates at sites 994, 995, and 997. Gas volumes from the Pressure Core Sampler (PCS) indicated the range of hydrate concentration to be in between 0% and 9%. Seismic data from vertical seismic profiles indicate that the sediments contain at least 2% gas hydrates.

Nearly as much gas hydrate was inferred to occur at site 994 (no BSR present) as with sites 995 and 997 (where extensive BSR was present). This demonstrates that gas hydrates may be present at a given location even if a BSR is not identified by seismic. Sites 991, 992, and 993 were the diapir sites. Shallow holes (50 to 60 mbsf) were drilled on the flanks and crest of the Cape Fear Diapir and Blake Ridge Diapir. The sediments from these three sites were strongly deformed.

Cascadia Margin

Figure 4-3 shows the expeditions performed in the Cascadia Margin, by the Ocean Drilling Program (ODP) Leg 168, 204 and International Ocean Drilling Program (IODP) Expedition 311.

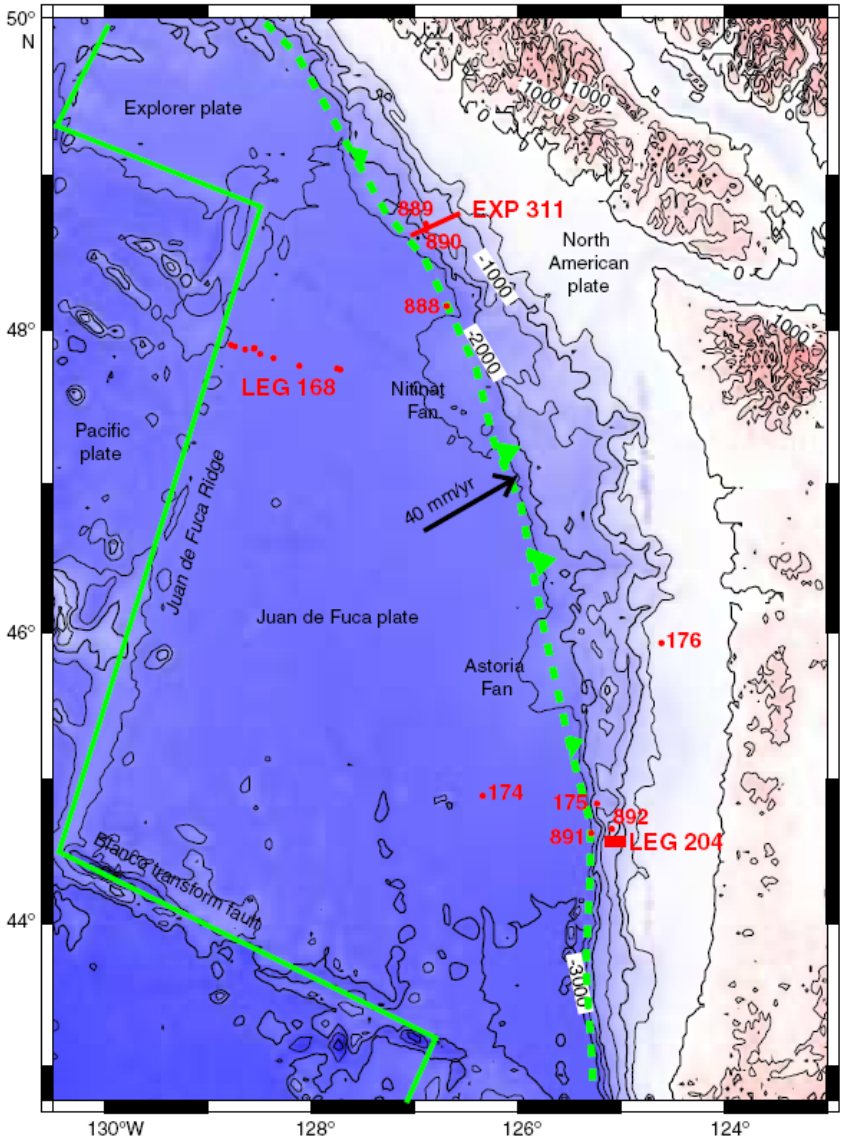

Figure 4-3 – Map of drilling sites at Cascadia Margin (from Trehu et al., 2006).

Leg 311 targeted a segment of northern Cascadia Margin where the sediments were coarser grained. The sediments encountered during the Leg 204 were finer grained. Leg 204 was carried out at Hydrate Ridge.

Hydrate Ridge is a 25-km long and 15-km wide ridge in the Cascadia accretionary complex, formed as Juan De Fuca plate subducts obliquely beneath North America at a rate of ~4.5 cm/year (Shipboard Scientific Party, 2003). Sediment on the subducting plate contains large volumes of sandy and silty turbidites. Hydrate Ridge is characterized by a northern summit at a water depth of ~600 m and a southern summit at a water depth of ~800 m (Figure 4-4).

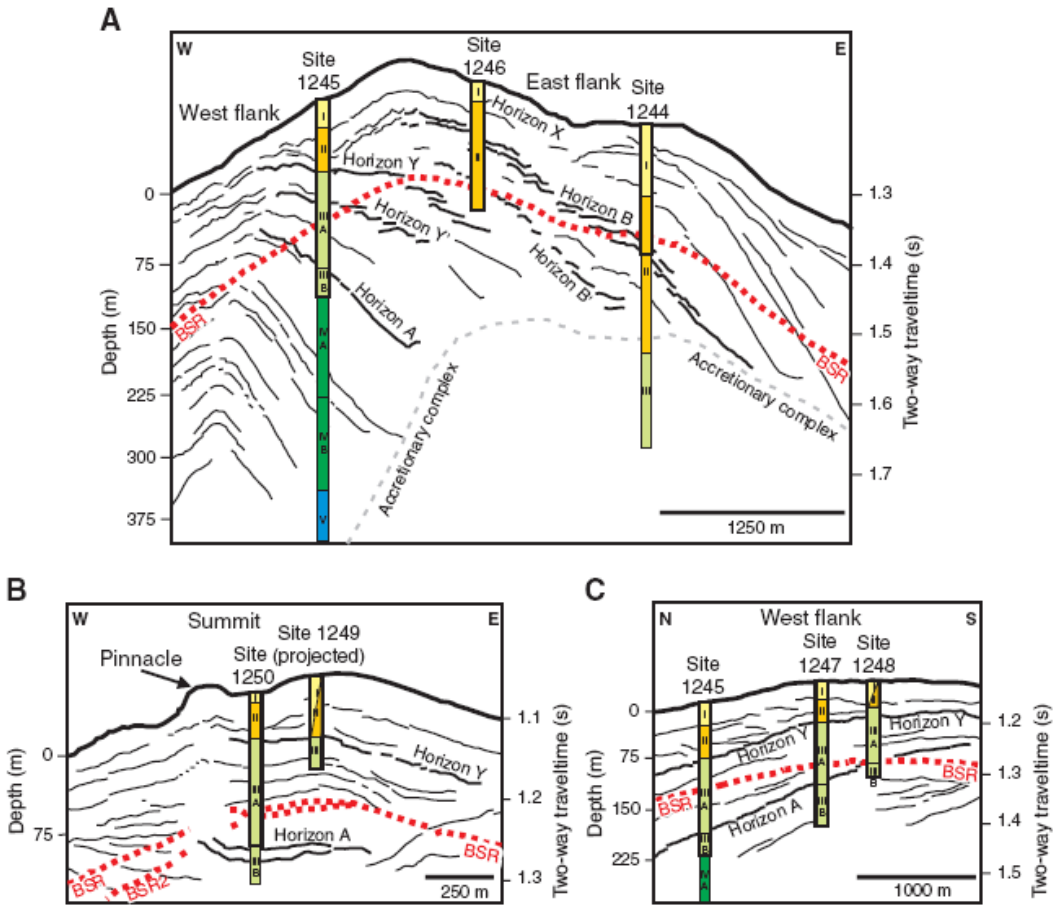

Figure 4-4 – Drilling sites during Leg 204 (from Gracia et al., 2006).

ODP Leg 204 was the first expedition to evaluate gas hydrates distribution in accretionary complexes. The distribution of gas hydrates in the nine sites and 45 wells is very heterogeneous, both laterally and vertically. The gas hydrates are present in the form of lenses and nodules of sub-millimeter to centimeter thickness. These lenses and nodules occur in clusters, and are several meters thick, and have orientations ranging from horizontal to vertical (Janik et al., 2003; Trehu et al., 2004; Abegg et al., 2006). Gas hydrates are usually present along the vertical fractures and do not significantly alter the sediment stiffness. The gas hydrate distribution at Cascadia Margin is a result of two different regimes of gas transport in the sediments, low flux settings and high flux settings (see Chapter II).

The water depths at Cascadia Margin drilled wells range from 790 to 1200 meters. The calculated geothermal gradient from the temperature measurements at different wells has an average value of 55°C/km. The BSR is present ubiquitously throughout the Hydrate ridge. A total of 13 hydrate bearing samples were subjected to X-ray Diffraction (XRD) measurements. Out of the 13 samples, 8 samples showed the hydrate concentration ranging from 1 to 7%. Five samples showed higher gas hydrate concentrations ranging from 20 to 70%. Detailed fabric analysis of the recovered samples showed that the gas hy-

drates were present in layers with different dips. In the shallow sediments (<40 m below seafloor) the gas hydrate layers were found to be parallel or subparallel to the bedding planes. At depths greater than 40 m, gas hydrate layers were found to be present at steeper dip angles (30° to 90°). The gas hydrates were interpreted to be fracture filling at these steeper angles.

Figure 4-5 illustrates the drilled wells at Cascadia Margin during Leg 204. The BSRs are shown in the cross-section and the color contours show the calculated gas hydrate saturations.

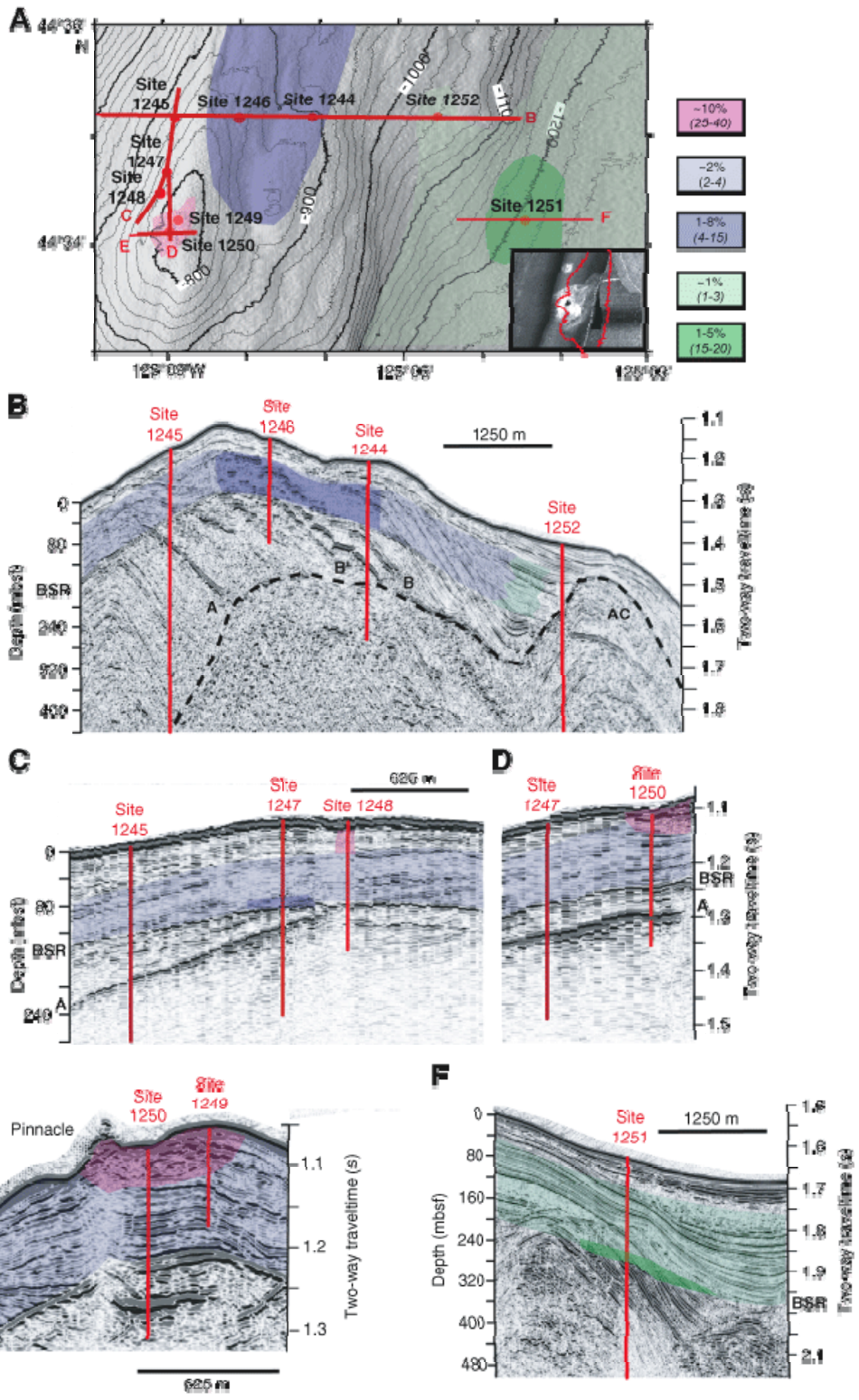

Figure 4-5 – ODP Leg 204 drill sites. Color contours refer to calculated gas hydrate saturations. Numbers in paranthesis refer to figure parts B-F (from Trehu et al., 2006).

Gulf of Mexico

Gas hydrates have been recovered in more than 53 sites in the northwest portion of the Gulf of Mexico (GOM) at water depths of 440 to 2400 m (Sassen et al., 1999a). According to Krason and Ciesnik (1985), the total volume of hydrate-bound gas in the GOM is estimated to be between ~0.5 and 255 x 10^{12} m^3. BSRs are rare in the GOM and no relationship has been observed between the presence of actual hydrates and the geophysical signatures. Sassen et. al. have performed numerous field sample studies from the shallow sediments from the GOM. There have also been two cruises in the GOM, namely Leg 96 of Ocean Drilling Program and the Chevron/DOE JIP work in 2005.

Although the GOM originated as a passive Continental margin, it is tectonically-active with complex geological features. These features are faults, folds and salt piercements. The main characteristic in the GOM that is different from other continental margins is that hydrates are found in the shallow sediments. In other Continental margins (e.g. Blake Ridge, Costa Rica margin, Cascadia margin and Nankai accretionary margin) the top of the GHSZ for methane gas is found from tens to hundreds of meters below seafloor. Figures 4-6 to 4-13 (Milkov and Sassen, 2003) illustrate some of the areas studied for hydrates in the Gulf of Mexico.

Gas hydrates in Gulf of Mexico occur in various forms; from seafloor to deeper sediments.

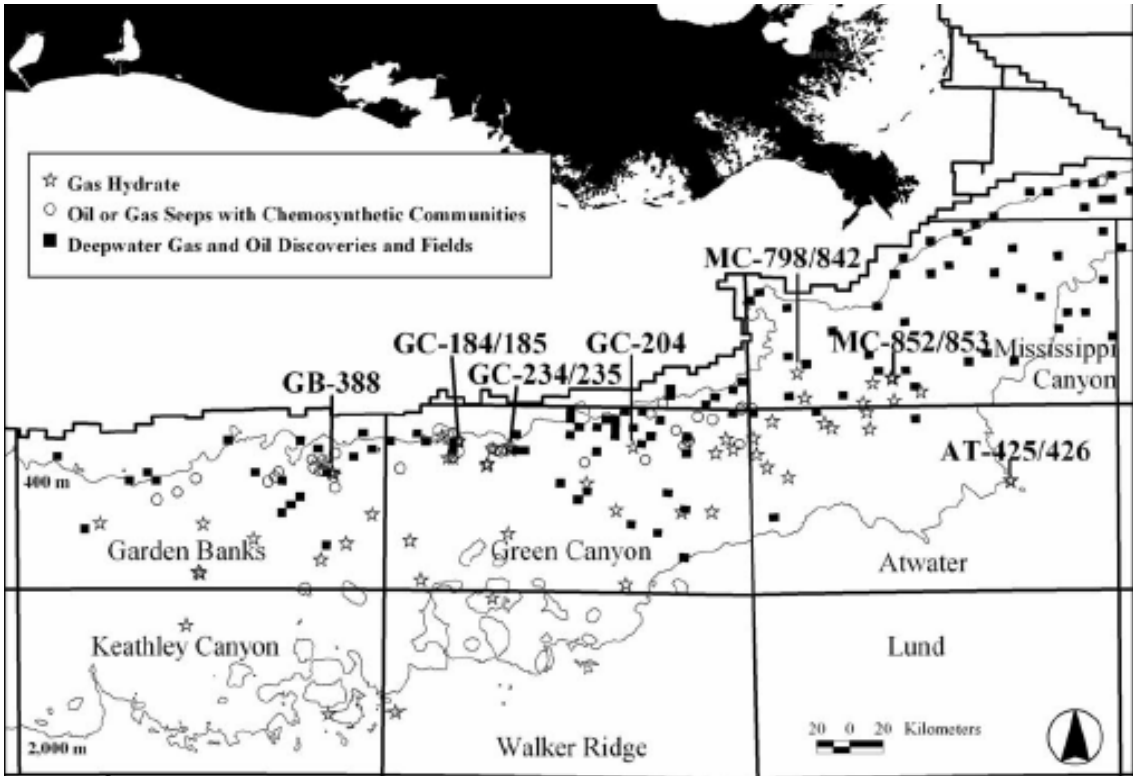

Figure 4-6 – Hydrate study locations at Gulf of Mexico (from Milkov and Sassen, 2003).

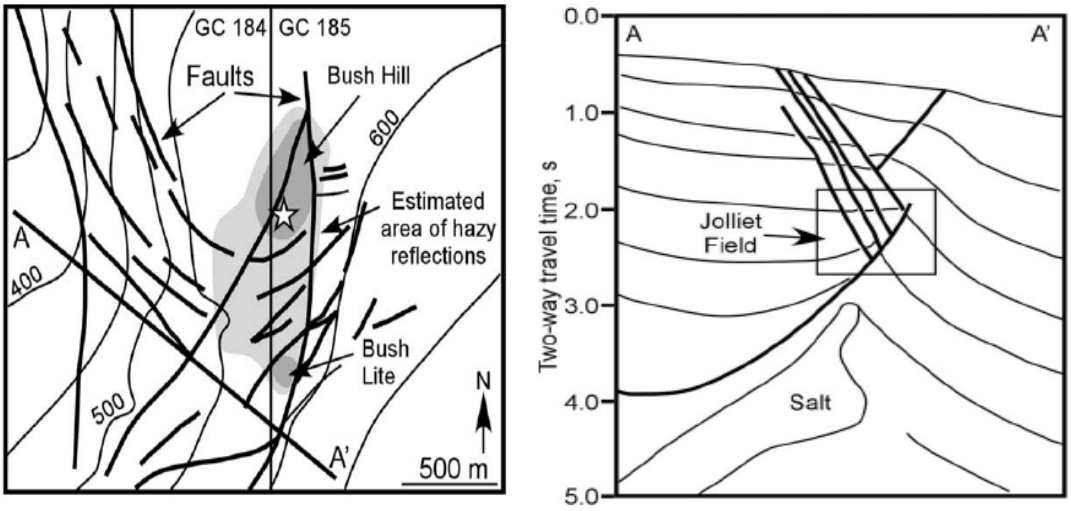

Figure 4-7 – Green Canyon 184/185 map and cross section (from Milkov and Sassen, 2003).

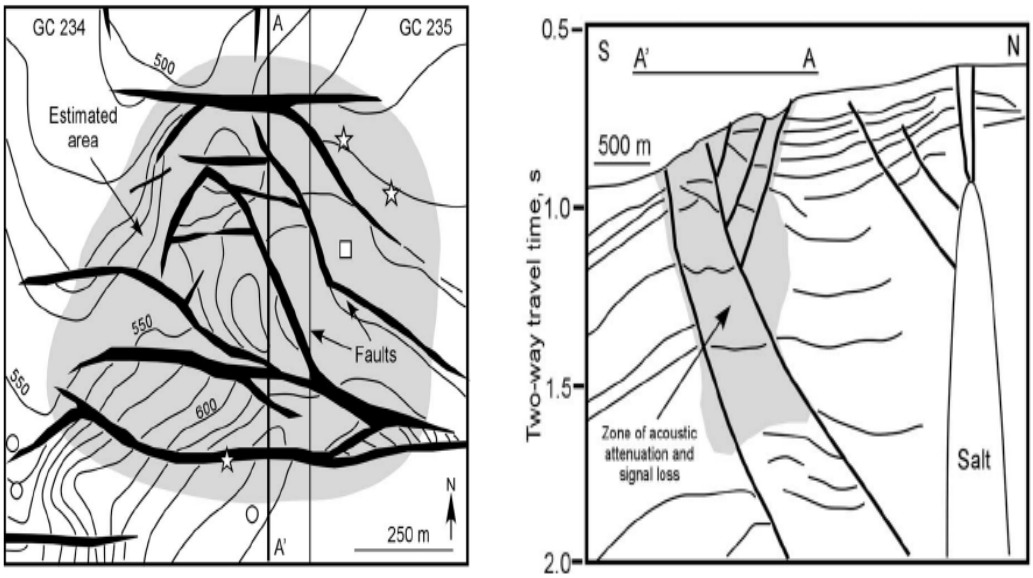

Figure 4-8 – Green Canyon 234/235 map and cross section (from Milkov and Sassen, 2003).

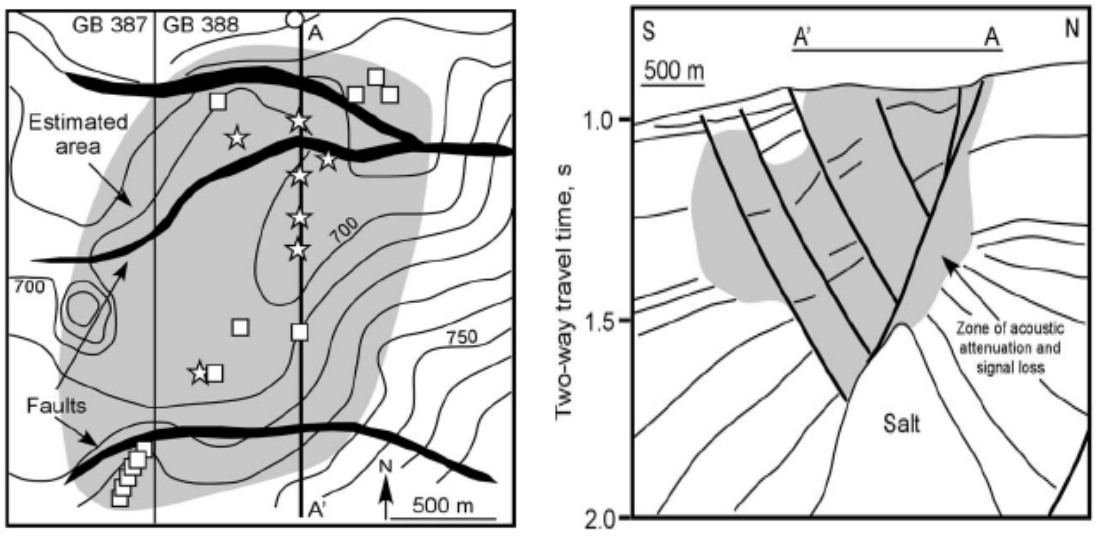

Figure 4-9 – Garden Banks 387/388 map and cross section (from Milkov and Sassen, 2003).

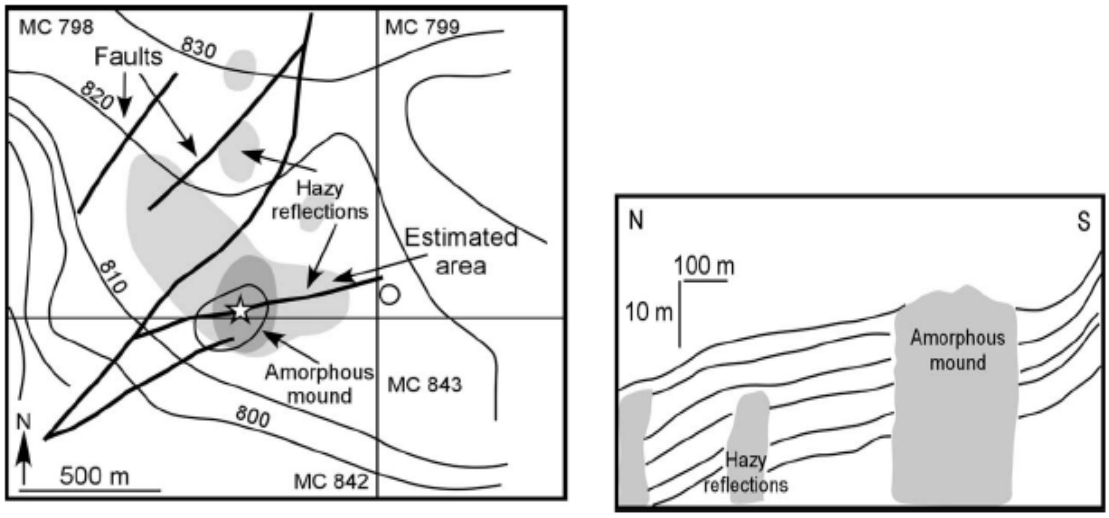

Figure 4-10 – Mississippi Canyon 798/842 map and cross section (from Milkov and Sassen, 2003).

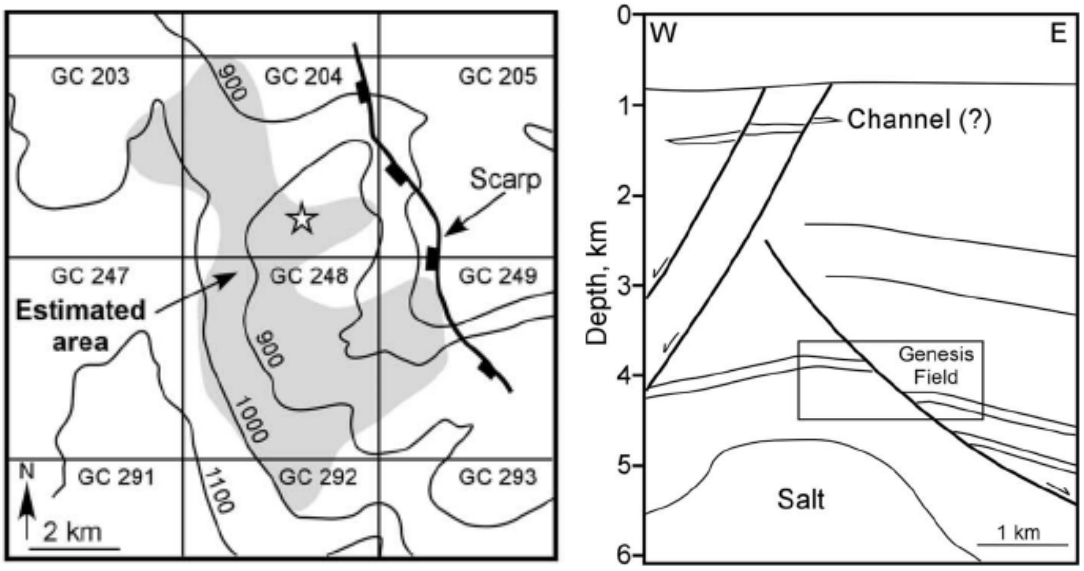

Figure 4-11 – Green Canyon 203/204 map and cross section (from Milkov and Sassen, 2003).

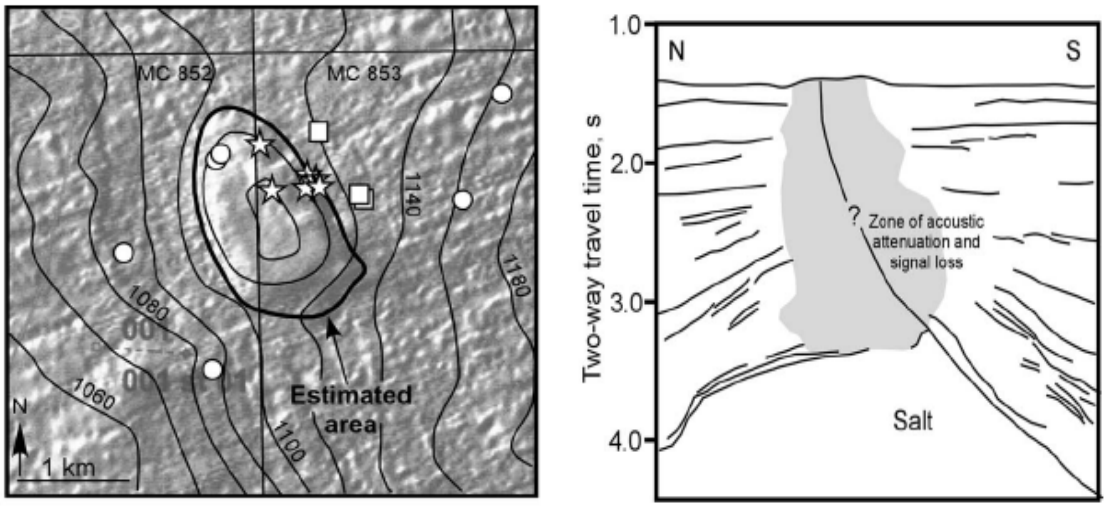

Figure 4-12 – Mississippi Canyon 852/853 map and cross section (from Milkov and Sassen, 2003).

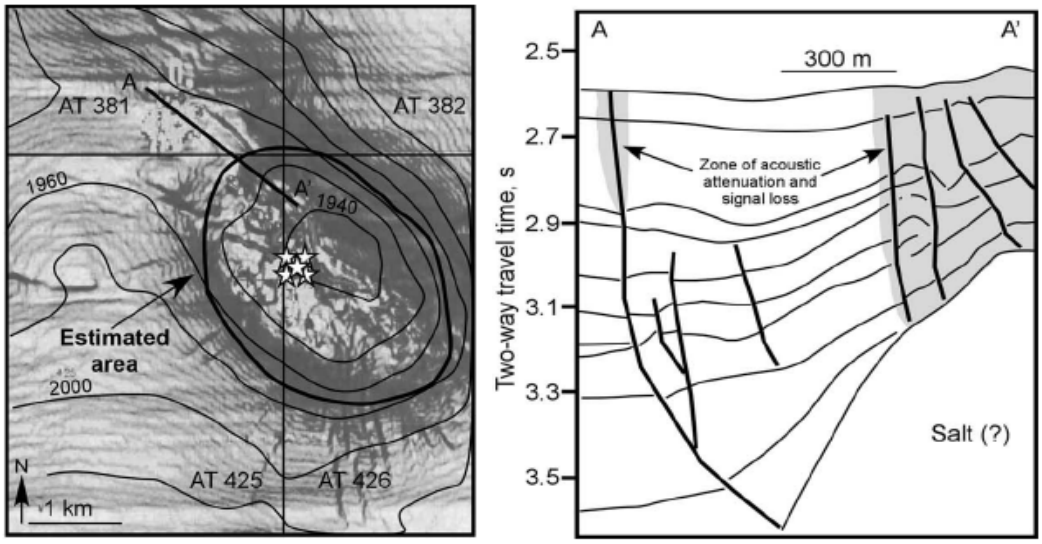

Figure 4-13 –Atwater Valley 425 map and cross section (from Milkov and Sassen, 2003).

In addition to the sites mentioned above, two sites have been drilled by US-DOE/Chevron JIP. Those two sites are Atwater Valley 13/14 and Keathley Canyon 151 (Figure 4-14). A total of seven wells were drilled during this expedition at water depths ranging from 1290 – 1320 meters.

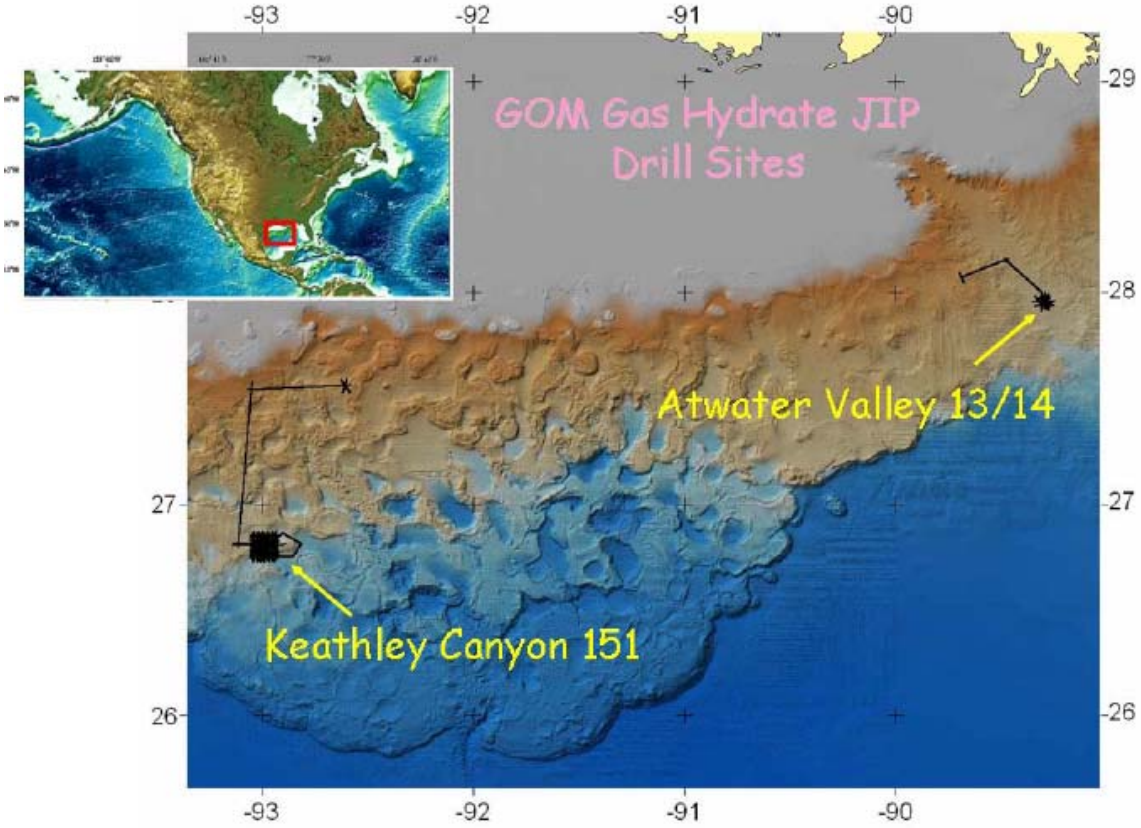

Figure 4-14 – US-DOE/Chevron JIP gas hydrate drill sites (from Conte and Bloyes, 2005).

Nankai Trough

The Nankai Trough is a convergent margin offshore southwest Japan. It is situated along the subduction zone between the Philippine Sea Plate and the island arc system of Japan. This area has been the focus of geologic and geophysical investigations for gas hydrates. Convergent margins are favorable locations for the formation of gas hydrates and it is estimated that two-thirds of total worldwide marine hydrates are found in these geological structures. According to Krason (1994), total gas resources in the form of gas hydrates in Nankai Trough is around 15 to 148 Tcf. Figure 4-15 (He et al., 2006) describes the geological setting of Nankai Trough. Gas hydrates were indicated by the detection of BSRs in the early 1980s. However, the first samples of cores containing gas hydrates were collected in 1990 during ODP Leg 131. During the Nankai Trough expedition, hydrates were noted in cores between 90 to 140 meters below the seafloor (mbsf). The methane in the cores was considered to be of biological origin because of the low concentration of higher hydrocarbons.

The ODP carried out another expedition in Nankai Trough in 2000 and drilled seven holes. Japan National Oil Company and Japan Petroleum Exploration Corporation drilled three boreholes in eastern Nankai Trough as a part of Japan's effort to study the feasibility of gas production from the marine hydrate deposits. The world's first offshore natural hydrate exploratory wells were drilled from November 1999 to February 2000 at a single location at the water depth of 945 meters. Up to about 100 mbsf the sediments are composed of flat-lying mudstone-siltstone with occasional ash beds. Below 100m, the formation is mudstone and with increasing depth, the number and thickness of sandstone beds increases.

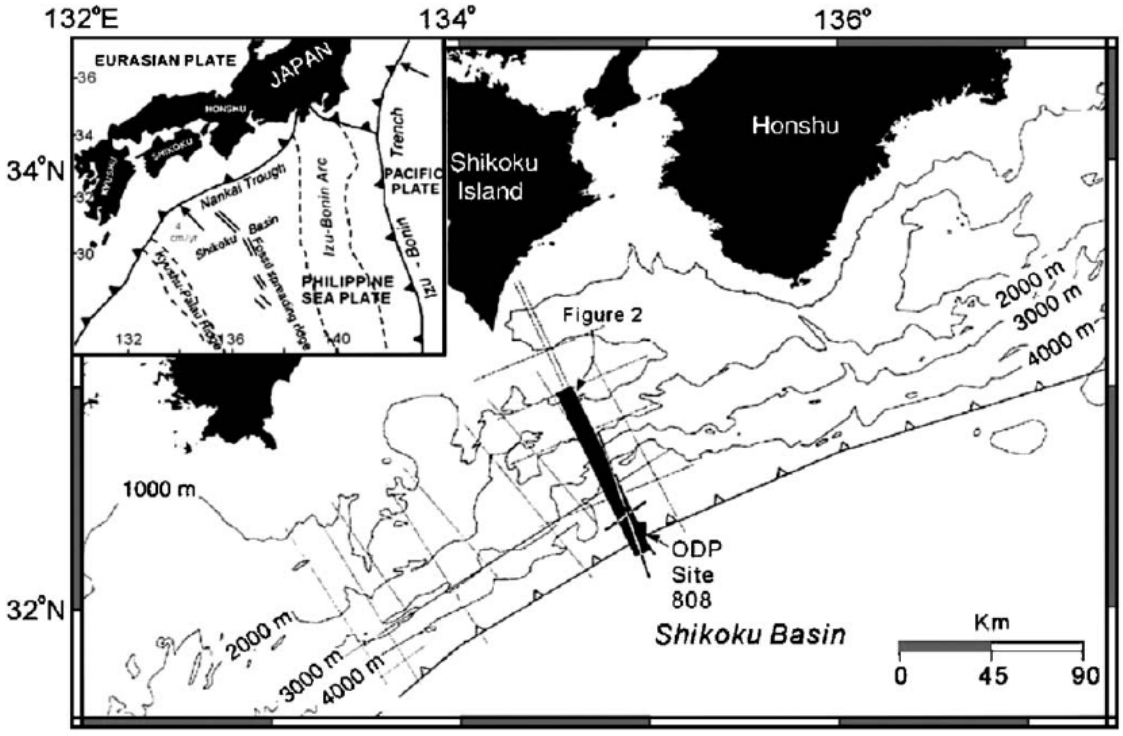

Figure 4-15 – Geological setting of Nankai accretionary prism (from He et al., 2006).

Chapter 5 – Pore Scale Modeling

Summary of Grain-Scale Modeling by UCB

The proposed model studies alteration of hydrate-bearing sediments (HBS) caused by hydrate dissociation. Simulated tests of stressing rock samples in laboratory produce estimates of the core-scale elastic moduli of the samples. Simulations employ a quasi-static variational approach, where deformation of granular matter is presented as a continuous sequence of equilibrium configurations. Our model is based on the principle of quasi-static equilibrium and uses physical material properties as input data, with no adjustments for calibration. Variational approach made possible the development of efficient numerical algorithms.

Ultimately, the objective of this effort is to develop a grain-scale model of HBS. Hydrate dissociation alters the strength of HBS. In particular, transformation of hydrate clusters into gas and liquid water weakens the skeleton and, simultaneously, reduces the effective stress by increasing pore pressure. The large-scale objective of the study is the evaluation of geomechanical stability of the offshore oil&gas production infrastructure. The output of the micro-scale model described here is intended to be used in the reservoir-scale simulations of coupled flow and geomechanics.

We model the mechanical deformation of HBS or, more generally, of a granular medium, by numerical simulations of deformation of a pack of elastic spherical grains. Although this approach cannot entirely replace laboratory tests as the ground truth, it offers insights and capabilities that may be not available otherwise. Grain-scale simulations provide unique insights into the mechanisms underlying phenomena such as strain hardening and hysteresis. Moreover, they can be used to play various what-if scenarios, which cannot be performed in a laboratory.

Milestones:

- The conceptual model developed within Phase One of the project has been verified against published laboratory test data.
- The quasi-static grain-scale model of HBS has been extended to incorporate tangential contact forces at grain-to-grain contacts.
- The computational performance has been significantly enhanced by the development and implementation of customized algorithms.

This report covers results within Subtask 3.1 and Task 6. Due to the discontinuation of DOE funding, the work on the project ceased rather prematurely, see the Further Reading section.

Technical Approach

The proposed model of rock deposition and alteration is based on the quasi-static variational approach, where deformation of granular matter is presented as a continuous sequence of equilibrium configurations. A disordered heterogeneous grain pack, constrained by solid walls, models granular medium, see Figure 5-1. Grain sizes and material properties are assigned with values from uniform and normal distributions, respectively. Each equilibrium configuration corresponds to a minimum of appropriately defined energy functional. Macroscopic elastic moduli are evaluated from the deformations and displacements of individual grains. The method relies on sound physics, and the simulation-based estimates of elastic moduli of glass-bead packs and sandstones adequately predict available published laboratory measurements with no adjustments of material properties [Holtzman et al 2008]. At the same time, simulated experiments can reproduce arbitrary reservoir conditions, including those which are impossible to realize in a laboratory test.

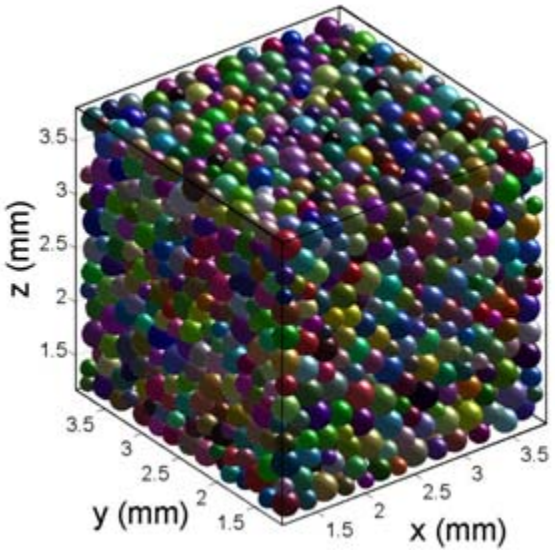

Figure 5-1. An example of computer-generated disordered 3D grain pack. The distribution of grain sizes and material properties are taken from published data.

Hydrate dissociation weakens the solid skeleton by "melting" hydrate clusters. Unless evacuated immediately, the gas released by dissociation increases the pore pressure. Since the overburden stress remains constant, the excess pore pressure reduces the effective stress. As a consequence, the shear strength of the HBS goes down. Grain-scale simulations provide insights into the interaction between these two mechanisms of formation damage and provide estimates that can be used as input in large-scale coupled flow and geomechanical simulations [Rutqvist, J. and Moridis, G. J., 2007].

Computer-generated HBS grain pack

Gas-hydrates are crystalline solids composed of water molecules arranged into a rigid framework of cages, occupied by gas molecules. Hydrates form under relatively high pressures and low temperatures, with sufficient supply of gas [Sloan, 1998, 2003]. There is a variety of models of hydrate distribution in the pore space. In the context of the pre-

sent study, the most interesting case is where the hydrates are integrated into the solid skeleton as load-bearing particles. In simulations, the hydrates are represented by the smaller grains, assigned with material properties of methane-hydrate. There is no affinity between hydrate and rock grains in the model presented here.

We model the effect of hydrate dissociation on the mechanical properties of an HBS sample using the quasi-static variational model mentioned above. In a computer-generated HBS sample, hydrates clusters are part of the load-bearing solid skeleton. A partial dissociation of hydrates results in shrinking of the hydrate phase, and a reduction of the effective stress caused by an increase of the pore pressure. Both phenomena dramatically reduce shear strength of the HBS. Moreover, simulations show that this strength reduction happens as an abrupt drop, which is followed by a more gradual further weakening of the material.

Main parameters

Using the convention that hydrates are a part of the pore volume [Jin et al., 2002], the hydrate saturation, S, is defined as $S = V_h/V_{\text{tot}}$. Here V_h denotes the volume occupied by hydrates, and V_{tot} is the total pore volume. The porosity is defined here as the water-filled porosity, see [Jin et al. 2002]. Weakening of HBS is the result of two main factors: (a) A shrinking of the solid skeleton, as some of the hydrate grains are converted into gas and liquid water; and (b) a decrease of the effective stress due to the growing pore pressure. Reduction of hydrate saturation, $S \rightarrow S-\Delta S$, $\Delta S > 0$, quantifies the dissociation. The hydrate shrinkage is modeled by scaling down the hydrate grain radii by a uniform factor. The computed reduction of the elastic moduli of the pack serves as a measure of formation damage.

The grain pack used in simulations contained 2740 grains. The radii were uniformly distributed between 0.07 and 0.09 mm. The bulk and shear elastic moduli of solid grain material were 47.6 and 43.5 GPa respectively, which correspond to material properties of quartz grains. A portion of grains of radii 0.07-0.075 mm was assigned material properties of methane-hydrate: 6.1 GPa for the bulk modulus, and 2.5 GPa for the shear modulus.

The initial porosity and hydrate saturation prior to dissociation were $\varphi \approx 36\%$ and $S \approx 0.22$. The initial effective stress was 21 MPa. The choice of the magnitude of initial stress reflects the overburden including the gas or oil recovery structures (e.g. an oil platform) standing on the ocean floor.

Determination of the relation between the pore pressure and the decrement of hydrate saturation requires account of the kinetics of hydrate dissociation: the excess pressure varies with factors such as dissociation rate, sediment permeability, and initial pore pressure [Xu & Germanovich, 2006]. We simulate several dissociation scenarios, by using a range of saturation decrements and excess pressures evaluated from the model of [Xu & Germanovich 2006] as input parameters. By varying the excess pressure and the saturation decrement independently, computations generate a series of configurations representing different scenarios.

Simulations

A range of possible dissociation scenarios was modeled by varying the excess pressure, p_{ex}, between 0–1 MPa, and the saturation decrement, ΔS, between 0–0.015. The varying elastic moduli were used as indicator of rock weakening. Thus, simulations included two components. First, deformation of the grains and rearrangement of the pack were computed at changing conditions: shrinking hydrate grains and decreasing effective stress due to growing pore pressure. Second, the elastic moduli were determined by simulation of small displacements of the solid walls bounding the grain pack, and numerical evaluation of the corresponding variations of the macroscopic stress. Flow modeling and relaxation of the excess pore pressure are a part of large-scale simulations, which are outside of the scope of our grain-scale model. Therefore, both the excess pressure and the degree of dissociation are input parameters.

Figure 5-2 shows the effective moduli versus excess pore pressure, assuming fixed shrinking of the hydrate grains that corresponds to the saturation decrease of one percent. Figure 5-3 shows a plot of computed decrease of the moduli versus saturation decrement assuming a fixed excess pore pressure, p_{ex}, of 1.0 MPa. Both these figures show an almost instantaneous drop in the shear modulus caused by excess pore pressure. Practically, this result implies that unless the released gas has a highly-permeable evacuation path from the dissociation area, the instability of the see floor can be a serious hazard and lead to the most dramatic undesired consequences.

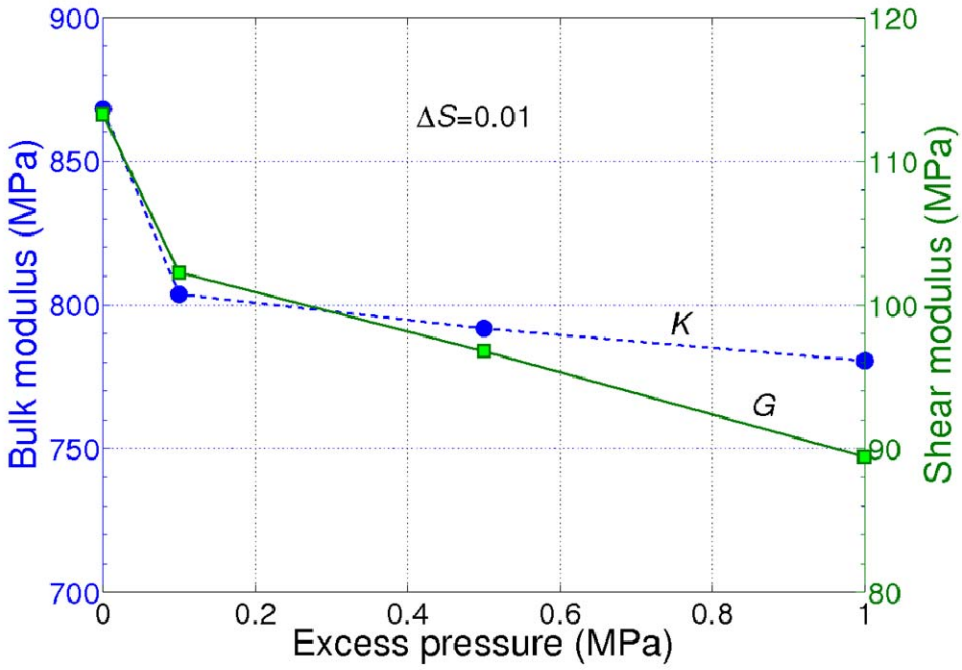

Figure 5-2. Simulations showing weakening of a hydrate-bearing sediment caused by hydrate dissociation. Weakening is demonstrated by a reduction in bulk (dashed line) and shear (solid line) modulus vs. increasing the excess pore pressure, p_{ex}, for a fixed saturation decrement, ΔS = 0.01.

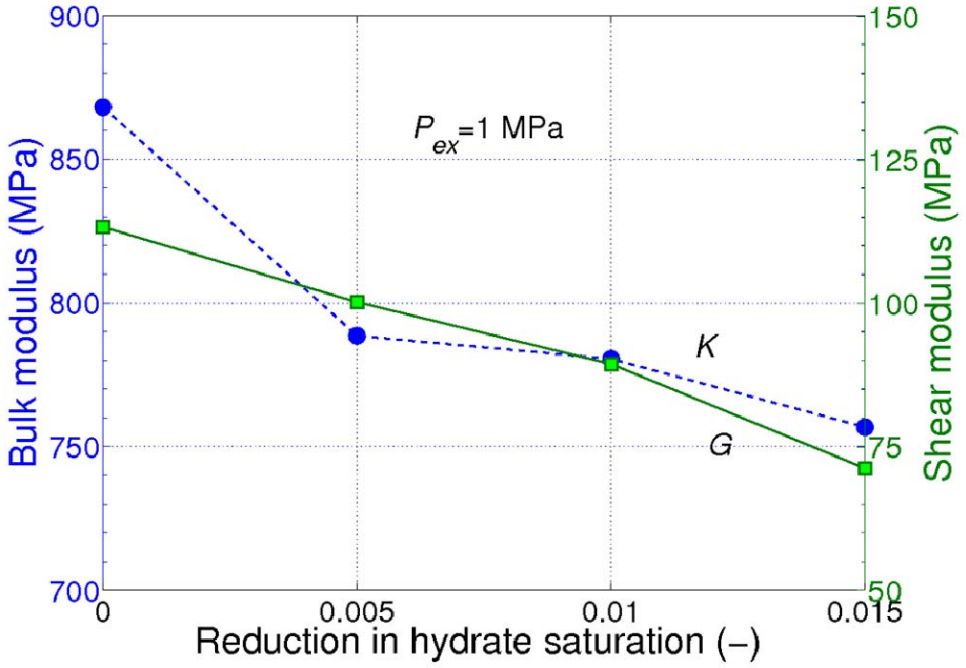

Figure 5-3. Reduction in bulk and shear moduli plotted as dashed and solid lines, respectively, vs decreasing the saturation for a fixed excess pressure, p_{ex} = 1 MPa. Note instantaneous shear modulus drop due to the effective stress reduction.

Concluding Remarks

We have modeled the mechanical deformation of HBS or, more generally, of a granular medium, by numerical simulations of a pack of elastic spherical grains. This approach offers opportunities which are unavailable in laboratory experiments or in a field test. Grain-scale simulations provide unique insights into the processes and phenomena underlying the classical continuum-medium models. They explain such phenomena as strain hardening and irreversibility. Simulations can address the various what-if scenarios at reservoir conditions, which cannot be performed otherwise. The quasi-static variational model discussed above has a significant potential for study of sediment failure caused by hydrate dissociation.

Hydrate dissociation is modeled as the shrinking of a part of the solid skeleton that is the hydrate "grains". A decrease of the effective stress is related to the evolution of trapped gas. Simulations show that excess pore pressure causes an almost instantaneous dramatic weakening of shear strength of the formation. Although these simulations treat the magnitude of the growing pore pressure as an input parameter, they show that if the gas formed by the dissociation is trapped, the loss of the ocean floor stability can be dramatic.

Ultimately, stability of the slope at the ocean floor can be predicted by the coupled large-scale simulations that account for both fluid flow and geomechanics. Such simulations require input in the form of trend curves, which are determined by the micromechanics of

the medium. A micromechanical model capable of providing such input has been developed here.

Further Reading

Some results have been published in Holtzman et al. [2008] and SPE Paper 114223. Also, see *Micromechanics of sediments: a variational approach to grain-scale simulations*, PhD Thesis by Ran Holtzman, University of California, Berkeley, 2008

Journal publications:

1. Holtzman, R., Silin, D. B., Patzek, T. W., Mechanical properties of granular materials: a variational approach to grain-scale simulations. Journal for Numerical and Analytical Methods in Geomechanics, 2008. Available on line: http://dx.doi.org/10.1002/nag.725
2. Holtzman, R., Silin, D. B., Patzek, T. W., Frictional Granular Mechanics: A Variational Approach. International Journal for Numerical Methods in Engineering. Submitted.

Conference papers

1. Holtzman, R., Silin, D.B., Patzek, T.W., Mechanical Properties of Granular Materials: A Variational Approach to Grain-Scale Simulations. 8th. World Congress on Computational Mechanics & 5th. European Congress on Computational Methods in Applied Sciences and Engineering, Venice, Italy, 2008.
2. Holtzman, R., Silin, D.B., Patzek, T.W., Frictional Granular Mechanics: A Variational Approach to Grain-Scale Simulations. CMG 2008 - 27th IUGG Conference on Mathematical Geophysics, Longyearbyen, Norway, 2008
3. Holtzman, R., Silin, D.B., Patzek, T.W., Micromechanics of Hydrate Dissociation in Marine Sediments by Grain-Scale Simulations. Paper SPE 114223 presented at SPE Western Regional and Pacific Section AAPG Joint Meeting, 29 March-2 April 2008, Bakersfield, California, USA.
4. Holtzman, R., Silin, D.B., Patzek, T.W. (2007) Micromechanics of Hydrate-Bearing Sediments by Grain-Scale Simulations. Eos Trans. AGU, 88(52), Fall Meet. Suppl., Abstract OS22A-07.
5. Holtzman, R. , T. W. Patzek, and D. B. Silin (2007) Deformations of Sediments via Grain-Scale Simulations: A Quasi Static Approach. Eos Trans. AGU, 88(52), Fall Meet. Suppl., Abstract T43E-04
6. Holtzman, R., Silin, D.B., Patzek, T.W.,Mechanical properties of granular media via grain-scale simulations. 9th US National Congress in Computational Mechanics, San-Francicso, CA, 2007.
7. Holtzman, R., Silin, D.B., Patzek, T.W., Estimating Macroscopic Mechanical Properties Via Grain-Scale Simulations. 2007 AAPG Annual Convention and Exhibition (April 1 - 4, 2007) Long Beach, CA
8. Holtzman, R., Silin, D. B., and Patzek, T.W. (2006), The Strength of Hydrate-Bearing Sediments: A Grain-Scale Approach, Eos Trans. AGU, 87(52), Fall Meet. Suppl., Abstract MR51A-0960.

Awards

1. Ran Holtzman, Outstanding Student Paper Award from the American Geophysical Union for presentation at the 2007 Fall Meeting in San Francisco, CA.

2. Ran Holtzman, Outstanding Student Paper Award from the American Geophysical Union for presentation at the 2006 Fall Meeting in San Francisco, CA.

Invited presentations (all presentations haves been given by Ran Holtzman)

1. 06/2008 Invited seminar, Physics of Geological Processes, Oslo University, Oslo, Norway.
2. 04/2008 Invited seminar, Department of Geophysics, Stanford University, Stanford, CA.
3. 06/2007 Invited seminar, Department of Environmental Sciences and Energy Research, Weizmann Institute of Science, Israel.
4. 06/2007 Invited seminar, Department of Geological & Environmental Sciences, Ben Gurion University, Israel.
5. 06/2007 Invited seminar, Geophysics Department, Lawrence Berkeley National Laboratory, Berkeley, CA.

Bibliography.

1. Rutqvist, J. and Moridis, G. J. (2007). Numerical studies of geomechanical stability of hydrate-bearing sediments. In 2007 Offshore Technology Conference, 30 April - 3 May 2007, Houston, TX.
2. Jin, G. (2006). Physics-Based Modeling of Sedimentary Rock Formation and Prediction of Transport Properties. PhD thesis, University of California, Berkeley, Berkeley, CA.
3. Sloan, E. D. (1998). Clathrate Hydrates of Natural Gases. New York: Marcel Dekker.
4. Sloan, E. D. (2003). Fundamental principles and applications of natural gas hydrates. Nature, 426, 353–363.
5. Jin, Y. K., Lee, M. W., and Collett, T. S. (2002). Relationship of gas hydrate concentration to porosity and reflection amplitude in a research well, Mackenzie Delta, Canada. Marine and Petroleum Geology, 19(4), 407–415.
6. Xu, W. & Germanovich, L. N. (2006). Excess pore pressure resulting from methane hydrate dissociation in marine sediments: A theoretical approach. Journal of Geophysical Research, 111, B01104.

Chapter 6 – PETREL-FLAC3D Data Exchange, Description and Workflow

Problem Statement

Given a *PETREL* database, provide software tools and describe a workflow for the creation of a *FLAC3D* model ready-to-run.

The PETREL model contains, among other things, the description of horizons and the special distribution of properties. As part of this project, an automatic method of creating a *FLAC3D* grid must be developed. The resulting grid must be composed of multiple materials representing the various regions of the *PETREL* database delimited by the horizons.

In addition to the grid, an automatic and conservative method of extracting material properties from *PETREL* should also be devised. The extracted properties should be automatically assigned to the individual *FLAC3D* grid element. The user will complement the missing material properties and mechanical behavior law parameters by adding them manually to the *FLAC3D* data file.

A number of comments are in order

1. Data sets extracted from *PETREL* may be very large. A automatic method should be devised to coarsen (decimate) the data, while maintaining pertinent details.
2. The *PETREL* model may contain features ranging in size from tens of meters to hundreds of kilometers. This requires a non-traditional meshing approach that would keep the total element count in the *FLAC3D* model to a minimum while ensuring adequate representation of details and adequate transition between *FLAC3D* element sizes.
3. Property transfer from *PETREL* to *FLAC3D* should be conservative
4. The workflow should be simple and robust

FLAC3D and the *3DShop* option

FLAC3D is a numerical modeling software for the advanced geotechnical analysis of soil, rock, and structural support in three dimensions. FLAC3D is used in analysis, testing, and design by geotechnical, civil, and mining engineers. It is designed to accommodate any kind of geotechnical engineering project where continuum analysis is necessary. FLAC3D uses an explicit finite volume formulation that models complex behaviors not readily suited to finite element software, such as problems consisting of several stages, large displacements and strains, non-linear material behavior and unstable systems (yield/failure over large areas, or total collapse, etc.).

FLAC3D version 3.1, combines speed (using multithreading on multiple processors, see multiprocessor speedup in Figure 6-4), virtually unlimited model size (with the new 64 bit implementation), and geometrical flexibility (with its ability to create both hexahedral and tetrahedral grids using the 3DShop option)

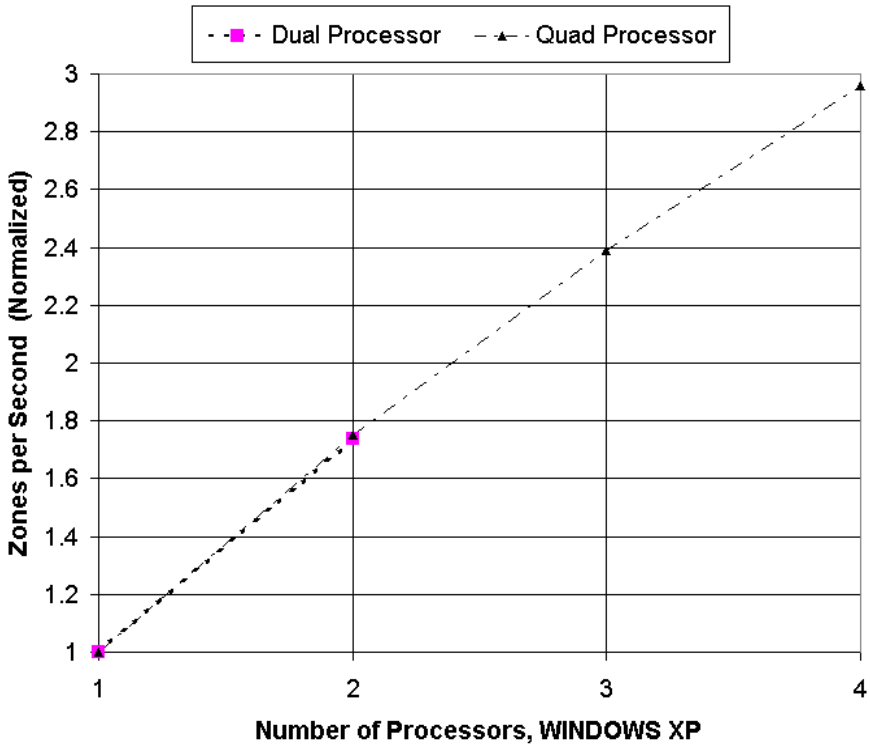

Figure 6-4: FLAC3D 3.1 Parallel performance: multiprocessor speedup as a function of number of processors

In addition to hexahedral grids, FALC3D 3.1 accepts more complex models using tetrahedral grids supported with the Nodal Mixed Discretization (NMD) scheme which ensures accurate plasticity results for tetrahedral grids. 3DShop's local mesh refinement facility allows for a more economical use of memory by concentrating elements near areas of interest.

The 3DShop option of FLAC3D is a powerful solid modeler that can be used to import complex models or create them from scratch. 3DShop includes an automatic hexahedral and tetrahedral grid generator for FLAC3D (Figure 6-6).

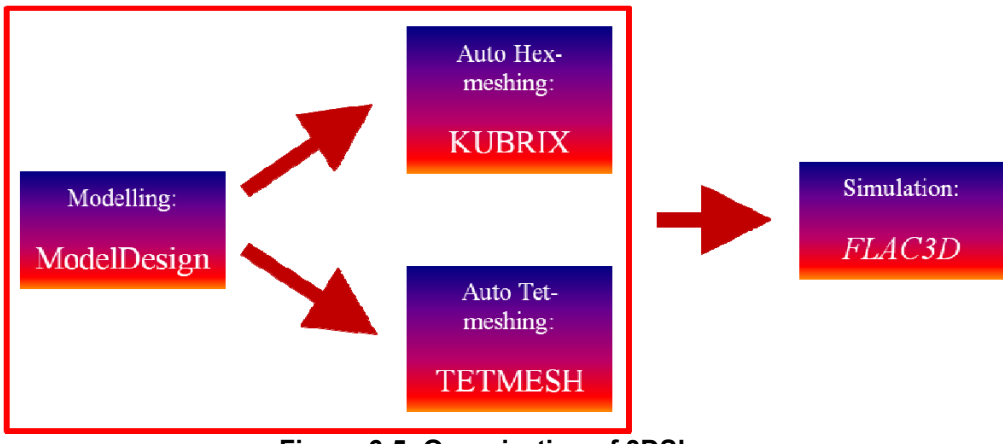

Figure 6-5: Organization of 3DShop

In contrast to many solid modelers used in mechanical engineering, 3DShop can handle complex non-manifold surfaces commonplace in geotechnical engineering applications. CAD and GIS data can be read from a variety of geotechnical analysis and mechanical computer-aided engineering tools such as GoCad, Vulcan, Map3D, DataMine, AutoCad, SolidWorks, SolidEdge, ProEngineer and Catia through the STEP, IGES, 3DS (3DStudio), STL, VRML, DXF and DWG (AutoCad) file format to produce both hexahedral and tetrahedral grids (Figure 6-6).

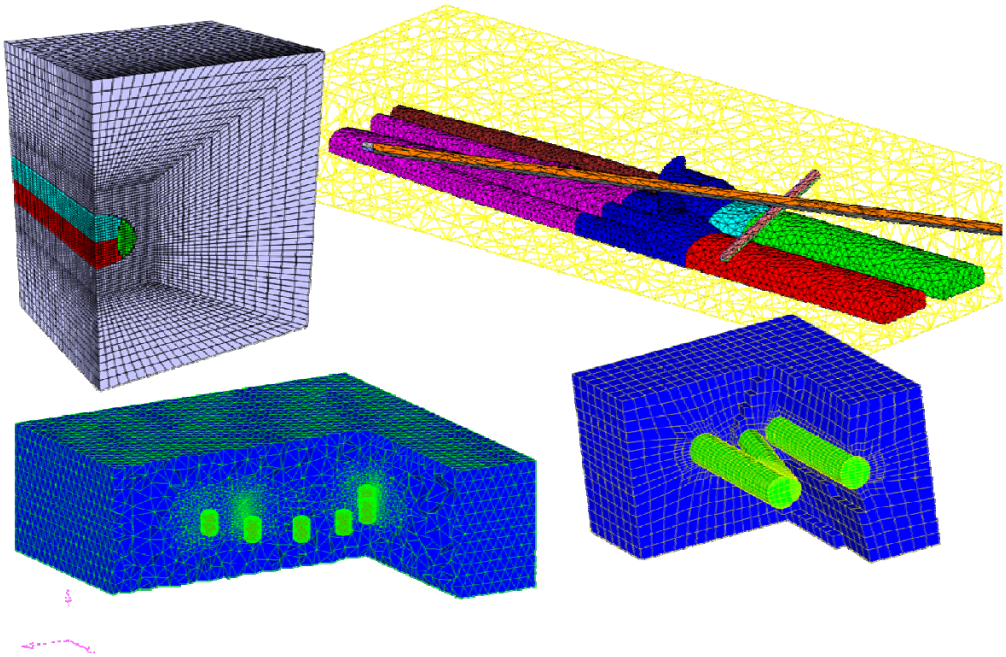

Figure 6-6: Geometrical flexibility in FLAC3D 3.1 with hexahedral and tetrahedral grids

Importing Horizons into 3DShop

As part of the present project, a module was developed to read and parse zmap files. This functionality enables users to export horizons from PETREL as zmap files and read them into 3DShop. In future developments the more straightforward import of horizons as .grid files may be envisaged.

Imported horizons can be visualized in 3DShop and saved as a single STL file. An STL file is an ASCII file used to store triangular element information. If the horizons cover a wide area and as a result their triangle count is large, 3DShop allows for the automatic coarsening or decimation of these meshes.

Data decimation

The decimation procedure substantially reduces the number of triangles in an imported horizon file while maintaining small details. The decimation process starts with the selection of a threshold dihedral angle by the user (usually in the order of 5°) and proceeds as follows:

- Sorting of all edges where the edge is the smaller of the two other edges in each of the adjacent triangles

- Sorting of the previous list in the order of increasing dihedral angles
- Collapse of all edges and their corresponding adjacent triangles, up to the threshold dihedral angles specified by the user
- This procedure is iterated several times until no edge collapse is possible

An example of the outcome of this procedure for a given horizon is shown in Figure 6-7. It can be noted that this decimation approach preserves details while reducing the triangle count by nearly an order of magnitude.

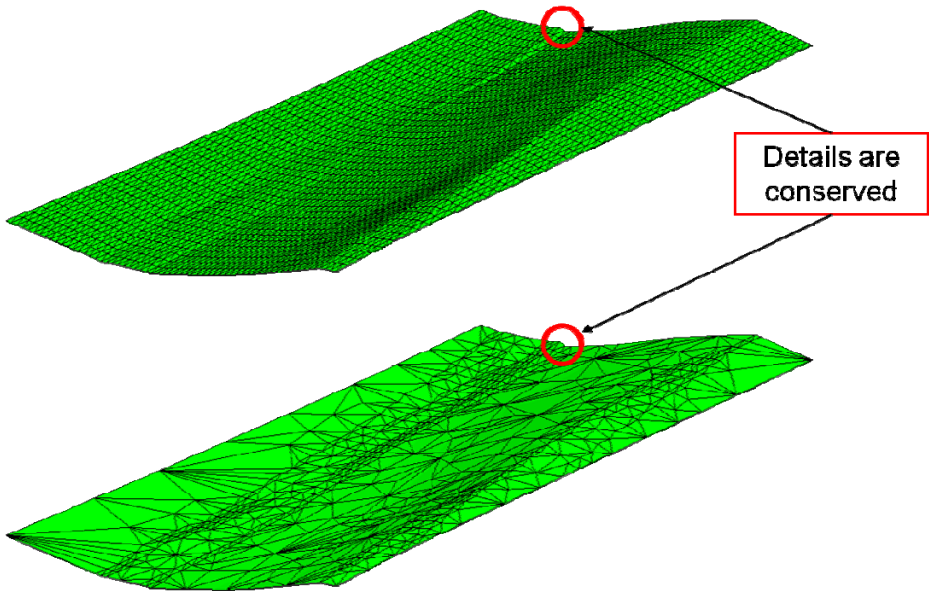

Figure 6-7: zmap file translation and subsequent mesh decimation

After reading all the horizons, the assembled geometry can be visualized in 3DShop (Figure 6-8).

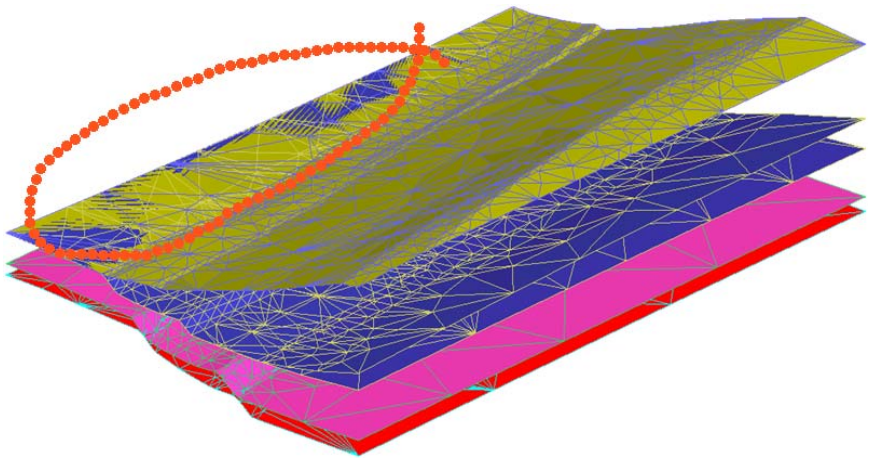

Figure 6-8: Final assembled horizons. Highlighted are show two or more tangent horizons.

A closer look at Figure 6-8 shows that the geometry of the assembled horizon presents a major challenge. The highlighted area shows that two or more horizons are tangent. This represents a challenge for traditional solid modeling where surfaces should intersect at clear edges without causing topological ambiguity or any angle close to zero. If we were

to clean up this geometry, we would have to decide where the intersection of the horizons occurs, and assume a clean description of the intersection curve. This would require manual intervention. The Oct-tree meshing approach avoids this problem.

Oct-tree Mesh Generation

Mesh generation should not require any operator intervention. This leaves us with any of the available automatic meshing options. But automatic meshing requires the creation of a so-called solid model. This requirement can also be described as that of creating a watertight triangulation of all the surfaces constituting the horizons and the outer block. Because of the topological ambiguity due to tangent horizons, we propose an oct-tree mesh generation technique.

Oct-tree meshing follows these steps:

1. Determination of a bounding cube. This cube is called the root element
2. If this element intersects the horizon, subdivide it into 8 cubes
3. If the edge length of the cube is smaller than a user-specified value, STOP
4. Else, go to step 2.

Because of its simple structure, the oct-tree mesh has a simple data structure depicted in Figure 6-9.

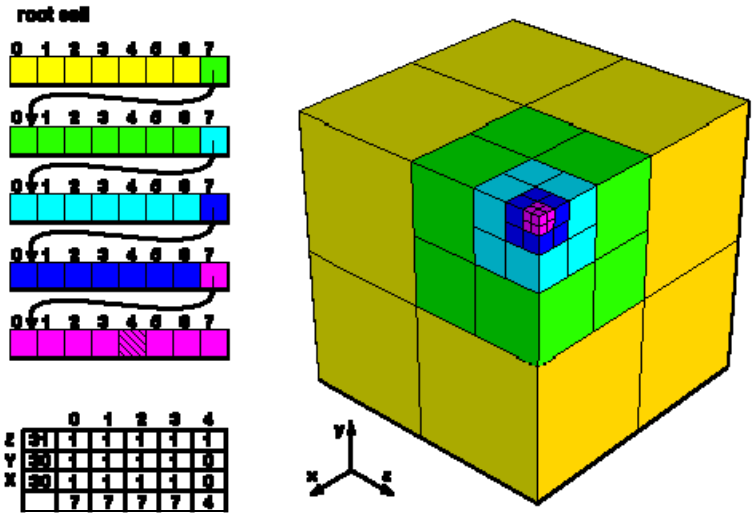

Figure 6-9: Data structure of an Oct-tree mesh

With an Oct-tree mesh, the size of the smallest captured detail is about the size of the smallest cube of the oct-tree; in the example above, the size of the pink cube.
The Oct-tree is first used to detect the geometry. Figure 6-10 shows a 2-D illustration of this approach. The blue region is the oct-tree's interpretation of the geometry.

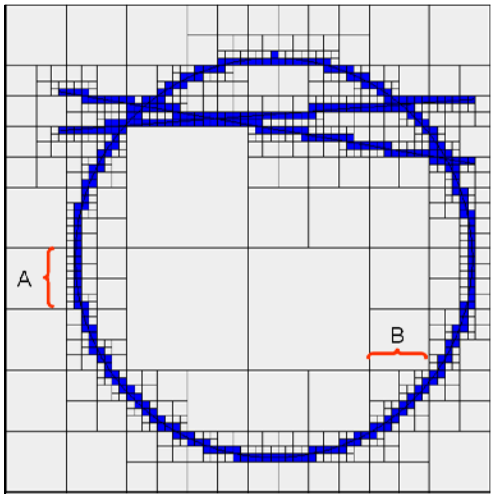

Figure 6-10: Principle of Oct-tree geometry detection

The standard oct-tree can cause abrupt grid refinements. The A region of Figure 6-10 show an abrupt 1 to 8 refinement and region B show an asymmetrical 1 to 3 refinement. These types of mesh refinement, while supported in FLAC3D, introduce large errors and are not recommended A balanced Oct-tree is one in which all refinements are 1 to 2 in 2D and 1 to 8 in 3D (
Figure 6-11). These types of refinement are preferable.

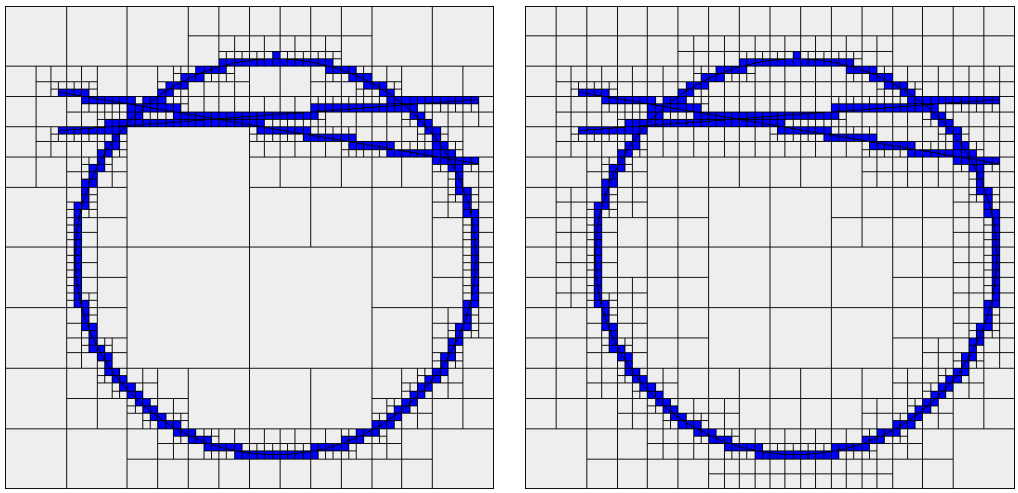

Figure 6-11: Original (unbalanced) and balanced Oct-tree. In a balanced oct-tree, two adjacent cubes are always no more than one generation apart.

The dark blue region delineates the various regions. The next step is to identify the regions as shown in Figure 6-12.

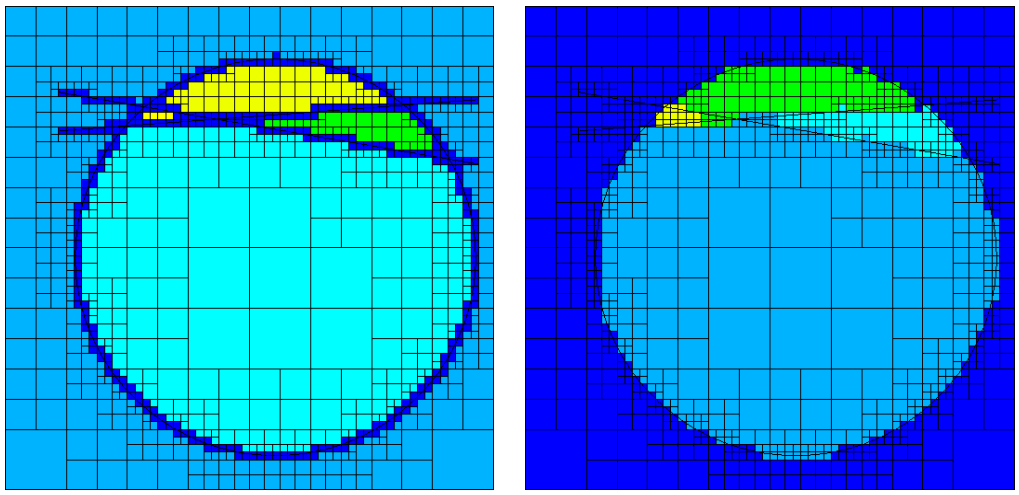

Figure 6-12: Partition of the space using an oct-tree. Left: regions + boundary. Right: regions

The oct-tree approach is very economical in terms of element count.
Figure 6-13 shows the increase in number of elements as cubes are cut into smaller and smaller pieces. In the limit, the number of elements is multiplied by 4 every time cube splitting advances one generation.

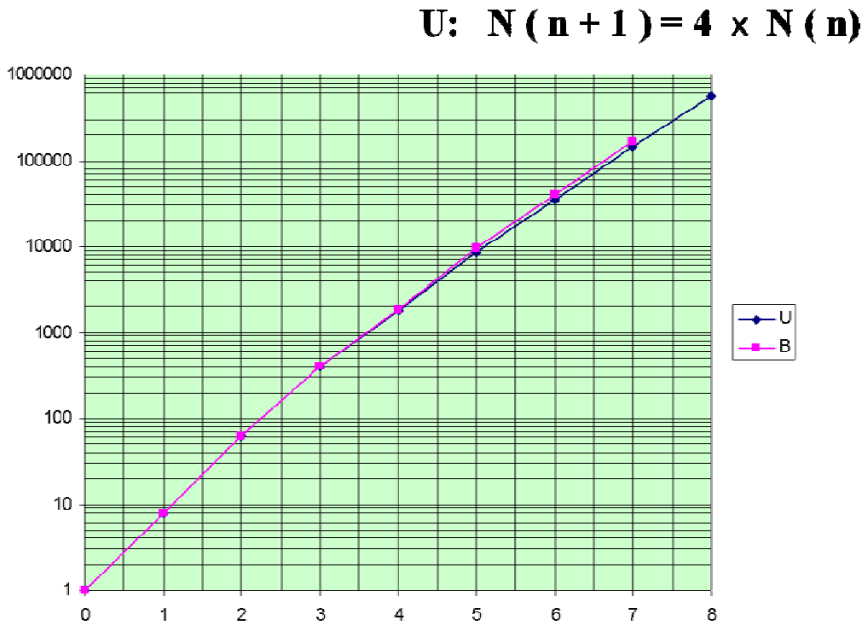

Figure 6-13: Number of elements as a function of oct-tree generations. U represents an unbalanced oct-tree while B is a balanced one which results in a slightly larger number of elements

In the present test case, the model's geometrical features vary in size from 30 to 3000 m. As a result, the number of oct-tree generations will be in the order of:

$$N = \log (3000/30) / \log 2 = 6$$

FLAC3D is one of the only commercial software packages that can handle oct-tree meshes because it can handle so –called dangling nodes. FLAC3D requires some over-head to handle such grids but all in all, using oct-tree grids results in substantial savings in memory and CPU time requirements. Figure 6-14 shows the present model meshed with a 7 level Oct-tree mesh.
Figure 6-15 shows a complex salt dome structure meshed with the same technique.

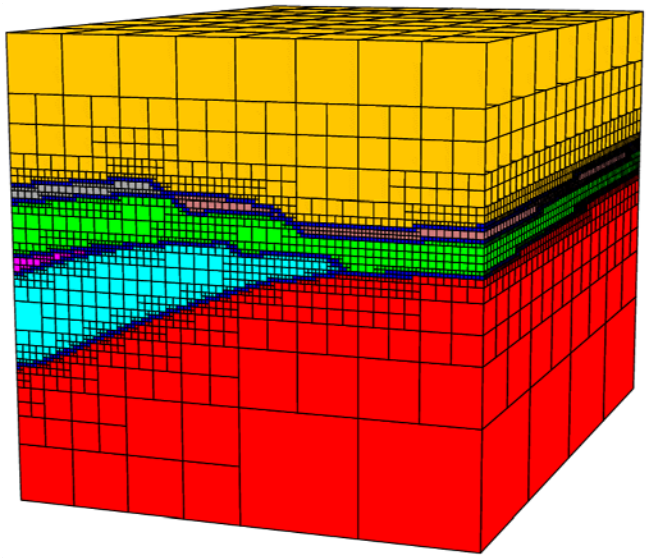

Figure 6-14: The present model meshed by a 7 level oct-tree

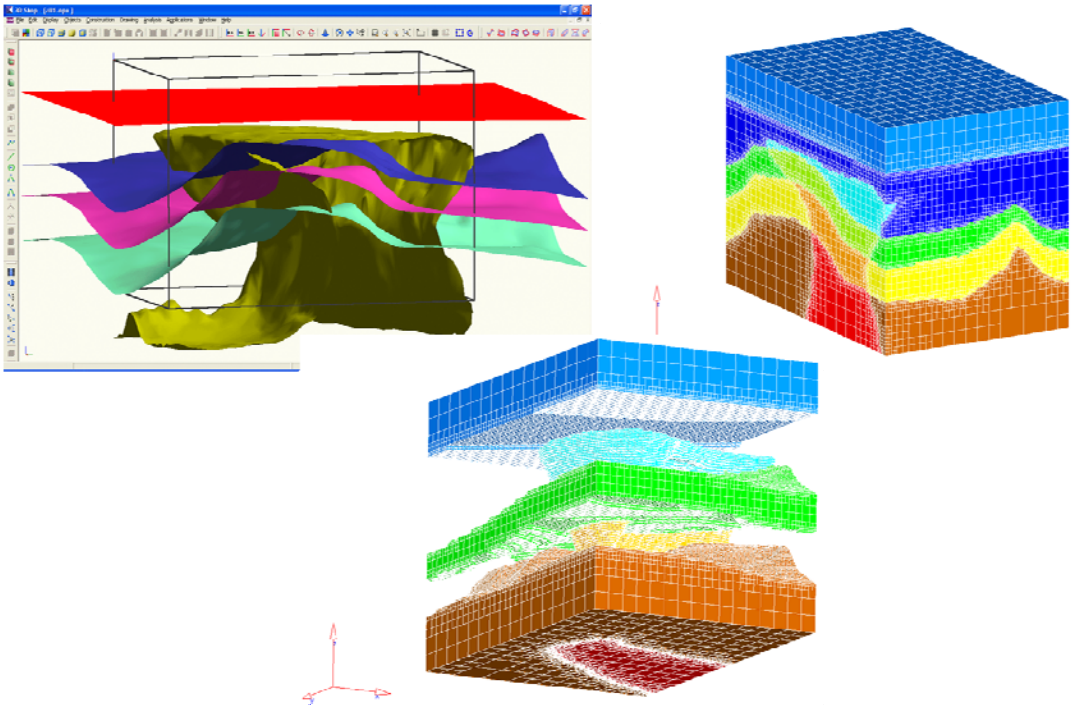

Figure 6-15: Example of a salt dome meshed with oct-trees

To verify that the oct-tree mesh results do not introduce any spurious artifacts in the results, we modeled the complete geometry as a single homogeneous elastic material, and computed the stresses caused under its own weight.

A vertical cross-section trough the middle of the geometry is shown in Figure 6-16. It can be seen that artifacts caused by the oct-tree mesh do not exceed the local maximum element size.

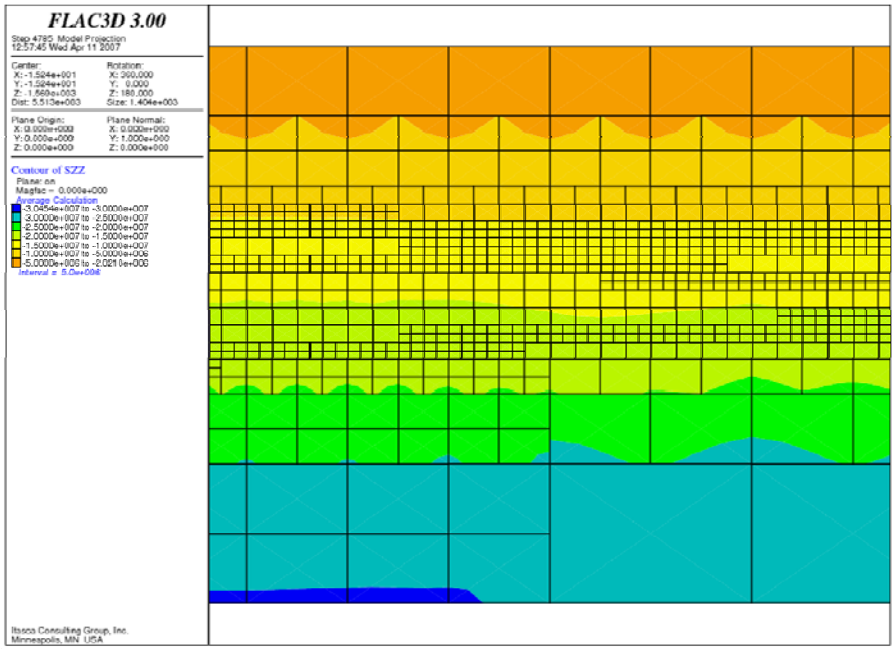

Figure 6-16: Contour of vertical stress SZZ for the present model represented as homogeneous elastic material.

PETREL Grid Extraction

In practice, material properties are extracted from a .grid file outputted by the PETREL database. The following guidelines should be creating when creating a .grid file:

1. Make sure that the grid file contains only the properties that you intend to read
2. The dimensions and location of the parallelepiped containing the model (for which the .grid file is produced) should match those of the parallelepiped containing the horizons
3. Grid orientation must be direct with the Z-direction pointing upwards

The grid file is read by 3DShop during mesh generation. If a material is available in the grid file, it will be read by 3DShop.

PETREL Property Extraction

A key concern in extracting material properties is that the property assignment be conservative. To comply with this requirement, we have implemented a method in 3DShop that computes, for each FLAC3D element, its volume intersection with all the PETREL cells concerned. For each PETREL cell P_i intersecting the FLAC3D element φ, its contribu-

tion to the FLAC3D element φ is weighed by the volume of intersection. The sum of all contributions is the FLAC3D element property (Figure 6-17).

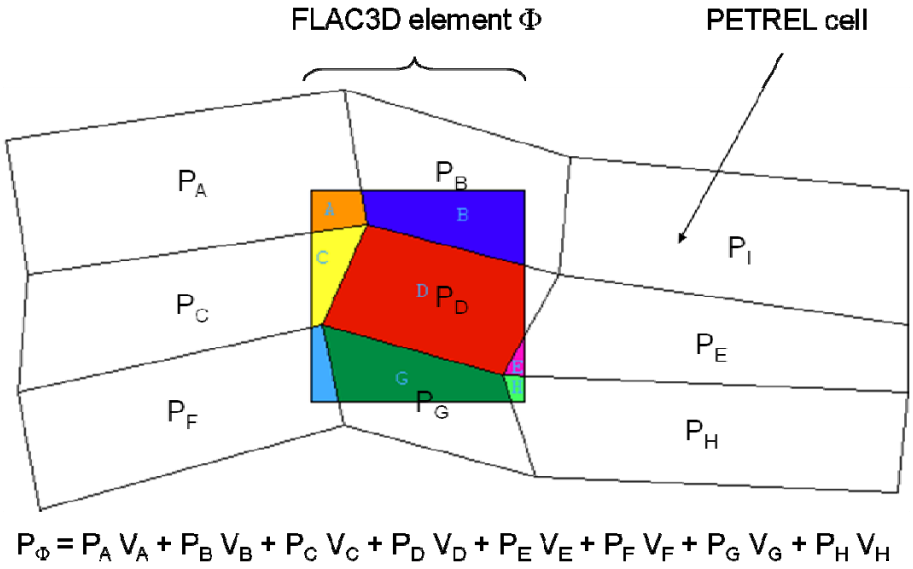

Figure 6-17: Computation of the FLAC3D element property based on PETREL cell properties

As properties are calculated for each FLAC3D element, 3DShop adds the property of that element to an ASCII file. Once mesh generation is complete and FLAC3D is launched, FLAC3D uses a FISH function to read the property file and assign the right property to each element.

Sample Calculation

An elastic model is used and several typical material properties are assigned to the various layers between the horizons. The FLAC3D data file is shown below.

```
;Schlumberger ECLIPSE-FLAC3D Data Transfer test case created by Reza Taghavi 3/27/07

res a1_lev7.sav

model elastic

group sandstone1 range group group4
group sandstone2 range group group5
group sandstone3 range group group3
group mudstone1  range group group9
group mudstone2  range group group6

;All groups other than sandstone 1, 2 & 3 and mudstone 1 & 2 are joints prop bulk 4.17E+08 shear 4.55E+08
density 2710
;coh 0 fric 3.00E+01 tension 0

prop bulk 8.03E+09 shear 6.53E+09 density 2310 range group sandstone1 ;coh 1.50E+07 fric 4.10E+01 tension
1.50E+06 range group sandstone1

;group 5 sandstone 2
prop bulk 1.33E+10 shear 1.00E+10 density 2310 range group sandstone2
;coh 2.00E+07 fric 4.90E+01 tension 2.00E+06 range group sandstone2

;group 6 sandstone 3
prop bulk 1.17E+10 shear 8.42E+09 density 2420 range group sandstone3
;coh 2.30E+07 fric 4.30E+01 tension 2.30E+06 range group sandstone3

;group 14 mudstone 1
prop bulk 3.22E+10 shear 6.48E+08 density 2710 range group mudstone1
;coh 1.20E+07 fric 4.70E+01 tension 1.20E+06 range group mudstone1

;group 17 mudstone 2
prop bulk 6.62E+09 shear 6.98E+09 density 2710 range group mudstone2
;coh 1.90E+07 fric 3.00E+01 tension 1.90E+06 range group mudstone2

set gravity 0 0 -9.81

;Apply Uniform Boundary Stress Field Values
fix x range x -2 2
fix x range x  1767  1771
fix y range y -2 2
fix y range y  1248 1252
fix x y z  range z -2203 -2197

;1000 kg/m3 * 1333 meters * 9.81 = 13.07e6 = pressure
apply nstress -13.07e6 range x 2 1767 y 2 1248 z -1500 -900
hist unbal
plot show base

save a1_lev7_Elastic_preSolve.sav
solve
save a1_lev7_Final.sav
ret

define TranslateAndScaleToMeters
   gp = gp_head
   loop while gp#null
      gp_xpos(gp) = 0.3048 * ( gp_xpos(gp) - 1643300 )
      gp_ypos(gp) = 0.3048 * ( gp_ypos(gp) - 9730950 )
      gp_zpos(gp) = 0.3048 *   gp_zpos(gp)
      gp = gp_next(gp)
   end_loop
end

impgrid a1_lev7.flac3d
TranslateAndScaleToMeters
del range group group2
attach face tol 1.
save a1_lev7.sav
```

Figure 6-18 shows the generic group assignments as produced by 3DShop. The arrowed numbers in
Figure 6-19 refer to the new group definitions in the FLAC3D data file.
Figure 6-20 Shows the FLAC3D grid after removal of the group corresponding to the material "water". This is done in the FLAC3D data file. Please note that it this test case, properties are not read from PETREL but assigned explicitly in the FLAC3D data file.

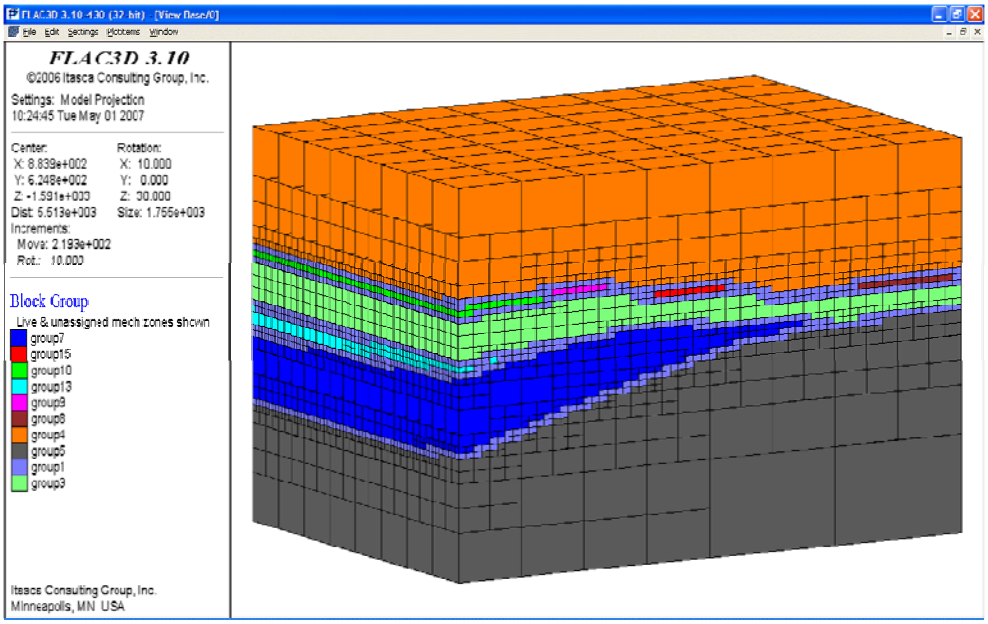

Figure 6-18: Sample calculation grid

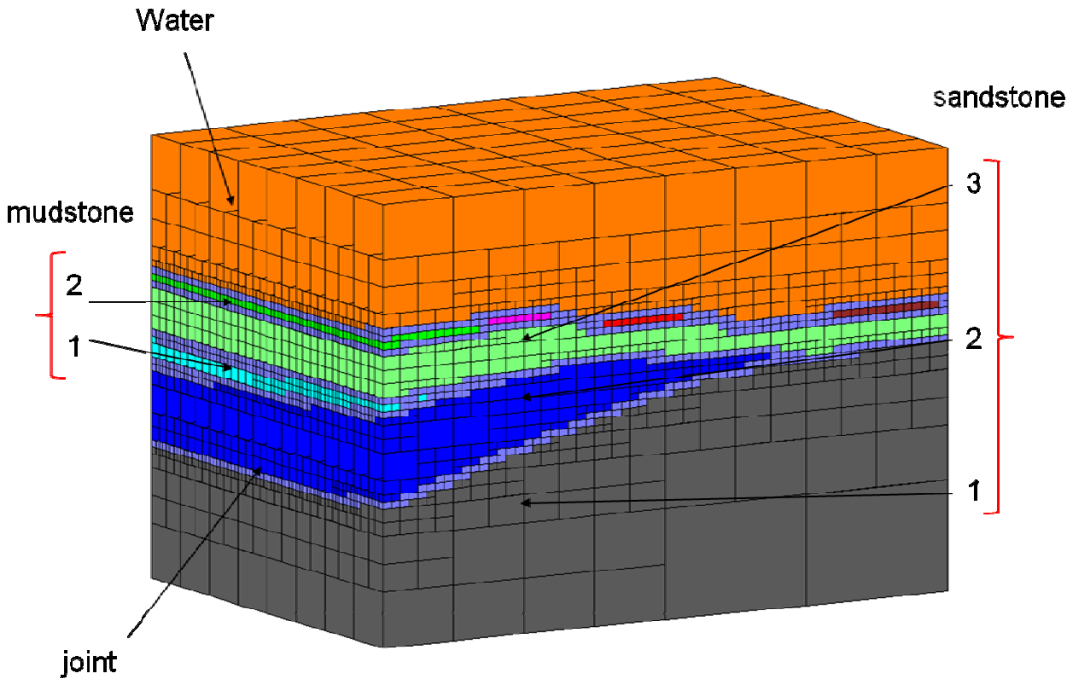

Figure 6-19: New group assignments done in the FLAC3D data file

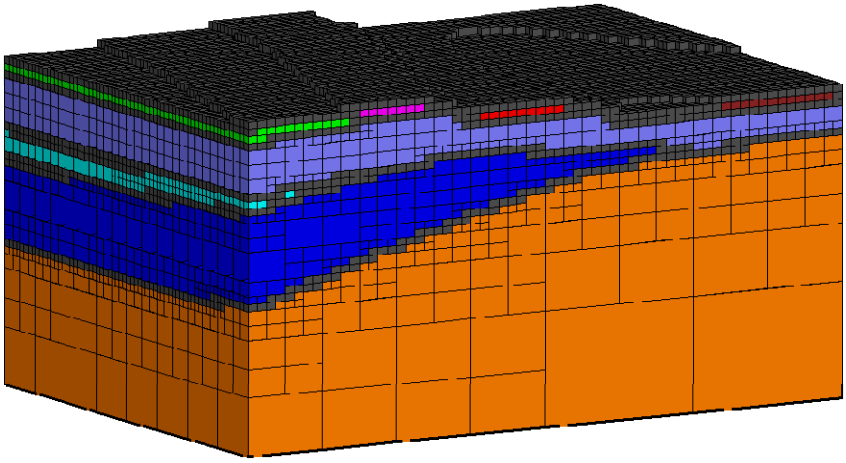

Figure 6-20: The final FLAC3D grid after removal of "water"

Figure 6-21 shows a result of this simulation

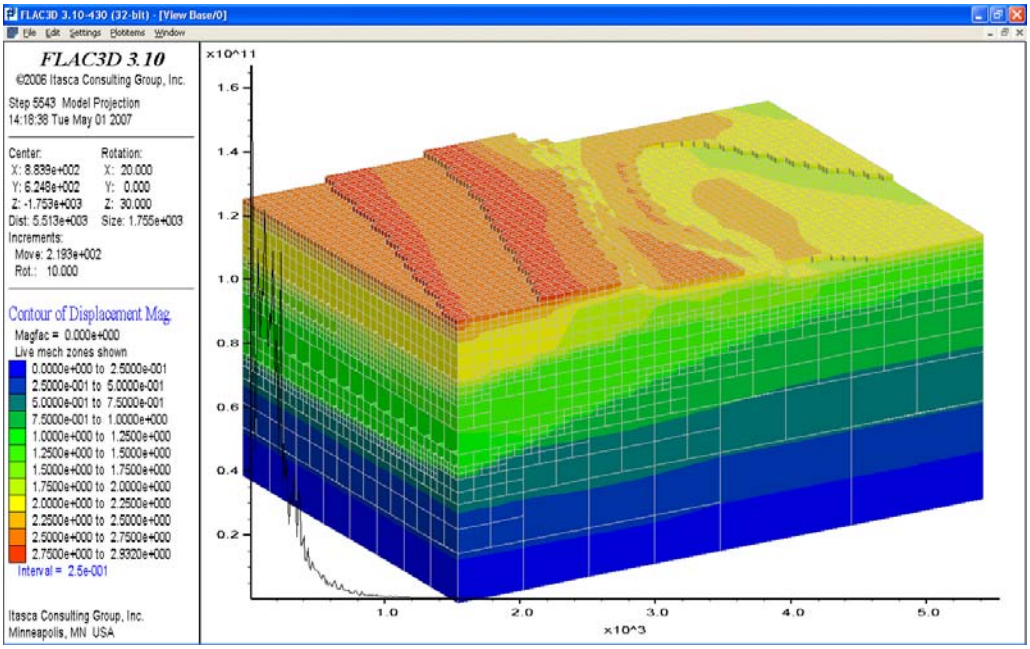

Figure 6-21: Sample elastic calculation: contour of displacement magnitude

PETREL to FLAC3D Workflow

Figure 6-22 shows a flow chart of the workflow. Yellow rectangles represent the development work performed in the framework of the present project. Light-blue squares are files and orange squares represent existing software applications.

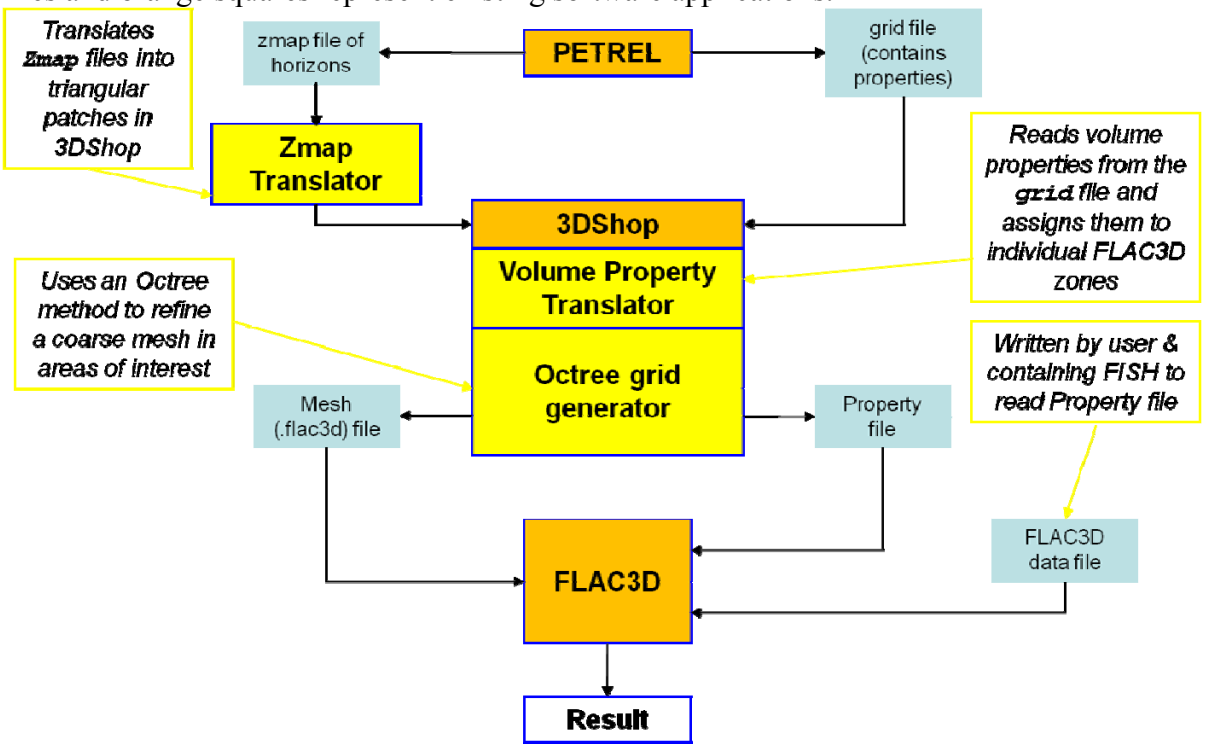

Figure 6-22: PETREL to FLAC3D Workflow Diagram

The various steps involved in creating a working FLAC3D model are as follows:

I. Collecting Geometry and Translation into STL files

1. Collect the following items
   1) **Grid file**. In PETREL, export a grid file representing a parallelepiped. The file must contain the properties that you are would like to assign to FLAC3D elements (porosity, density, etc…). All dimensions are in feet.
   2) **Horizons in the zmap format.** The file must cover the same parallelepiped, with all dimensions in feet.

II. Translate the horizons:

3) Run**:**

Kubrix –i waterbottom –it zmap –translate stl

This produces a file called **x.stl**

4) Rename **x.stl** to **w.stl (mv x.stl p1.stl)**
5) Run:

Kubrix –i pleist1 –it zmap –translate stl

6) mv **x.stl p1.stl**
7) repeat the same operation with pleist2, unconform1 and unconform2
8) …….

At the end, we have 5 files: **w.stl, p1.stl, p2.stl, u1.stl, u2.stl**

III. Creating the Horizon Model & Determining the Extent of the FLAC3D Grid

1. Run 3DShop
   1) Create a new document
   2) Insert **w.stl, p1.stl, p2.stl, u1.stl, u2.stl** in the new document
   3) Save the complete model as: **a1.stl**
   4) Reflect the entire model with respect to the z = 0 plane
   5) Save the complete model, again, as: **a1.stl**

You have created the input geometry

2. Determine the box containing the FLAC3D mesh…
   1) Determine the smallest and largest x,y and z of the model using 3DShop.

IV. Create the FLAC3D Mesh Based on a1.stl (Preparation)

3. Run 3DShop…
   1) Read in **a1.stl**
   2) Select **Applications|kubrix|Hexahedral Meshing.** The Hexahedral Meshing dialog box opens…
   3) Click on Default to enter default values in all fields
   4) Enter the following string in the field marked New Keywords:

-mode octree -olevel 5 -obox 1646200 9733000 -5220 5800 4100 4000 -app petrel

   5) **Mode:** specifies the custom Octree mesh type
   6) **Olevel:** specifies the level of Octree mesh generation
   7) **Obox**: specifies the position of the box: the first 3 floats are the coordinates of the center of the box and the next 3 indicate the dimensions of the box
   8) **app:** specifies the custom application

V. Create the FLAC3D Mesh Based on a1.stl (Mesh Generation)

4. Click on Compute…
   1) 3DShop reads **a1.stl**
   2) Creates and octree mesh that fits in the box specified by **obox** with **olevel** number of levels
   3) Parses the grid file, extracts the cells
   4) Extracts the properties
   5) Computes the contribution of each PETREL cell to each FLAC3D element
   6) Outputs PetrelProperties.dat
   7) Outputs a1.flac3d

VI. Output from 3DShop

```
PORO
0.086446
0.0812567
0.0964004
.
.
.
.
0.0813897
0.0840277
0.0865843
0.0791058
DENSITY
1.13922
1.06322
1.26
1.18523
1.21041
.
.
.
.
1.06196
1.19866
1.20858
1.07038
```

```
*
* FLAC3D input deck produced by KUBRIX version 9.3.0
* mesh built: Thu May 03 07:14:01 2007
* -app 3dshop -i C:\Documents and Settings\Reza Tagh
Taghavi\Desktop\Itasca\geo\Schlumberger032307\a1.fla
-obox 1646200 9733000 -5220 5800 4100 4000
*
*GRIDPOINTS
G 1, 1.643300e+006, 9.730950e+006, -7.220000e+003
G 2, 1.649100e+006, 9.730950e+006, -7.220000e+003
G 3, 1.649100e+006, 9.735050e+006, -7.220000e+003
G 4, 1.643300e+006, 9.735050e+006, -7.220000e+003
.
.
.
.
G 11593, 1.648919e+006, 9.734922e+006, -4.470000e+00
G 11594, 1.649100e+006, 9.734922e+006, -4.470000e+00
G 11595, 1.648919e+006, 9.735050e+006, -4.470000e+00
*ZONES
Z B8 1, 9, 47, 35, 36, 48, 37, 49, 50
Z B8 2, 47, 2, 48, 49, 51, 50, 52, 53
Z B8 3, 35, 48, 10, 37, 54, 41, 50, 55
.
.
.
.
Z B8 8889, 11577, 11578, 11589, 11581, 11590, 11593,
Z B8 8890, 11583, 11589, 11585, 11587, 11591, 2324,
Z B8 8891, 11589, 11590, 11591, 11593, 11592, 11595,
*GROUPS
ZGROUP group1
1290 1292 1293 1294 1295 1300 1302 1304 1305 1306 13
1318 1319 1320 1321 1323 1328 1330 1336 1337 1338 13
.
```

Figure 6-23: PetrelProperties.dat and a1.flac3d files

VII. Running FLAC3D

8) Run FLAC3D
9) Run ReadPetrelProperties.fis
10) Remove water
11) Attach face **tol 1**
12) Complement missing properties
13) Manage model through FISH

Conclusions

The objective of this multi-year, multi-institutional research project was to develop the knowledge base and quantitative predictive capability for the description of geomechanical performance of hydrate-bearing sediments (HBS) in oceanic environments. The focus was on the determination of the envelope of hydrate stability under conditions typical of those related to the construction and operation of offshore platforms. On the basis of our work, we offer the following conclusions:

Pore Scale Modeling by UCB

- We modeled the mechanical deformation of HBS or, more generally, of a granular medium, by numerical simulations of a pack of elastic spherical grains. Although this approach cannot entirely displace laboratory tests as the ground truth, it offers some opportunities which may be not available otherwise.
- Grain-scale simulations provide unique insights into the processes and phenomena underlying the classical continuum-medium models.
- A grain-scale model of granular material has been verified against available experimental data and numerical simulations by others. The model is based on the principle of quasi-static equilibrium, and uses physical parameters as input data, with no adjustments for calibration.
- After successful verification, the model has been applied to quantitative estimates of the impact of hydrate dissociation on the mechanical strength of hydrate-bearing sediments. The results have been reported in journal publications, presented at a number of scientific conferences and invited seminars.
- Hydrate dissociation is modeled as the shrinking of a part of the solid skeleton that is the hydrate "grains". A decrease of the effective stress is related to the evolution of trapped gas.
- Simulations show that excess pore pressure causes an almost instantaneous dramatic weakening of shear strength of the formation. Although these simulations treat the magnitude of the growing pore pressure as an input parameter, they show that if the gas formed by the dissociation is trapped, the loss of the ocean floor stability can be dramatic.
- Ultimately, stability of the slope at the ocean floor can be predicted by the coupled large-scale simulations that account for both fluid flow and geomechanics. Such simulations require input in the form of trend curves, which are determined by the micromechanics of the medium.

TOUGH+/FLAC3D Model Development by LBNL

- We coupled the TOUGH+/HYDRATE code (developed by LBNL and used for the description of system behavior in HBS) with FLAC3D (a commercial code that is widely used in soil and rock mechanics engineering and for scientific research in academia).
- TOUGH+/HYDRATE allows the study of flow and transport of fluids (distributed among four phases) and heat in hydrate deposits, and accurately describes the ther-

modynamics of hydrates as they are distributed among fifteen possible states (i.e., phase coexistence combinations).

- FLAC3D has built-in constitutive mechanical models suitable for soil and rocks, including various elastoplastic models for quasi-static yield and failure analysis, and viscoplastic models for time-dependent (creep) analysis.
- The coupled model is the first of its kind, can be used for the joint analysis of hydraulic, thermal, flow and geomechanical behavior in HBS, and is a unique tool for the analysis of the effect of hydrate dissociation processes on the structural stability and possible displacement of HBS and of their overburdens.
- Presently we have developed a novel simulator for analysis of geomechanical performance of HBS and we already applied the simulator on studies related to the geomechanical behavior of both offshore (oceanic) and onshore (sub-permafrost) hydrate deposits.
- In these studies we have addressed the questions about the geomechanical performance of the HBS and the potential for well bore instability and casing deformation.
- The next step will be to expand our analysis to two-way coupled effects, i.e. investigating the effect of compaction-induced changes in porosity and permeability on the production performance.

Simulation of Gas Production from Hydrates Using TOUGH+Hydrate by TAMU

We have used **TOUGH+Hydrate** to simulate the observed gas production and reservoir pressure field data at Messoyakha. We simulated various scenarios that help to explain the field behavior. Due to limited data, we constructed a number of 2D cross sectional models to answer as many questions as possible. We list here important conclusions.

- Our simulation results indicate that the published description of the Messoyakha Field as a hydrate layer, underlain by a free gas layer, and a weak aquifer is the correct description.
- As the gas in the free gas layer was produced, the pressure and temperature declined, and as much as 15-20% of the gas produced during the early years at Messoyakha came from gas hydrate dissociation.
- We simulated the reservoir pressure increase after the wells were shut-in in 1979 by decreasing the vertical permeability in the gas hydrate zone to 0.01 to 0.1 md. These values of vertical permeability are likely caused by the thin shale layers that exist in the Dolgon formation.
- Our modeling shows that if the perforations are close to the hydrate-gas interface, the rapid cooling due to both hydrate dissociation and the Joule-Thomson cooling effect will lead to the formation of secondary hydrates around the perforation (perforation choking). The formation of secondary hydrates will lead to reduction in permeability (essentially a damaged zone) that can lead to a rapid decrease in gas flow rates. The damage can be removed by injecting solvents or heat to melt the secondary gas hydrates.
- We need to know for sure if the gas-water contact at Messoyakha has moved during the life of the field. If we believe that the gas-water contact has not moved with time, the increase in pressure due to continued hydrate dissociation after shut-in is a plausible scenario. Otherwise, the increase of reservoir pressure can be simulated using an intermediate strength aquifer.

- It is important to know the absolute permeability of hydrate bearing rock for production as well as geomechanical issues. The absolute permeability is responsible to change the pressure profile in a hydrate reservoir and more so in a hydrate capped gas reservoir. If the hydrates make the rock "tighter", the feasibility of other stimulation techniques such as hydraulic fracturing must be studied in detail.
- Hydrate saturation has an important effect on gas recovery from Class 1G reservoirs. As the hydrate saturation decreases, the depressurization will be less effective as compared to high hydrate saturation case. This is because the gas is more compressible and hence it has less vigorous pressure wave traveling through it.

Laboratory Testing of Gas Hydrate Filled Core Samples for Rock Mechanics

- Lawrence Berkeley National Laboratory researchers developed an approach to forming hydrate bearing samples in fine-grained material and then designed and completed fabrication of a geomechanical properties and geophysical signature test cell.
- The method proposed follows these steps and the method was accepted by DOE in July, 2007, and can be summarized as follows:
    - Mix dry mineral components until visually homogeneous,
    - Add water using a pipette (for sand), by equilibrating in a humidified chamber (silt or clay), or by stirring in flakes of frost ice (samples containing clay) and mix thoroughly,
    - Pack moistened material into the sleeve,
    - Rapidly evacuate air from the sample,
    - Chill sample to the appropriate temperature,
    - Pressurize sample with methane gas, and monitor T, P until hydrate is formed,
    - Saturate with water.

To measure rock mechanical properties in the laboratory, LBNL designed and built a unique pressure vessel capable of

- forming methane hydrate in the pore space of sediments,
- applying a confining stress and independently applying an axial load,
- while allowing simultaneous measurements of the compressive and shear wave velocities,
- sample length, and
- spatially resolved sample density using x-ray CT scanning to observe sample structure

Summary of Petrel-FLAC3D Data Exchange by Schlumberger

- The PETREL model contains, among other things, the description of horizons and the special distribution of properties. As part of this project, an automatic method of creating a *FLAC3D* grid was developed. The resulting grid is composed of multiple materials representing the various regions of the *PETREL* database delimited by the horizons.
- In addition to the grid, an automatic and conservative method of extracting material properties from *PETREL* should was devised. The extracted properties can be automatically assigned to the individual *FLAC3D* grid element.
- When using *PETREL +FLAC3D*, the user should be aware that

    - Data sets extracted from *PETREL* may be very large. An automatic method has been devised to coarsen (decimate) the data, while maintaining pertinent details.
    - The *PETREL* model may contain features ranging in size from tens of meters to hundreds of kilometers, which requires a non-traditional meshing approach that would keep the total element count in the *FLAC3D* model to a minimum while ensuring adequate representation of details and adequate transition between *FLAC3D* element sizes.
    - Property transfer from *PETREL* to *FLAC3D* should be conservative.
- FLAC3D is a numerical model for the advanced geotechnical analysis of soil, rock, and structural support in three dimensions. FLAC3D is used in analysis, testing, and design by geotechnical, civil, and mining engineers. It is designed to accommodate any kind of geotechnical engineering project where continuum analysis is necessary.
- FLAC3D uses an explicit finite volume formulation that models complex behaviors not readily suited to finite element software, such as problems consisting of several stages, large displacements and strains, non-linear material behavior and unstable systems (yield/failure over large areas, or total collapse, etc.).

References

Abegg, F., Bohrmann, G. and Kuhs, W., 2006. Data report: shapes and structures of gas hydrates imaged by computed tomographic analyses, ODP Leg 204, Hydrate Ridge. In: A.M. Trehu, G. Bohrmann, M.E. Torres and F.S. Colwell (Editors), Proceedings of Ocean Drilling Program, Scientific Results, 204, College Station, Texas, pp. 1-11.

Boothe, J.S., Rowe, M.M. and Fischer, K.M., 1996. Offshore gas hydrate sample database: Open file report 96-272, United States Geological Survey, http://pubs.usgs.gov/of/1996/of96-272/index.html.

Boswell, R., Kleinberg, R.L., Collett, T. and Frye, M., 2007, Exploration priorities for marine gas hydrate resources. Fire in The Ice: Methane Hydrate R&D Newsletter, Spring/Summer 2007, 11-13, http://www.netl.doe.gov/technologies/oil-gas/FutureSupply/MethaneHydrates/newsletter/newsletter.htm.

Breitzke, M., 2006. Physical properties of marine sediments. In: H.D. Schultz and M. Zabel (Editors), Marine Geochemistry. Springer, Berlin, pp. 27-71.

Brooks, J.M., Cox, H.B., Bryant, W.R., Kennicutt, M.C., Mann, R.G. et al., 1986. Association of gas hydrates and oil seepage in the Gulf of Mexico. Organic Geochemistry. 10, 221-234.

Bryn, P., Berg, K., Forsberg, C.F., Solheim, A. and Kvalstad, T.J., 2005. Explaining the Storrega Slide. Marine and Petroleum Geology. 22(1-2), 11-19.

Carpenter, G.B., 1981. Coincident sediment slump/clathrate complexes on the U.S Atlantic slope. Geo-Marine Letters. 1, 29-32.

Center for Gas Hydrate Research - Heriot Watt University, 2007. What are gas hydrates?, http://www.pet.hw.ac.uk/research/hydrate/hydrates_what.htm.

Claypool, G.E. and Kaplan, I.R., 1974. The origin and distribution of methane in marine sediments. In: I.R. Kaplan (Editor), Natural Gases in Marine Sediments. Plenum Press, New York, pp. 99-139.

Collett, T., Lewis, R.E. and Dallimore, S.R., 2005. Mallik 5L-38 gas hydrate production research well downhole well-log and core montages. In: S.R. Dallimore and T. Collett (Editors), GSC Bulletin 585: Scientific results from the Mallik 2002 gas hydrate production well program, Mackenzie Delta, Northwest Territories, Canada. Geological Survey of Canada, pp. 23.

Conte, A. and Bloys, B., 2005. Cruise report - The Gulf of Mexico gas hydrate joint industry project, National Energy Technology Laboratory - US Department of Energy http://www.netl.doe.gov/technologies/oil-gas/FutureSupply/MethaneHydrates/rd-program/GOM_JIP/hydrates_main.html.

Cook, A.E., Goldberg, D. and Kleinberg, R.L., In Press. Fracture-controlled gas hydrate systems in Gulf of Mexico. Marine and Petroleum Geology.

Crutchley, G.J., Gorman, A.R. and Fohrmann, M., 2007. Investigation of the role of gas hydrates in continental slope stability west of Fiordland, New Zealand. New Zealand Journal of Geology and Geophysics. 50, 357-364.

Dallimore, S.R. and Collett, T.S., 2005. Summary and implications of the Mallik 2002 gas hydrate production research well program. In: S.R. Dallimore and T.S. Collett (Editors), GSC Bulletin 585: Scientific results from the Mallik 2002 gas hydrate production research well program, Mackenzie Delta, Northwest Territories, Canada. Geological Survey of Canada, pp. 36.

Davie, M.K. and Buffett, B.A., 2001. A numerical model for the formation of gas hydrate below the seafloor. Journal of Geophysical Research. 106(B1), 497-514.
Dicharry, C., Gayet, P., Marion, G., Graciaa, A. and Nesterov, A.N., 2005. Modeling heating curve for gas hydrate dissociation in porous media. Journal of Physical Chemistry B. 2005(109), 17205-17211.
Field, M.E. and Barber, J.H.J., 1993. A submarine landslide associated with shallow seafloor gas and gas hydrates off Northern California. In: W.C. Schwab, H.J. Jee and D.C. Twichell (Editors), Submarine Landslides: Selected Studies in the U.S. Exclusive Economic Zone. U.S Geological Survey, pp. 971-972.
Francisca, F., Yun, T.S., Ruppel, C. and Santamarina, J.C., 2005. Geophysical and geotechnical properties of near-seafloor sediments in the northern Gulf of Mexico gas hydrate province. Earth and Planetary Science Letters. 237, 924-939.
Ginsburg, G., Soloviev, V., Matveeva, T. and Andreeva, I., 2000. Sediment grain-size control on gas hydrate presence, Sites 994, 995 and 997. In: C.K. Paull, R. Matsumoto, P.J. Wallace and W.P. Dillion (Editors), Proceedings of Ocean Drilling Program, Scientific Results, 164, College Station, Texas, pp. 237-245.
Gracia, E., Martinez-Ruiz, F., Pinero, E., Larrasoana, J.C., Vizcanio, A. et al., 2006. Data Report: Grain-size and bulk and clay mineralogy of sediments and the presence of gas hydrate in Hydrate Ridge. In: A.M. Trehu, G. Bohrmann, M.E. Torres and F.S. Colwell (Editors), Proceedings of Ocean Drilling Program, Scientific Results, 204, College Station, Texas, pp. 1-19.
Hammerschmidt, E.G., 1934. Formation of gas hydrates in natural gas transmission lines. Industrial and Engineering Chemistry. 26(8), 851-855.
Handa, Y.P. and Stupin, D., 1992. Thermodynamic properties and dissociation characteristics of methane and propane hydrates in 70 Å radius silica gel pores Journal of Physical Chemistry. 96(21), 8599-8603.
He, L., Matsubayashi, O. and Lei, X., 2006. Methane hydrate accumulation model for the Central Nankai accretionary prism. Marine Geology. 227, 201-214.
Hesse, R. and Harrison, W.E., 1981. Gas hydrates (clathrates) causing pore-water freshening and oxygen isotope fractionation in deepwater sedimentary sections of terrigenous continental margins. Earth and Planetary Science Letters. 55, 453-462.
Holditch, S., 2006. Tight gas sands. Journal of Petroleum Technology. 58(6), 86-93.
Huang, D. and Fan, S., 2005. Measuring and modeling thermal conductivity of gas hydrate bearing sand. Journal of Geophysical Research. 110(B01311), 1-10.
Hyndman, R.D. and Davis, E.E., 1992. A mechanism for the formation of methane hydrate and seafloor bottom simulating reflectors by vertical fluid expulsion. Journal of Geophysical Research. 97(B5), 7025-7041.
Itasca Consulting Group, 2002. FLAC3D: Fast Lagrangian Analysis of Continua in 3 Dimensions, Minneapolis.
Janik, A., Goldberg, D., Collett, T. and Leg 204 Scientific Party, 2003. Azimuthal variability in gas hydrate concentration using LWD resistivity and density images EOS Transactions, 84(46/Supplement), Abstract OS51C-0875.
Kilner, J.R. and Grozic, J.L.H., 2006. Determination of synthetic hydrate content in sand specimens using dielectrics Canadian Geotechnical Journal. 43, 551-562.
Kitajima, H., Noda, H., Chester, F.M. and Shimamoto, T., 2007. Hydraulic and frictional properties of natural clay-rich sediments from OPD Leg 190 Nankai Trough and IODP expedition 311 Cascadia Margin EOS Transactions, 88(52), Abstract S21B-0569.

Klauda, J.B. and Sandler, S.I., 2005. Global distribution of methane hydrate in ocean sediment. Energy and Fuels. 19, 459-470.
Kleinberg, R.L., 2006. New deposit accumulation model for marine gas hydrates, Offshore Technology Conference. Society of Petroleum Engineers, Houston, Texas.
Kneafsey, T.J., 2007. Staff Scientist, Lawrence Berkeley National Laboratory, Personal Communication.
Kneafsey, T.J., Tomutsa, L., Moridis, G.J., Seol, Y., Friefeld, B.M. et al., 2007. Methane hydrate formation and dissociation in a partially saturated core-scale sand sample. Journal of Petroleum Science and Engineering. 56(1-3), 108-126.
Kono, H.O., Narasimhan, S., Song, F. and Smith, D.H., 2002. Synthesis of methane gas hydrate in porous sediments and its dissociation by depressurizing Powder Technology. 122, 239-246.
Krason, J. and Ciesnik, M., 1985. Geological evolution and analysis of confrmed or suspected gas hydrate localities. DOE/MC/21181-1950, US Department of Energy, Morgantown, West Virginia.
Krason, J. and Finley, P.D., 1992. Messoyakh Gas Field - Russia West Siberian Basin, American Association of Petroleum Geologists - Treatise of Petroleum Geology, Structural Traps VII, pp. 197-220.
Kumar, P., Turner, D. and Sloan, E.D., 2004. Thermal difffusivity measurements of porous methane hydrate and hydrate-sediment mixtures. Journal of Geophysical Research. 109(B01207), 1-8.
Kunerth, D.C., Weinberg, D.M., III, J.W.R., Scott, C.L. and Johnson, J.T., 2001. Acoustic laboratory measurements during the formation of a THF hydrate in unconsolidated porous media. Journal of Seismic Exploration. 9, 337-354.
Kvalstad, T.J., Andresen, L., Forsberg, C.F., Berg, K., Bryn, P. et al., 2005. The Storegga Slide: evaluation of triggering sources and slide mechanics. Marine and Petroleum Geology. 22(1-2), 245-256.
Kvenvolden, K.A. and McMenamin, M.A., 1982. Hydrates of natural gas: A review of their occurence. US Geological Survey Circular 825, pp. 11.
Liang, M., Chen, G., Sun, C., Yan, L., Liu, J. et al., 2005. Experimental and modeling study on decomposition kinetics of methane hydrates in different media. Journal of Physical Chemistry B. 109, 19034-19041.
Liu, X. and Flemings, P.B., 2007. Dynamic multiphase flow model of hydrate formation in marine sediments. Journal of Geophysical Research. 112(B3), B01301.
Macdonald, I.R., Guinasso, N.L., Sassen, R., Brooks, J.M., Lee, L. et al., 1994. Gas hydrates that breaches the seafloor on the continental slope of the Gulf of Mexico. Geology. 22, 699-702.
Makogon, Y.F., 1965. Hydrate formation in gas bearing beds under permafrost conditions. Gazovaia Promyshlennost. 5, 14-15.
Makogon, Y.F., 1966. Specialties of exploitation of the natural gas hydrate fields in permafrost conditions. Vniiegazprom. 11(4), 1-12.
Makogon, Y.F., 1974. Hydrates of natural gases. NEDRA, Moscow.
Makogon, Y.F., 1981. Hydrates of natural gases. PennWell, Tulsa, Oklahoma.
Makogon, Y.F., 1984. Production from nautral gas hydrate deposits. Gazovaya Promishlennost. 10, 24-26.
Makogon, Y.F., 1988. Natural gas hydrates - the state of study in the USSR and perspectives for its use, Third Chemical Congress of North America, Toronto, Canada.
Makogon, Y.F., 1997. Hydrates of hydrocarbons. PennWell, Tulsa, Oklahoma.

Makogon, Y.F., 2007. Professor Emeritus - Petroleum Engineering Department, Texas A&M University, Personal Communication.
Makogon, Y.F., Holditch, S.A. and Makogon, T.Y., 2005. Russian field illustrates gas-hydrate production. Oil and Gas Journal. 103(5), 43-47.
Makogon, Y.F., Holditch, S.A. and Makogon, T.Y., 2007. Natural gas hydrates - A potential energy source for the 21st century. Journal of Petroleum Science and Engineering. 56(1-3), 14-31.
Makogon, Y.F., Trebin, F.A., Trofimuk, A.A. and Chersky, N.V., 1971. Detection of a pool of natural gas in a soild hydrated state. Doklady Akademii Nauk SSSR. 196(1), 197-200.
Makogon, Y.F., Tsarev, V.P. and Chersky, N.V., 1970. Gas-hydrate resource in the offshore, 17th World Gas Congress, Moscow.
Masui, A., Haneda, H., Ogata, Y. and Aoki, K., 2005. The effect of saturation degree of methane hydrate on the shear strength of synthetic methane hydrate sediments, 5th International Conference on Gas Hydrates, Trondheim, Norway, pp. 657-663.
Max, M.D., Johnson, A.H. and Dillon, W.P., 2006. Economic Geology of Natural Gas Hydrates (Coastal Systems and Continental Margins). Springer, Dordrecht, 341 pp.
Meyerhoff, A.A., 1980. Petroleum basins of the Soviet Arctic. Geological Magazine. 117(2), 101-210.
Mienert, J., Vanneste, M., Bunz, S., Andreassen, K., Haflidason, H. et al., 2005. Ocean warming and gas hydrate stability on the mid-Norwegian margin at the Storrega Slide. Marine and Petroleum Geology. 22, 233-244.
Milkov, A.V., 2000. Worldwide distribution of submarine mud volcanoes and associated gas hydrates. Marine Geology. 167, 29-42.
Milkov, A.V., 2005. Molecular and stable isotope compositions of natural gas hydrates: a revised global dataset and basic interpretations in the context of geological settings. Organic Geochemistry. 36, 681-702.
Milkov, A.V., Claypool, G.E., Lee, Y.-J. and Sassen, R., 2005. Gas hydrate systems at Hydrate Ridge offshore Oregon inferred from molecular and isotopic properties of hydrate-bound and void gases. Geochimica et Cosmochimica Acta. 69(4), 1007-1026.
Milkov, A.V. and Sassen, R., 2000. Thickness of the gas hydrate stability zone, Gulf of Mexico continental slope. Marine and Petroleum Geology. 17, 981-991.
Milkov, A.V. and Sassen, R., 2002. Economic geology of offshore gas hydrate accumulations and provinces. Marine and Petroleum Geology. 19, 1-11.
Milkov, A.V. and Sassen, R., 2003. Preliminary assessment of resources and economic potential of individual gas hydrate accumulations in the Gulf of Mexico continental slope. Marine and Petroleum Geology. 20, 111-128.
Moridis, G.J., 2003. Numerical studies of gas production from methane hydrates. SPE Journal. 8(4).
Moridis, G.J., 2004. Numerical studies of gas production from Class 2 and Class 3 hydrate accumulations at the Mallik site, Mackenzie Delta, Canada. SPE Reservoir Evaluation and Engineering. 7(3), 175-183.
Moridis, G.J. and Collettt, T., 2003. Strategies for gas production from hydrate accumulations under various geologic conditions. LBNL-52568, Lawrence Berkeley National Laboratory, Berkeley, California.

Moridis, G.J. and Collettt, T., 2004. Gas production from Class 1 hydrate accumulations. In: C. Taylor and J. Kwan (Editors), Recent Advances in the Study of Gas Hydrates, pp. 75-88.
Moridis, G.J., Collettt, T., Dallimore, S.R., Satoh, T., Hancock, S. et al., 2004. Numerical studies of gas production from several CH4 hydrate zones at the Mallik site, Mackenzie Delta, Canada. Journal of Petroleum Science and Engineering. 43(3-4), 219-238.
Moridis, G.J., Kowalsky, M.B. and Pruess, K., 2007. Depressurization-induced gas production from Class 1 hydrate deposits. SPE Reservoir Evaluation and Engineering. 10(5), 458-481.
Moridis, G.J., Kowalsky, M.B. and Pruess, K., 2008. TOUGH+Hydrate v 1.0 User's Manual: A code for the simulation of system behavior in hydrate bearing geologic media. Lawrence Berkeley National Laboratory, Berkeley, California.
Moridis, G.J. and Reagan, M., 2007. Gas production from oceanic Class 2 hydrate accumulations, Offshore Technology Conference, Houston, Texas.
Moridis, G.J. and Sloan, E.D., 2007. Gas production potential of disperse low-saturation hydrate accumulations in oceanic sediments. Energy Conversion and Management. 48(6), 1834-1849.
Nakagawa, S., 2007. Staff Scientist, Lawrence Berkeley National Laboratory, Personal Communication.
Nixon, M.F. and Grozic, J.L.H., 2007. Submarine slope failure due to gas hydrate dissociation: a preliminary quantification. Canadian Geotehcnical Journal. 44, 314-325.
Paul, C.K. and Ussler, I.W., 2001. History and significance of gas sampling during DSDP and ODP. In: C.K. Paul and W.P. Dillon (Editors), Natural Gas Hydrates: Occurrence, Distribution and Detection. American Geophysical Union, pp. 53-66.
Popenoe, P., Schmuck, E.A. and Dillon, W.P., 1993. The Cape Fear landslide: slope failure associated with salt diapirism and gas hydrate decomposition. In: W.C. Schwab, H.J. Lee and D.C. Twichell (Editors), Submarine Landslides-Selected Studies in the U.S. Exclusive Economic Zone: U.S. Geological Survey Bulletin B 2002, pp. 40-53.
Pruess, K., Oldenburg, C. and Moridis, G.J., 1991. A general purpose numerical simulator for multiphase fluid and heat flow. LBNL-29400, Lawrence Berkeley National Laboratory, Berkeley, California.
Rempel, A.W. and Buffett, B.A., 1997. Formation and accumulation of gas hydrate in porous media. Journal of Geophysical Research. 102(B5), 10,151-10.
Ruppel, C., Dickens, G.R., Castellini, D.G., Gilhooly, W. and Lizzarlde, D., 2005. Heat and salt inhibition of gas hydrate formation in the northern Gulf of Mexico. Geophysical Research Letters. 32(L04605), 1-4.
Rutqvist, J., 2007. Staff Scientist, Lawrence Berkeley National Laboratory, Personal Communication.
Rutqvist, J., 2008. Staff Scientist, Lawrence Berkeley National Laboratory, Personal Communication.
Rutqvist, J., Grover, T. and Moridis, G.J., 2008. Coupled hydrological, thermal and geomechanical analysis of wellbore stability in hydrate bearing sediments, Offshore Technology Conference, Houston, Texas.
Rutqvist, J. and Moridis, G.J., 2007. Numerical studies on the geomechanical stability of hydrate-bearing sediments, Offshore Technology Conference, Houston, Texas.

Rutqvist, J. and Tsang, C.F., 2003. Analysis of thermal-hydrologic-mechanical behavior near an emplacement drift at Yucca Mountain. Journal of Contaminant Hydrology. 62-63, 637-652.
Santamarina, J.C., Francisca, F.M., Sun, T.S., Lee, J.Y., Martin, A.I. et al., 2004. Mechanical, thermal, and electrical properties of hydrate bearing sediments, AAPG Hedberg Conference. AAPG, Vancouver, BC, Canada.
Sapir, M.H., Khramenkov, E.N., Yefremov, I.D., Ginsburg, G.D., Beniaminovich, A.E. et al., 1973. Geologic and gephysical features of the gas hydrate deposits in the Messoiakh field. Geologiia Nefti i Gaza. 6, 26-34.
Sassen, R., 2007. Deputy Director, Resource Geochemistry, Geochemical and Ennvironmental Research Group, Texas A&M University - College Station, Personal Communication.
Sassen, R., Brooks, J.M., Macdonald, I.R., KennicuttII, M.C., Guinasso, N.L. et al., 1994. Association of oil seeps and chemosynthetic communities with oil discoveries, upper continental slope, Gulf of Mexico. Gulf Coast Association of Geological Societies Transactions. 44, 349-355.
Sassen, R., Joye, S., Sweet, S.T., DeFreitas, D.A., Milkov, A. et al., 1999a. Thermogenic gas hydrates and hydrocarbon gases in complex chemosynthetic communities, Gulf of Mexico continental slope. Organic Geochemistry. 30, 485-497.
Sassen, R., Joye, S., Sweet, S.T., DeFreitas, D.a., Milkov, A.V. et al., 1999b. Thermogenic gas hydrates and hydrocarbon gases in complex chemosynthetic communities, Gulf of Mexico continental slope. Organic Geochemistry. 30, 485-497.
Sassen, R. and Macdonald, I.R., 1994. Evidence of structure H hydrate, Gulf of Mexico continental slope. Organic Geochemistry. 22(6), 1029-1032.
Settari, A. and Mourits, F.M., 1998. A coupled reservoir and geomechanical simulation system. SPE Journal. 27(9), 219-226.
Sheshukov, N.L., 1973. Features of gas bearing strata with the hydrates. Geologiia Nefti i Gaza. 6, 20-26.
Shipboard Scientific Party, 1996. In: C.K. Paul, R. Matsumoto, P.J. Wallace, N.R. Black, W.S. Borowski et al. (Editors), Proceedings of Ocean Drilling Program, Initial Reports, 164, College Station, Texas.
Shipboard Scientific Party, 2003. Leg 204 Summary. In: A.M. Trehu, G. Bohrmann, F.R. Rack, M.E. Torres, N.L. Bangs et al. (Editors), Proceedings of Ocean Drilling Program, Initial Reports, 204, College Station, Texas, pp. 1-75.
Sloan, E.D. and Koh, C.A., 2008. Clathrate Hydrates of Natural Gases. CRC Press, Boca Raton, 752 pp.
Smith, D.H., Wilder, J.W. and Seshadri, K., 2002. Methane hydrate equilibria in silica gels with broad pore-size distributions AIChE Journal. 48(2), 393-400.
Smith, S., Boswell, R., Collett, T., Lee, M. and Jones, E., 2006. Alaminos Canyon Block 818: A documented example of gas hydrate saturated sand in Gulf of Mexico. Fire In The Ice: NETL Methane Hydrate R&D Newsletter. 12.
Spangenberg, E., Kulenkampff, J., Naumann, R. and Erzinger, J., 2005. Pore space hydrate formation in a glass bead sample from methane dissolved in water. Geophysical Research Letters. 32(L24301), 1-4.
Stern, L., Circone, S., Kirby, S. and Durham, W.B., 2001. Anolamous preservation of pure methane hydrate at 1 atm Journal of Physical Chemistry B. 105, 1756-1762.

Stern, L., Kirby, S. and Durham, W.B., 1996. Peculiarities of methane clathrate hydrate formation and solid-state deformation, including possible superheating of water-ice. Science. 273, 1843-1848.
Stone, H.L., 1970. Probability model for estimating three phase relative permeability. Journal of Petroleum Technology. 22(2), 214-218.
Su, X., Song, C.B. and Fang, N.Q., 2006. Relationship between sediment granulometry and the presence of gas hydrate on Hydrate Ridge. In: A.M. Trehu, G. Bohrmann, M.E. Torres and F.S. Colwell (Editors), Proceedings of Ocean Drilling Program, Scientific Results, 204, College Station, Texas, pp. 1-30.
Sultan, N., Cochonat, P., Canals, M., Cattaneo, A., Dennielou, B. et al., 2004a. Triggering mechanisms of slope instability processes and sediment failures on continental margins: a geotechnical approach. Marine Geology. 213, 291-321.
Sultan, N., Cochonat, P., Foucher, J.P. and Mienert, J., 2004b. Effect of gas hydrates melting on seafloor slope stability. Marine Geology. 231, 379-401.
Sun, C.-Y., Chen, G.-J. and Yang, L.-Y., 2004. Interfacial tension of methane+water with surfactant near the hydrate formation conditions. Journal of Chemical Engineering Data. 49, 1023-1025.
Tan, B., Germaine, J.T. and Flemings, P.B., 2006. Data report: consolidation and strength characteristics of sediments from ODP Site 1244, Hydrate Ridge, Cascadia continental margin. In: A.M. Trehu, G. Bohrmann, M.E. Torres and F.S. Colwell (Editors), Proceedings of Ocean Drilling Program, Scientific Results, 204, College Station, Texas.
Tohidi, B., Anderson, R., Clennell, M.B., Burgass, R.W. and Biderkab, A.B., 2001. Visual observation of gas hydrate formation and dissociation in synthetic porous media by means of glass micromodels. Geology. 29(9), 867-870.
Trehu, A.M., Long, P.E., Torres, M.E., Bohrmann, G., Collett, T.S. et al., 2004. Three-dimensional distribution of gas hydrate beneath southern Hydrate Ridge: constraints from ODP Leg 204. Earth and Planetary Science Letters. 222, 845-862.
Trehu, A.M., Torres, M.E., Bohrmann, G. and Colwell, F.S., 2006. Leg 204 Synthesis: Gas hydrate distribution and dynamics in the Central Cascadia Accretionary Prism Complex. In: A.M. Trehu, G. Bohrmann, M.E. Torres and F.S. Colwell (Editors), Proceedings of the Ocean Drilling Program, Scientific Results, 2004.
Uchida, T., Ebinuma, T., Takeya, S., Nagao, J. and Narita, H., 2002. Effects of pore sizes on dissociation temperatures and pressures of methane, carbon dioxide, and propane hydrates in porous media. Journal of Physical Chemistry B. 106, 820-826.
Uchida, T., Takeya, S., Chuvilin, E.M., Ohmura, R., Nagao, J. et al., 2004. Decomposition of methane hydrates in sand, sandstone, clays and glass beads. Journal of Geophysical Research. 109(B05206), 1-12.
US Department of Energy, 2007. http://www.netl.doe.gov/technologies/oil-gas/FutureSupply/MethaneHydrates/about-hydrates/estimates.htm,
Ussler, I.W. and Paul, C.K., 2001. Ion exclusion associated with marine gas hydrate deposits. In: C.K. Paul and W.P. Dillon (Editors), Natural Gas Hydrates: Occurrence, Distribution and Detection. American Geophysical Union, pp. 41-51.
Van Genutchen, M.T., 1980. A closed-form equation for predicting the hydraulic conductivity of unsaturated soils. Soil Science Society of America Journal. 44, 892-898.
Vogt, P.R. and Jung, W.Y., 2002. Holocene mass wasting on upper non-polar continental slopes - due to post-glacial ocean warming and hydrate dissociation? Geophysical Research Letters. 29(9), 55-1 - 55-4.

Waite, W.F., deMartin, B.J., Kirby, S.H., Pinkston, J. and Ruppel, C.D., 2002. Thermal conductivity measurements in porous mixtures of methane hydrate and quartz sand. Geophysical Research Letters. 29(24), 2229-2232.

Weinberger, J.L., Brown, K.M. and Long, P.E., 2005. Painting a picture of gas hydrate distribution with thermal images. Geophysical Research Letters. 32(L04609), 1-4.

Winters, W.J., 2000. Stress history and geotechnical properties of sediment from the Cape Fear Diapir, Blake Ridge Diapir and Blake Ridge. Ocean Drilling Program, Scientific Results. 164, 421-429.

Winters, W.J., Pecher, I.A., Waite, W.F. and Mason, D.H., 2004. Physical properties and rock physics models of sediment containing natural and laboratory-formed methane gas hydrate American Mineralogist. 89, 1221-1227.

Winters, W.J., Waite, W.F., Mason, D.H., Gilbert, L.Y. and Pecher, I.A., 2007. Methane gas hydrate effect on sediment acoustic and strength properties. Journal of Petroleum Science and Engineering. 56(1-3), 127-135.

Xu, W. and Germanovich, L.N., 2006. Excess pore pressure resulting from methane hydrate dissociation in marine sediments: A theoretical approach. Journal of Geophysical Research. 111(B01104), 1-12.

Xu, W. and Ruppel, C., 1999. Predicting the occurrence, dsitribution, and evolution of methane gas hydrate in porous marine sediments. Journal of Geophysical Research. 104(B3), 5081-5095.

Yun, T.S., Francisca, F.M., Santamarina, J.C. and Ruppel, C., 2005. Compressional and shear wave velocities in uncemented sediment containing gas hydrate. Geophysical Research Letters. 32(L10609), 1-5.

Yun, T.S., Narsilio, G.A. and Santamarina, J.C., 2007a. Physical characterization of core samples recovered from Gulf of Mexico. Marine and Petroleum Geology. In Press.

Yun, T.S., Santamarina, J.C. and Ruppel, C., 2007b. Mechanical properties of sand,silt and clay containing tetrahydrofuran hydrate. Journal of Geophysical Research. 112(B04016), 1-13.

Zatsepina, O.Y. and Buffett, B.A., 2001. Experimental study of the stability of CO2 hydrate in a porous medium. Fluid Phase Equilibria. 192, 85-102.

Appendix

SPE 114223

Micromechanics of Hydrate Dissociation in Marine Sediments by Grain-Scale Simulations

Holtzman Ran, SPE, UC Berkeley; **Dmitriy B. Silin**, SPE, UC Berkeley; and **Tad W. Patzek**, SPE, UC Berkeley

This paper was prepared for presentation at the 2008 SPE Western Regional and Pacific Section AAPG Joint Meeting held in Bakersfield, California, U.S.A., 31 March-2 April 2008.

Abstract

We seek to quantify the impact of hydrate dissociation on the strength of hydrate-bearing sediments. Dissociation of gas-hydrates in marine sediments converts the solid hydrate structure into liquid water and gas. Together with the associated pore pressure increase, this process reduces the stiffness of the sediments, which may fracture or be fluidized. If sediment failure occurs, seafloor subsidence and landslides can severely damage offshore infrastructure.

To evaluate the mechanical properties of a sediment sample, we simulate loading of a disordered pack of spherical grains by incremental displacements of its boundaries. The deformation is described as a sequence of equilibrium configurations. Each configuration is characterized by a minimum of the total potential energy. This minimum is computed using a modification of the conjugate gradient algorithm. We verify our model against published data from experiments on glass beads. Our simulations capture the nonlinear, path-dependent behavior of granular materials observed in experiments.

Hydrates are modeled as load-bearing solid particles within the pores. To simulate the consequences of dissociation, we reduce the solid fraction by shrinking the hydrate grains. The effect of the associated excess pore pressure is modeled by isotropic compression of the solid grains, and reduction in macroscopic effective stress. Weakening of the sediment is quantified as a reduction of the effective elastic moduli.

Introduction

Gas-hydrates are solid materials formed under a range of high pressures and low temperatures. Dissociation converts them into liquid water and free gas. The volumetric expansion of gas can lead to an appreciable increase in pore pressure,[1] reducing the effective stress. Thus, dissociation impacts the mechanical properties of hydrate-bearing sediments (HBS) by reducing both the solid fraction and the effective stress. Hydrate dissociation caused, for instance, by hot fluids produced from deep formations, can destabilize the ocean floor and lead to massive landslides[1] that can damage nearby structures such as off-shore platforms.

On the one hand, obtaining undisturbed HBS samples requires special coring which preserves the in-situ conditions. On the other hand, artificial creation of representative samples is difficult.[2] For these reasons, there is no single definitive model for the distribution of hydrates within the pore space.[3] This distribution depends on the formation mechanism, along with many other factors.

We seek to evaluate the mechanical response to dissociation of gas-hydrates in marine sediments. The response of composite materials such as HBS is determined by the interactions among discrete grains. Grain-scale numerical simulations have become a valuable tool in the study of granular materials.[4,5] Most grain-scale simulations are based on the Discrete Element Method (DEM).[6] In DEM, interactions between the particles are treated as a dynamic process, accounting for the inertia of the grains. However, tight constraints imposed on the time step used in the numerical integration,[7] make DEM simulations time-consuming. To accelerate computations and damp grain oscillations, material properties such as the density of the

grains and their contact stiffness are often adjusted[8,9] to unrealistic values.

In this paper, a physically-based discrete model is presented. We simulate an irregular pack of spherical grains, loaded by incremental displacements of its boundaries. The contact forces are determined by the Hertzian model, assuming frictionless contacts. Using a quasi-static model, we find the equilibrium configurations using a modification of the conjugate gradient (CG)[10] algorithm. This efficient computational procedure, implemented in Matlab by Holtzman, is also utilized to generate a dense initial arrangement required for simulations. The interactions between the hydrate and the sediment are considered from both the grain and the sample scale. The degradation of sediment strength is quantified via the reduction in elastic moduli.

Simulating quasi-static deformation

We simulate an experiment on a sample made of cohesionless grains in a rectangular container. The sample is loaded by incremental displacements of the container walls, allowing the grains to reach static equilibrium following each perturbation. Each equilibrium configuration is computed by minimizing the total potential energy of the system. The initial conditions are the positions of the grains, prior to the simulated test. The positions and orientations of the container walls provide for the boundary conditions.

Grain pack model. We model granular materials as a three-dimensional (3D) irregular ("random") packing of spherical grains, see **Fig. 1**. The grains are assumed to be homogenous and isotropic. To model heterogenous materials such as clastic sediments, we assign the grain properties from a given distribution of sizes and elastic moduli. The deformations are assumed to be small and localized near the contacts, allowing to approximate the shape of a deformed grain by a sphere. We hypothesize here that in a tight packing, the macroscopic stress is mostly affected by the normal component of the contact forces.[8,11,12] This assumption is based on the argument that the size of the asperities that resist lateral or angular displacements is much smaller than the size of the grains themselves. Thus, we only account for the normal force components.

The orientation and rotations of the grains are of no importance under the assumption of frictionless contact between spherical grains. In a fixed coordinate system, each grain is fully described by the coordinates of its center and its radius. Each configuration is characterized by the positions of the grain centers, providing $3N$ degrees of freedom for a pack of N grains. Given a reference configuration in equilibrium, we perturb the boundary conditions, forcing the grains to deform and rearrange to a new equilibrium configuration ("current"). Labeling all grains with a single index $i = 1, 2, \ldots, N$, we denote the radius-vector of the center of grain i by $\boldsymbol{r}_i$. Let $\boldsymbol{u}_i$ denote the displacement of grain i: $\boldsymbol{u}_i = \boldsymbol{r}_i - \boldsymbol{r}_{i(0)}$, where subscript (0) denotes the reference configuration, see Fig. 1. The radius of body i is

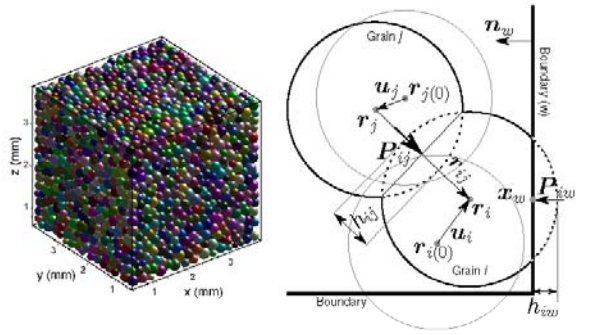

Fig. 1: Left: a typical pack with 5036 grains used in the numerical simulations. Right: schematic description of the contact geometry. The initial configuration of the grains is marked with grey dotted lines. The dashed lines represent grain overlap caused by deformations.

R_i, its mass is m_i, and the Young's modulus and Poisson's ratio of its material are E_i and ν_i, respectively. Subscript w denotes a boundary wall, $w = 1, 2, \ldots, 6$.

Contact model. According to Hertzian contact theory, the magnitude of the compressive normal force acting at the contact between a pair of grains i and j is

$$\|\boldsymbol{P}_{ij}\| = \frac{4}{3} E^*_{ij} \left(R^*_{ij}\right)^{1/2} \left(h_{ij}\right)^{3/2} \tag{1}$$

where $\|\boldsymbol{a}\| = (\boldsymbol{a} \cdot \boldsymbol{a})^{1/2}$ is the magnitude of a vector $\boldsymbol{a}$. Parameters $R^*_{ij} = \left(\frac{1}{R_i} + \frac{1}{R_j}\right)^{-1}$ and $E^* = \left[\frac{(1-\nu_i^2)}{E_i} + \frac{(1-\nu_j^2)}{E_j}\right]^{-1}$ are the effective radius and elastic coefficient associated with that contact, respectively. Eq. (1) is applicable to a grain-boundary contact, by modeling the latter as a grain of an infinite radius. The contact deformation is measured by the overlap $h_{ij} \geq 0$,

$$\begin{aligned} h_{ij} &= R_i + R_j - \|\boldsymbol{r}_{ij}\| && \text{for grain-grain contact} \\ h_{iw} &= R_i - (\boldsymbol{r}_i - \boldsymbol{x}_w) \cdot \boldsymbol{n}_w && \text{for grain-boundary contact} \end{aligned} \tag{2}$$

where $\boldsymbol{r}_{ij} = \boldsymbol{r}_i - \boldsymbol{r}_j$, $\boldsymbol{x}_w$ denotes the initial contact point with the wall w, and $\boldsymbol{n}_w$ is an inward unit normal to the wall, see Fig. 1. Here the orientation $\boldsymbol{n}_w$ was held fixed, and thus $\boldsymbol{x}_w$ can be chosen arbitrarily on w. The force acting on grain i at the contact with another grain j or a wall w is directed along $\boldsymbol{r}_{ij}$ or $\boldsymbol{n}_w$, respectively. Thus, no moment relative to the center of the grain is developed.

Obtaining equilibrium configurations. At equilibrium, the balance of forces for each grain yields three scalar equations. For N grains, the total number of equations is $3N$. The unknowns, i.e. the grain displacements, can be

written as a column vector $\boldsymbol{\theta} = [\boldsymbol{u}_1 \dots \boldsymbol{u}_N]^T$, where $\boldsymbol{u}_i$ is a row vector, and superscript T is the transpose. The exponent of 3/2 in Eq. (1) makes the system of equations nonlinear.

We seek an equilibrium configuration by employing an equivalent variational formulation. Namely, an equilibrium configuration is characterized by a set of displacements $\boldsymbol{\theta}$ corresponding to a minimum of the total potential energy of the system. This energy is a function of the deformations (strain energy) and the gravitational energy of the grains. The elastic strain energy of a pair of bodies in contact is equal to the sum of work done on each body to deform it. This work is the dot product of the force with the displacement increment, integrated over the total displacement. Thus, the strain energy U_{ij} stored in the deformed contact region between bodies i and j is (cf. Eq. (9.15) in Ref.[13])

$$U_{ij}(\boldsymbol{u}_i, \boldsymbol{u}_j) = \frac{8E^*_{ij}(R^*_{ij})^{1/2}}{15}(h_{ij})^{5/2} \tag{3}$$

The total potential energy of the system is the sum of the strain energy of all contacts and the gravitational potentials of all grains

$$\Pi(\boldsymbol{\theta}) = \sum_{i=1}^{N} \left\{ \frac{1}{2} \sum_{j=1}^{N^i_g} U_{ij} + \sum_{w=1}^{N^i_b} U_{iw} + m_i g(\boldsymbol{r}_i \cdot \hat{\boldsymbol{e}}_z - z^*) \right\} \tag{4}$$

Here z^* is an arbitrary fixed reference elevation, $\hat{\boldsymbol{e}}_z$ is a unit vector pointing opposite to the direction of gravity, and g is the gravity acceleration. N^i_g and N^i_b are the number of contacts for grain i with other grains and boundaries, respectively. Their sum $N^i_g + N^i_b$ is the coordination number of that grain. Note that the set of contacts for each grain varies with the deformation of the pack, introducing additional nonlinearity.

The gradient of Π with respect to $\boldsymbol{\theta}$ is a column vector $\nabla_\theta \Pi = -[\boldsymbol{F}_1 \dots \boldsymbol{F}_N]^T$, where the row vector $\boldsymbol{F}_i$ is the sum of forces on grain i,

$$\boldsymbol{F}_i = \sum_{j=1}^{N^i_g} \boldsymbol{P}_{ij} + \sum_{w=1}^{N^i_b} \boldsymbol{P}_{iw} - m_i g \hat{\boldsymbol{e}}_z \tag{5}$$

Thus, the vanishing gradient of Π is equivalent to the balance of forces. This minimum is found numerically using a modification of the CG algorithm, see Appendix.

Initial grain pack generation. Simulations of a deforming grain pack requires a sufficiently dense initial configuration.[14,15] Such an initial configuration could be obtained from a physical sample, e.g. using MRI[16] or X-ray tomography imaging.[17] However, these techniques are cumbersome. Alternatively, an initial irregular configuration could be generated numerically using wither "constructive" or "dynamic" algorithms. Constructive algorithms are based on geometry alone and thus require relatively small computing time; however, the current state-of-the-art constructive algorithms produce 3D arrangements with low coordination numbers, gaps, or anisotropic structure.[15] In dynamic algorithms, a loose packing is created by placing a relatively small number of grains in a bounded domain. Then, its density is increased by either expanding the grains or moving the boundaries closer together. A static equilibrium configuration is found by simulating intergranular interactions, e.g. using DEM. The large number of collisions and grain rearrangements makes such a procedure very time-consuming.[15]

Instead, we use our quasi-static algorithm, which provides an efficient alternative to DEM. Here, we start by selecting a portion of a pack generated by DEM,[18] bounding it by a rectangular domain. This packing is loose, with many grains supported by less than 4 contacts, rendering them mechanically unstable. To obtain a denser packing we first expand these unstable grains, until their coordination number reaches 4. Then, we shrink the pack by equal displacements of all boundaries, and apply our algorithm to obtain an equilibrium configuration. This process is repeated until practically* all grains have coordination number of 4 or more, and appreciable contact forces develop.

Evaluating macroscopic stress and strain. Macroscopic, continuum parameters such as stress and strain can be obtained from grain-scale parameters by spatial averaging. However, there are several methods for transforming between discrete and continuum parameters, in particular for the strain.[19] Here we consider the pack to be a homogenous representative volume of a larger medium, and compute the average stress and strain within this volume as described below.

The external normal forces applied on the boundaries are calculated from the sum of the contact forces on the container walls. The average normal stresses are evaluated by dividing these external forces by the area of the respective walls. To confirm the validity of our stress evaluation procedure, we also calculate the averaged Cauchy stress, taking into account the entire set of contact forces within the sample volume.[20] This calculation yielded similar values to those obtained from our procedure.

To estimate numerically the macroscopic strains $\boldsymbol{\epsilon} = \frac{1}{2}\left[\nabla_x \boldsymbol{u} + (\nabla_x \boldsymbol{u})^T\right]/2$, we replace the derivatives with finite differences. In the last equation $\boldsymbol{x}$ is a radius-vector to an infinitesimal volume, and $\boldsymbol{u}$ is its displacement.[13] For a rectangular domain, the normal strain in the l-direction ($l = 1, 2, 3$) reduces to $\Delta L_l / L_{l(0)}$, where $\Delta L_l = L_l - L_{l(0)}$, L_l and $L_{l(0)}$ being the current and the reference (undeformed) length of the domain in that direction, respectively. In our simulations, the macroscopic strains serve as boundary conditions, enforced by displacing the container walls. By applying uniform or different normal strains in three principal directions, we simulate an isotopic or

*A complete elimination of unstable grains may not be possible[11] because of grain sizes variation: the opening between large grains can be large enough to contain a small grain, not in stable equilibrium.

a polyaxial test. A uniaxial test is simulated by applying strain in a single direction.

Macroscopic elastic moduli. To describe mechanical properties as they evolve with the deformation, we discretize the load path and assign a set of constant effective elastic moduli for each loading interval. The moduli for each interval are evaluated by fitting the stress-strain results with Hooke's law. Hooke's law for a homogenous, isotropic body is $\boldsymbol{\sigma} = \lambda \mathrm{tr}(\boldsymbol{\epsilon})\hat{\boldsymbol{I}} + 2G\boldsymbol{\epsilon}$, where $\boldsymbol{\sigma}$ is the stress tensor, $\mathrm{tr}(\boldsymbol{\epsilon})$ is the trace of $\boldsymbol{\epsilon}$, and $\hat{\boldsymbol{I}}$ is the unit second order tensor. The moduli λ and G are Lame's constant and the shear modulus, respectively. Other elastic moduli can be evaluated from λ and G.[13]

The moduli evaluated using the procedure above are the bulk-averaged, effective moduli, corresponding to an effective homogeneous and isotropic elastic medium. Because the moduli depend on the deformation, stress-induced anisotropy can develop when loads in different directions are significantly different,[21] as observed in our simulations. To verify whether a grain pack is isotropic, we simulate a polyaxial test and compare the moduli for each pair of principal directions. If they are similar within a given tolerance, we consider the response isotropic. We minimized stress-induced anisotropy by applying relatively isotropic strains, evaluating the moduli at different loads by a uniaxial test. Anisotropy can also develop if the number of grains in the pack is too small, as macroscopically isotropic systems may exhibit local anisotropy.[22] To avoid such scale-related anisotropy, we used packs with sides not smaller than ∼15 grain diameters. This length scale depends on the properties of the grains and their spatial arrangement, and was determined by trial and error. As a result of using the above measures, the estimates of the moduli in different directions were practically identical.

Model verification

Input parameters. To verify our model, we compare our estimated macroscopic moduli with those measured in experiments on spherical and relatively smooth glass beads. The elastic moduli of the grains were assigned mean values of $\bar{E} = 70$ GPa for Young's modulus and $\bar{\nu} = 0.2$ for Poisson's ratios.[23] In other simulations, quartz sand was modeled by assigning $\bar{E} = 100$ GPa and $\bar{\nu} = 0.15$.[24,25] The elastic moduli were normally distributed with a standard deviation of 10% of the mean. The radii of the grains were distributed uniformly between 0.07-0.13 mm. The density of both types of grains was taken to be 2.65 g/cm^3, Ref.[24]

Stress-Strain. To capture hysteresis and stress-induced anisotropy, we simulated loading-unloading cycle in a polyaxial test, on a pack of 2654 quartz grains (denoted by QUARTZ2654). The porosity and mean coordination number varied as 35.8-30.8% and 7.23-8.26, accordingly, with stresses of ∼50-300 MPa. To verify our model against experiments on glass beads, we simulated a test on a pack of 5036 glass beads (GLASS5036). For

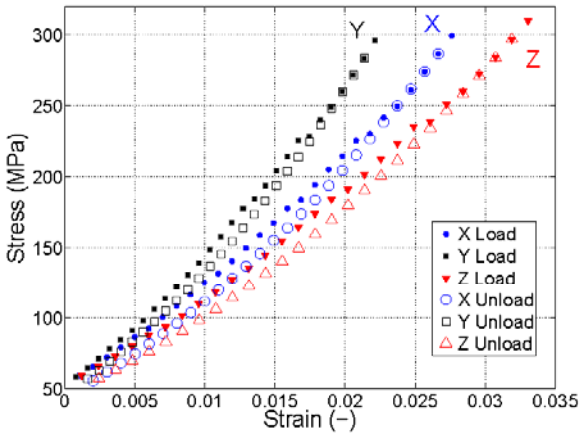

Fig. 2: Stress-strain curves obtained from numerical simulations of loading and unloading in a polyaxial test on QUARTZ2654. Hysteresis is evident as different loading and unloading curves.

GLASS5036, the porosity and mean coordination number varied as 37.1-35.7% and 6.48-6.97, accordingly, with stresses of ∼1-22 MPa. The stress-strain curves calculated for QUARTZ2654 are plotted in **Fig. 2**. A stress drop is noticeable, associated with variations in the complex network of contacts ("fabric") and contact forces.[5] Some of these microstructural variations are irreversible, contributing to the hysteretic response observed in experiments.[26] This hysteresis is evident in Fig. 2 as different loading and unloading curves. A more elaborate discussion and additional results will be published elsewhere.

Elastic moduli. The macroscopic elastic moduli for different stages of isotropic compression were evaluated for sample GLASS5036 by a uniaxial test. These moduli estimates are plotted in **Fig. 3** vs. the confining stress σ_c, defined by the mean of the lateral stresses perpendicular to the principal loading direction. The bulk modulus K estimates are in agreement with calculations from acoustic velocity data measured in experiments on glass beads,[23,27,28] though some values are slightly lower than the data. In addition, our predicted rate of moduli growth with σ_c agrees with the data, indicating that the moduli grow faster than the power law ${\sigma_c}^{1/3}$ predicted by the effective medium theory (EMT).[23]

At the same time, our shear modulus strongly underestimates the experimental data. In particular, at lower stresses, the evaluated shear modulus drops sharply, becoming negligibly small as the mean coordination number approaches 6 and the porosity exceeds ∼37%. Similar loss of shear rigidity was observed in DEM simulations using a frictionless contact model.[29] We consider the discrepancies between our predictions and the data to be caused by the frictionless contact assumption, as the shear modulus greatly depends on the intergranular shear.[29]

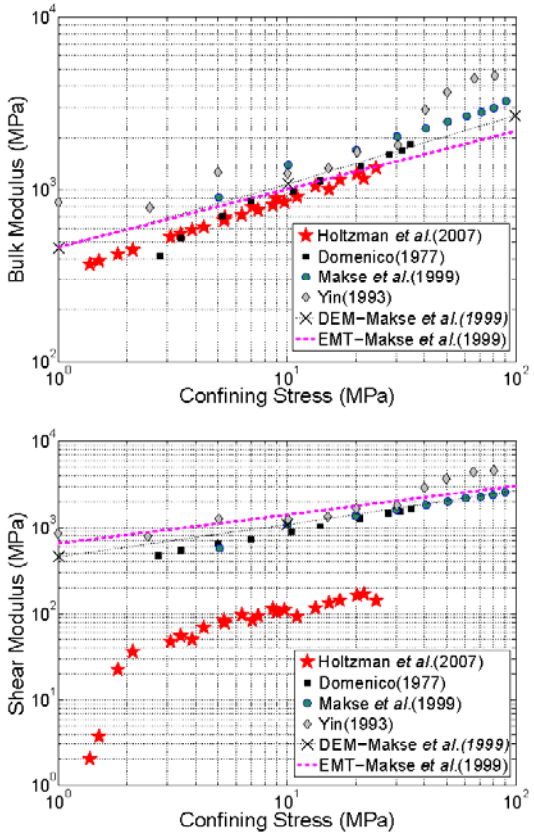

Fig. 3: The evaluated effective bulk (top) and shear (bottom) modulus from our simulations using GLASS5036 vs. the confining stress σ_c. Also shown are calculations from acoustic velocities measured in glass beads,[23,27,28] in addition to results from DEM simulations and effective medium theory (EMT),[23] obtained by digitizing Figure 1 in Ref.[23]

Impact of hydrate dissociation

Modeling hydrate dissociation. We use the procedure described above to quantify the mechanical response to hydrate dissociation in HBS. Dissociation impacts the mechanical properties of HBS by reducing both the solid fraction and the effective stress. The excess pressure due to dissociation varies with factors such as dissociation rate, sediment permeability, and initial pore pressure.[1] Predicting this excess pressure as a function of dissociation is outside the scope of this paper. Thus, we consider a number of dissociation scenarios, for a range of possible dissociation amounts and excess pressures. This range, taken from other models,[1] is used as input parameters in our simulations.

To model the interaction between the sediment and the hydrate, we consider methane-hydrate formed preferentially in the larger pores, rather than in the pore-throats. Such distribution makes hydrates a part of the granular frame, i.e. load-bearing solid particles. Such hydrate distribution can represent sediments with low hydrate saturation, where the gas is slowly introduced in the aqueous phase.[2] The distribution of hydrates within the pore space depends on the formation mechanism, among other factors, and a wide variety of distribution models exists.[3]

The hydrate saturation is defined by $S = V^h/V$, where V^h is the volume occupied by hydrate and V is the total pore volume (including the hydrate). We quantify the amount of dissociation by the decrement of hydrate saturation $\Delta S < 0$, decreasing the saturation to $S + \Delta S$. The reduction in solid fraction due to dissociation is modeled by shrinking the hydrate grains. The impact of the excess pore pressure p_{ex} is modeled at both the grain and the sample level. At the grain scale, with the assumption of small deformations, the contact area is much smaller than the surface area of the grains. Thus, assuming uniform pore pressure within the sample, the grains experience isotropic compression, with a net force applied by the fluid pressure which is practically zero. The volume of grain i, V_i, changes by $\Delta V_i < 0$, determined by $-p_{ex} = K_i \epsilon_{kk,i}$, where K_i and $\epsilon_{kk,i}$ are the bulk modulus and the volumetric strain of grain i, respectively. For small changes, $\epsilon_{kk,i} \approx \Delta V_i/V_i$. At the sample scale, the reduction in effective stress is modeled by applying a tensile macroscopic strain $\epsilon_{kk} > 0$, expanding the sample isotropically. This strain is determined from the poroelastic constitutive equation $\alpha_{bw} p_{ex} = K \epsilon_{kk}$, where α_{bw} is the Biot-Willis coefficient.[30]

Elastic moduli reduction by hydrate dissociation. The effect of dissociation in HBS is quantified via the evolution of the elastic moduli. The initial state of an HBS sample is modeled as a dense arrangement of spherical grains, where some of the smallest grains are considered to be methane-hydrate. These hydrate grains are linearly-elastic, with moduli of $E = 6.6$ GPa and $\nu = 0.32$ and density of 0.9 g/cm^3, Ref.[31] To model quartz sand as the host sediment, the other grains were assigned properties of quartz. The initial porosity and hydrate saturation was $\phi \approx 45\%$ and $S = 0.215$, respectively. The effective stress for this initial packing, determined from the contact forces on the walls, was ~21 MPa. The pack is considered to be under a specified initial pore pressure, which may be larger than hydrostatic pressure if the sediment is confined by a low-permeability layer. The resulting total stress, which is considered fixed in our simulations, can exceed the lithostatic stress if the sediment carries the weight of a nearby off-shore platform.

By varying the excess pressure p_{ex} and the saturation reduction ΔS independently, we produce a series of configurations, covering a range of possible scenarios. For each configuration, the elastic moduli are evaluated by simulating a uniaxial test. In **Fig. 4** (top), these moduli are plotted against the excess pressure p_{ex}, for a fixed change in saturation $\Delta S = -0.01$. Conversely, Fig. 4 (bottom) shows the moduli as functions of ΔS, for a fixed pressure $p_{ex} = 1$ MPa. The initial moduli prior to dissociation are

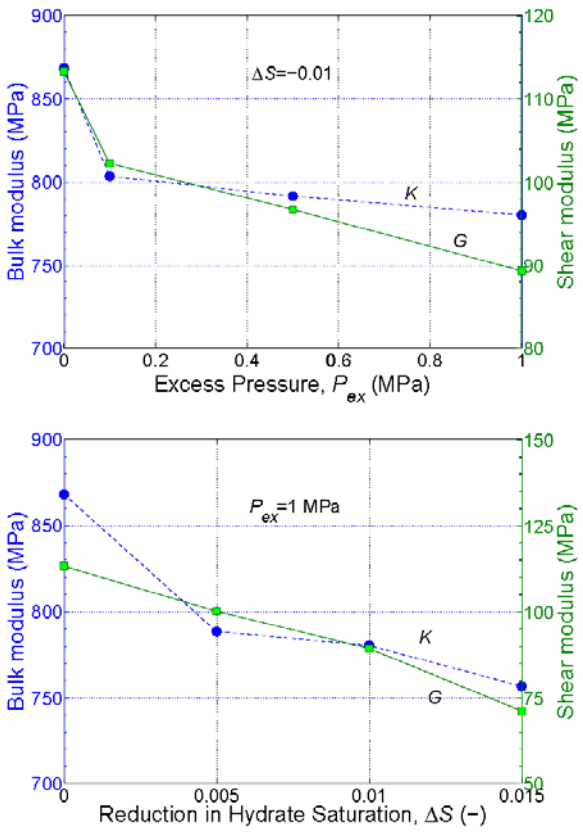

Fig. 4: Simulating reduction in bulk (dashed line) and shear (solid) modulus due to hydrate dissociation. Top: varying the excess pore pressure p_{ex}, for a fixed saturation decrement $\Delta S = -0.01$. Bottom: varying the saturation decrement ΔS, for a fixed excess pressures $p_{ex} = 1$ MPa.

plotted in the left-most parts of both figures. We used a value of $\alpha_{bw} = 0.8$, corresponding to that of sand.[25]

Weakening of HBS is evident from a reduction in elastic moduli, as the sediment becomes looser and softer. This observation is in qualitative agreement with experiments[2,3] and other numerical simulations.[32] Further dissociation may lead to a significant decrease in the solid support, reaching a critical state with loss of shear rigidity. In such a state, the sediment is more susceptible to landslides and subsidence, threatening the safety of adjacent off-shore platforms.

Discussion and conclusions

We quantify the mechanical effect of hydrate dissociation in marine sediments using grain-scale simulations. We describe HBS as a granular material, modeling an HBS sample as a three-dimensional, disordered packing of elastic spherical grains, bounded by a rectangular container.

We use a quasi-static model, where the pack is loaded by incremental displacements of the container walls. Each equilibrium configuration is found by minimizing the total potential energy of the system. A modification of the conjugate gradient algorithm is used to obtain this minimum. This approach results in an efficient computational procedure, which is also used to generate a dense initial arrangement.

The macroscopic stress, strain, and elastic moduli are evaluated from the contact forces and the displacements of the boundaries. Our results capture the nonlinear and path-dependent macroscopic strain-stress response observed in experiments, such as loading and unloading hysteresis.

We have verified our physics-based model against available experimental data. The good agreement between predicted and measured values of the macroscopic bulk modulus has been achieved with no adjustments of the relevant material properties. The macroscopic shear modulus evaluated from the simulations underestimates typical experimental data. We attribute this deficiency to the frictionless contact model employed, using the Hertzian contact theory. A more advanced model accounting for friction and inter-granular cementation will be presented elsewhere.

Hydrates are modeled as load-bearing solid particles within the pores. To simulate the consequences of dissociation, we reduce the solid fraction by shrinking the hydrate grains. The effect of the associated excess pore pressure is modeled by isotropic compression of the solid grains, and reduction in macroscopic effective stress.

A series of possible scenarios has been simulated, showing degradation of sediment strength as a reduction in the macroscopic elastic moduli. This trend agrees qualitatively with the published results of experiments and numerical simulations. Further dissociation might lead to a loss of solid support of the skeleton, causing seafloor instabilities such as landslides and subsidence. To predict such instabilities and their possible impact on off-shore platforms, our model can be used to produce constitutive relationships for large-scale simulations (e.g. Ref.[32]).

Acknowledgements

This work was supported by the Assistant Secretary for Fossil Energy, Office of Natural Gas and Petroleum Technology, through the National Energy Technology Laboratory, under the U.S. Department of Energy, Contract #DE-FC26-05NT42664.

References

[1] W. Xu and L. N. Germanovich. Excess pore pressure resulting from methane hydrate dissociation in marine sediments: A theoretical approach. *Journal of Geophysical Research*, 111:B01104, 2006.

[2] T. S. Yun, J. C. Santamarina, and C. Ruppel. Mechanical properties of sand, silt, and clay containing tetrahydrofuran hydrate. *Journal of Geophysical Research*, 112(B04106), 2007.

[3] W. Durham, L. Stern, S. Kirby, and S. Circone. Rheological comparisons and structural imaging of sI and

sII endmember gas hydrates and hydrate/sediment aggregates. In *Proceedings of the 5th International Conference on Gas Hydrates, 26-29 September 2004*, Trondheim, Norway, 2005.

[4] H. Kruggel-Emden, E. Simsek, S. Rickelt, S. Wirtz, and V. Scherer. Review and extension of normal force models for the discrete element method. *Powder Technology*, 171(3):157–173, 2007.

[5] A. A. Peña, A. Lizcano, F. Alonso-Marroquin, and H. J. Herrmann. Biaxial test simulations using a packing of polygonal particles. *International Journal for Numerical and Analytical Methods in Geomechanics*, 32(2):143–160, 2008.

[6] P. A. Cundall and O. D. L. Strack. A discrete numerical model for granular assemblies. *Geotechnique*, 29:47–65, 1979.

[7] C. O'Sullivan and J. D. Bray. Selecting a suitable time-step for discrete element simulations that use the central difference time integration approach. *Engineering Computations*, 21(2–4):278–303, 2004.

[8] C. Thornton. Numerical simulations of deviatoric shear deformation of granular media. *Geotechnique*, 50(1):43–53, 2000.

[9] C. O'Sullivan, J. D. Bray, and M. Riemer. Examination of the response of regularly packed specimens of spherical particles using physical tests and discrete element simulations. *Journal of Engineering Mechanics*, 130(10):1140–1150, 2004.

[10] W. H. Press, B. P. Flannery, S. A. Teukolsky, and W. T. Vetterling. *Numerical Recipes in Fortran 77*. Cambridge University Press, New York, 1986.

[11] C. Thornton and S. J. Antony. Quasi-static deformation of particulate media. *Philosophical Transactions of the Royal Society A: Mathematical, Physical and Engineering Sciences*, 356(1747):2763–2782, 1998.

[12] L. Rothenburg and R. J. Bathurst. Analytical study of induced anisotropy in idealized granular-materials. *Geotechnique*, 39(4):601–614, 1989.

[13] L. D. Landau and E. M. Lifshitz. *Theory of Elasticity*. Course of Theoretical Physics, Vol 7. Elsevier, Burlington, MA, 1986.

[14] C. O'Sullivan. *The application of discrete element modelling to finite deformation problems in geomechanics*. PhD thesis, University of California, Berkeley, CA, 2002.

[15] K. Bagi. An algorithm to generate random dense arrangements for discrete element simulations of granular assemblies. *Granular Matter*, 7(1):31–43, 2005.

[16] T. T. Ng and C. Wang. Comparison of a 3-D DEM simulation with MRI data. *International Journal for Numerical and Analytical Methods in Geomechanics*, 25(5):497–507, 2001.

[17] Yanrong Fu. *Experimental Quantification and DEM Simulation of Micro-Macro Behaviors of Granular Materials Using X-ray Tomography Imaging*. PhD thesis, University of Louisiana, Baton Rouge, LA, 2005.

[18] G. Jin. *Physics-Based Modeling of Sedimentary Rock Formation and Prediction of Transport Properties*. PhD thesis, University of California, Berkeley, CA, 2006.

[19] K. Bagi. Analysis of microstructural strain tensors for granular assemblies. *International Journal of Solids and Structures*, 43(10):3166–3184, 2006.

[20] J. Christoffersen, M. M. Mehrabadi, and S. Nemat-Nasser. A micromechanical description of granular material behavior. *Journal of Applied Mechanics*, 48(2):339–344, 1981.

[21] D. L. Johnson, L. M. Schwartz, D. Elata, J. G. Berryman, B. Hornby, and A. N. Norris. Linear and nonlinear elasticity of granular media: stress-induced anisotropy of a random sphere pack. *Journal of Applied Mechanics*, 65:380–388, 1998.

[22] I. Goldenhirsch and C. Goldenberg. Stress in dense granular materials. In H. Hinrichsen and D. E. Wolf, editors, *The Physics of Granular Media*. Wiley-VCH, 2005.

[23] H. A. Makse, N. Gland, D. L. Johnson, and L. M. Schwartz. Why effective medium theory fails in granular materials. *Physical Review Letters*, 83(24):5070–5073, 1999.

[24] R. N. Yong. *Soil properties and behaviour*. Developments in geotechnical engineering. Elsevier Scientific Pub. Co., Amsterdam; New York, 1975.

[25] D. J. Hart and H. F. Wang. Laboratory measurements of a complete set of poroelastic moduli for Berea sandstone and Indian limestone. *Journal of Geophysical Research*, 100(B9):17741–17751, 1995.

[26] Jyh-Chau Liou and Yii-Wen Pan. Fabric evolution of granular assembly under *K0* loading/unloading. *International Journal for Numerical and Analytical Methods in Geomechanics*, 27(13):1099–1122, 2003.

[27] S. N. Domenico. Elastic properties of unconsolidated porous sand reservoirs. *Geophysics*, 42(7):1339–1368, 1977.

[28] Hezhu Yin. *Acoustic velocity and attenuation of rocks: isotropy, intrinsic anisotropy, and stress-induced anisotropy*. PhD thesis, Stanford University, Stanford, CA, 1993.

[29] Hernan A. Makse, Nicolas Gland, David L. Johnson, and Lawrence Schwartz. Granular packings: nonlinear elasticity, sound propagation and collective relaxation dynamics. *Physical Review E*, 70:061302, 2004.

[30] M. A. Biot and D. G. Willis. The elastic coefficients of the theory of consolidation. *Journal of Applied Mechanics*, 24:594–601, 1957.

[31] Gilles Guerin. *Acoustic and Thermal Characterization of Oil Migration, Gas Hydrates Formation and Silica Diagenesis*. PhD thesis, Columbia University, New York, NY, 2000.

[32] Jonny Rutqvist and George J. Moridis. Numerical studies of geomechanical stability of hydrate-bearing sediments. In *2007 Offshore Technology Conference, 30 April - 3 May*, Houston, TX, 2007.

INTERNATIONAL JOURNAL FOR NUMERICAL AND ANALYTICAL METHODS IN GEOMECHANICS
Int. J. Numer. Anal. Meth. Geomech. (2008)
Published online in Wiley InterScience (www.interscience.wiley.com). DOI: 10.1002/nag.725

Mechanical properties of granular materials: A variational approach to grain-scale simulations

R. Holtzman*,†, D. B. Silin and T. W. Patzek

Department of Civil and Environmental Engineering, University of California, Berkeley, CA 94720, U.S.A.

SUMMARY

The mechanical properties of cohesionless granular materials are evaluated from grain-scale simulations. A three-dimensional pack of spherical grains is loaded by incremental displacements of its boundaries. The deformation is described as a sequence of equilibrium configurations. Each configuration is characterized by a minimum of the total potential energy. This minimum is computed using a modification of the conjugate gradient algorithm.

Our simulations capture the nonlinear, path-dependent behavior of granular materials observed in experiments. Micromechanical analysis provides valuable insight into phenomena such as hysteresis, strain hardening and stress-induced anisotropy. Estimates of the effective bulk modulus, obtained with no adjustment of material parameters, are in agreement with published experimental data. The model is applied to evaluate the effects of hydrate dissociation in marine sediments. Weakening of the sediment is quantified as a reduction in the effective elastic moduli. Copyright © 2008 John Wiley & Sons, Ltd.

Received 29 January 2008; Revised 5 March 2008; Accepted 12 May 2008

KEY WORDS: granular matter; grain-scale simulations; quasi-static deformation; variational approach; micromechanics; hydrate dissociation

1. INTRODUCTION

The mechanical properties of cohesionless granular materials are important in many applications, making them the subject of intensive research [1]. When a granular material undergoes deformation, its bulk response is determined by the interactions among discrete grains. This property makes grain-scale numerical simulations a valuable tool [2–5]. For instance, such simulations provide contact forces in three-dimensions which are currently unavailable from experiments [5], and enable insight into the mechanical response of granular matter [6].

*Correspondence to: R. Holtzman, Department of Civil and Environmental Engineering, University of California, Berkeley, CA 94720, U.S.A.
†E-mail: holtzman@berkeley.edu

Contract/grant sponsor: NETL under DOE; contract/grant number: #DE-FC26-05NT42664

Interactions between grains are modeled by contact laws, relating the loads at the grain contacts to their relative displacements and deformations. For elastic deformations, the force component acting normal to the contact interface can be calculated by the Hertzian model [7], which has been verified by experiments [8]. To evaluate loads related to intergranular friction such as shear, the model by Mindlin and Deresiewicz [9] (M-D) is considered adequate [10]. Since it is cumbersome to implement M-D theory for multiple contacts, simplified versions are used for computations, e.g. [10]. However, simulations show that the normal components of the contact forces dominate many aspects of the bulk response [11–14]. Thus, essential aspects of the mechanics of granular materials can be captured by using a 'frictionless' contact law, accounting for the normal contact forces only [15].

Deformation can be described by a quasi-static model, as a sequence of equilibrium configurations corresponding to incremental changes of the boundary conditions. These configurations are found by using a discrete, grain-scale model. Most grain-scale simulations are based on the discrete element method (DEM) [16]. In DEM, interactions between the grains are treated as a dynamic process, accounting for the grain inertia. The equilibrium configurations are found by numerical integration over time. The tight constraints imposed on the time step used in the integration [17] make DEM simulations time consuming. To accelerate computations and damp grain oscillations, material parameters such as the density of the grains and their contact stiffness are often adjusted [13, 18] to unrealistic values.

In this paper, we present a technique that does not include such adjustments. The input parameters in our model are the sizes, densities and elastic moduli of the grains, obtained from published experiments. We use a quasi-static model, where each load increment is followed by a static equilibrium. The contact forces are determined by the Hertzian model, assuming frictionless contacts. Thus, all forces can be obtained as gradients of a potential field. Employing a variational approach, we seek equilibrium configurations of the grains by minimizing their total potential energy. A variational approach in the context of granular mechanics was proposed in [19, 20].

Three-dimensional (3D) micromechanical analysis is used to demonstrate mechanisms leading to phenomena such as hysteresis and stress-induced anisotropy. Macroscopically, our simulations capture the nonlinear, path-dependent response observed in experiments. With no adjustment of material parameters, our estimates of the effective bulk modulus are in agreement with published experimental data. However, the shear modulus is underestimated; this is attributed to the frictionless contact model employed. Elsewhere [21], we extend our variational approach to account for intergranular friction. This extension produces more accurate predictions of the moduli.

Our model is applied to evaluate the mechanical response to dissociation of gas-hydrates in marine sediments. Hydrate dissociation caused, for instance, by hot fluids produced from deep formations, can destabilize the ocean floor and lead to landslides [22], posing risk to nearby equipment such as offshore platforms. The mechanical properties and structure of hydrate-bearing sediments (HBS) are not well-known, due to difficulties in sampling, imaging and testing [23, 24]. We quantify the degradation of strength in an HBS sample by a reduction in elastic moduli.

The outline of this paper is as follows. Section 2 describes our model and simulation methodology. Grain- and sample-scale observations from our simulations are presented in Section 3. In Section 4, we quantify the effects of hydrate dissociation in marine sediments. We discuss our results in Section 5.

DOI: 10.1002/nag

2. SIMULATING DEFORMATION OF GRANULAR MATERIALS

We simulate loading of cohesionless grains packed in a rectangular container. Load is applied by incremental displacements of the container walls, allowing the grains to reach a static equilibrium. Each equilibrium configuration is computed by minimizing the total potential energy of the pack. The initial conditions are the positions of the grains prior to the simulated test. The positions and orientations of the container walls determine the boundary conditions, from which the strains are evaluated. By applying uniform or different normal strains in three principal directions, we simulate an isotopic or a polyaxial test. A uniaxial test is simulated by loading in a single direction.

2.1. *Grain pack model*

We model granular matter as a heterogeneous, irregular ('random') 3D packing of spherical grains, see Figure 1. Each grain is homogeneous and isotropic. To model heterogenous materials such as clastic sediments, we assign the grain sizes and elastic moduli from a given distribution. The deformations are assumed to be small and localized near the contacts, allowing for the shape of a deformed grain to be approximated by a sphere.

In a fixed coordinate system, the geometry of the pack is fully described by the coordinates of the grain centers and their radii. The orientations of the grains are of no importance under the assumption of frictionless contacts. Thus, for a pack of N grains, each configuration has $3N$ degrees of freedom, i.e. the grain center coordinates. Labeling all grains with a single index, $i=1,2,\ldots,N$, we denote the radius-vector of the center of grain i by $\mathbf{r}_i$. Given a reference configuration in equilibrium, we perturb the boundary conditions, forcing the grains to deform and rearrange to a new equilibrium configuration ('current'). Let $\mathbf{u}_i$ denote the displacement of grain i: $\mathbf{u}_i=\mathbf{r}_i-\mathbf{r}_{i(0)}$, where subscript (0) denotes the reference configuration, see Figure 1. The radius of grain i is R_i, its mass is m_i, and Young's modulus and Poisson's ratio of its material are E_i and ν_i, respectively. Subscript w denotes a boundary wall.

We hypothesize here that in a tight packing, the macroscopic stress is mostly affected by the normal component of the contact forces [11–14]. This assumption is based on the argument that

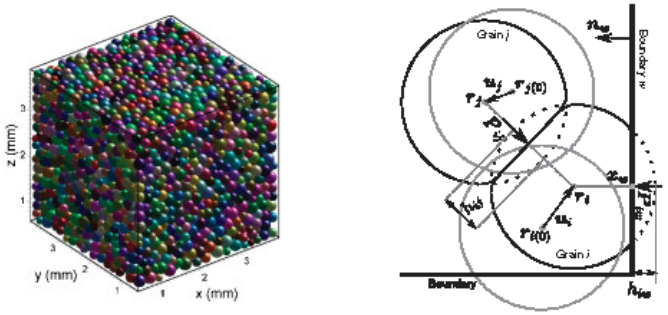

Figure 1. Left: a typical pack with 5036 grains used in the numerical simulations. Right: schematic description of the contact geometry. The reference configuration of the grains is marked with gray dotted lines. The dashed lines show the shapes of the undeformed grains in the current configuration.

DOI: 10.1002/nag

the size of the asperities that resist lateral or angular displacements is much smaller than the size of the grains themselves. Thus, we only account for the normal force components.

2.2. *Contact model: force–displacement relation*

According to Hertzian contact theory [7], the magnitude of the compressive normal force acting at the contact between a pair of grains, i and j, is

$$\|\mathbf{P}_{ij}\| = \tfrac{4}{3} E^*_{ij} (R^*_{ij})^{1/2} (h_{ij})^{3/2} \tag{1}$$

where $\|\mathbf{a}\| = (\mathbf{a}\cdot\mathbf{a})^{1/2}$ is the magnitude of a vector $\mathbf{a}$. Parameters

$$R^*_{ij} = \left(\frac{1}{R_i} + \frac{1}{R_j}\right)^{-1} \quad \text{and} \quad E^* = \left[\frac{(1-\nu_i^2)}{E_i} + \frac{(1-\nu_j^2)}{E_j}\right]^{-1}$$

are the effective radius and elastic coefficient associated with that contact, respectively. Equation (1) is applicable to a grain–boundary contact, by modeling the latter as a grain of infinite radius. The contact deformation is measured by the overlap $h_{ij} \geqslant 0$,

$$\begin{aligned} h_{ij} &= R_i + R_j - \|\mathbf{r}_{ij}\| && \text{for grain–grain contact} \\ h_{iw} &= R_i - (\mathbf{r}_i - \mathbf{x}_w)\cdot\mathbf{n}_w && \text{for grain–boundary contact} \end{aligned} \tag{2}$$

where $\mathbf{r}_{ij} = \mathbf{r}_i - \mathbf{r}_j$, the initial contact point with the wall w is $\mathbf{x}_w$ and $\mathbf{n}_w$ is an inward unit normal to the wall, see Figure 1. As long as the orientation $\mathbf{n}_w$ is held fixed, $\mathbf{x}_w$ can be chosen arbitrarily on the boundary w. The force acting on grain i at the contact with another grain j or a wall w is directed along $\mathbf{r}_{ij}$ or $\mathbf{n}_w$, respectively. No moment relative to the center of the grain is developed.

2.3. *Obtaining equilibrium configurations*

At equilibrium, the balance of forces for each grain yields three scalar equations, a total of $3N$ equations for N grains. The unknowns, grain displacements, can be written as a column vector $\boldsymbol{\theta} = [\mathbf{u}_1 \ldots \mathbf{u}_N]^{\mathrm{T}}$. Here $\mathbf{u}_i$ is a row vector and superscript T is the transpose. The exponent of $\frac{3}{2}$ in Equation (1) makes the system of equations nonlinear.

We seek an equilibrium configuration by employing a variational formulation. Namely, an equilibrium configuration is characterized by a set of displacements $\boldsymbol{\theta}$ corresponding to a minimum of the total potential energy of the pack. This minimum is found numerically using a modification of the conjugate gradient (CG) algorithm [25], see Appendix. The total energy is a function of the deformation (strain energy) and the gravitational energy of the grains. The elastic strain energy of a pair of grains in contact is equal to the sum of work done on each grain to deform it. This work equals the dot product of the force with the displacement increment, integrated over the total displacement. Thus, the strain energy, U_{ij}, stored in the deformed contact region between grains i and j is (cf. Equation (9.15) in [26]):

$$U_{ij}(\mathbf{u}_i, \mathbf{u}_j) = \tfrac{8}{15} E^*_{ij} (R^*_{ij})^{1/2} (h_{ij})^{5/2} \tag{3}$$

DOI: 10.1002/nag

The total potential energy of the pack is the sum of the strain energy of all contacts and the gravitational potentials of all grains

$$\Pi(\boldsymbol{\theta}) = \sum_{i=1}^{N} \left[\frac{1}{2} \sum_{j=1}^{N_g^i} U_{ij} + \sum_{w=1}^{N_b^i} U_{iw} + m_i g (\mathbf{r}_i \cdot \hat{\mathbf{e}}_z - z^*) \right] \tag{4}$$

Here z^* is an arbitrary fixed reference elevation, $\hat{\mathbf{e}}_z$ is a unit vector pointing opposite to the direction of gravity and g is the gravity acceleration. By N_g^i and N_b^i we denote the number of contacts of grain i with other grains and boundaries, respectively. The coordination number of grain i is $N_g^i + N_b^i$. Note that the set of contacts for each grain varies with the deformation of the pack, introducing additional nonlinearity.

The gradient of Π with respect to $\boldsymbol{\theta}$ is a column vector, $\nabla_{\boldsymbol{\theta}} \Pi = -[\mathbf{F}_1 \ldots \mathbf{F}_N]^{\mathrm{T}}$, where the row vector $\mathbf{F}_i$ is the sum of forces on grain i,

$$\mathbf{F}_i = \sum_{j=1}^{N_g^i} \mathbf{P}_{ij} + \sum_{w=1}^{N_b^i} \mathbf{P}_{iw} - m_i g \hat{\mathbf{e}}_z \tag{5}$$

Thus, the vanishing gradient of Π is equivalent to the balance of forces.

2.4. *Initial grain pack generation*

To simulate deformation of a grain pack, a sufficiently dense initial configuration is required [27, 28]. Such an initial configuration could be obtained from a physical sample, using advanced imaging [29, 30]. Alternatively, an initial configuration could be generated numerically using either 'constructive' or 'dynamic' algorithms. Constructive algorithms are based on geometry alone and thus require relatively small computing time; however, these algorithms may produce 3D arrangements with low coordination numbers, gaps or anisotropic structure [28]. In dynamic algorithms, a loose packing is created by placing a relatively small number of grains in a bounded domain. Then, the packing density is increased by either expanding the grains or moving the boundaries closer together. A static equilibrium configuration is found by simulating intergranular interactions, e.g. using DEM. The large number of collisions and grain rearrangements makes such a procedure time-consuming [28].

Instead, we use a quasi-static algorithm. Here, we start by selecting a portion of a pack generated by DEM [31], bounding it with a rectangular domain. This packing is loose, with many grains supported by less than four contacts, rendering them mechanically unstable. To obtain a denser packing we first expand the unstable grains, until their coordination numbers is at least 4. Then, we shrink the pack by displacing its boundaries, and apply our variational algorithm to obtain an equilibrium configuration. This process is repeated until practically all grains have coordination number of 4 or more, and appreciable contact forces develop.

2.5. *Evaluating macroscopic parameters*

2.5.1. Stress and strain. There are several methods for transforming between discrete, grain-scale parameters and continuum, macroscopic stress and strain (e.g. [32, 33]). We consider the pack to be a representative volume of a larger medium, and compute the average stress and strain within this volume as described below.

DOI: 10.1002/nag

The external normal forces applied on the boundaries are calculated from the sum of the contact forces on the container walls. The average normal stresses are evaluated by dividing these external forces by the area of the respective walls. To confirm the validity of our stress evaluation procedure, we also calculate the averaged Cauchy stress, taking into account the entire set of contact forces within the sample volume [32]. This calculation yields values similar to those obtained from our procedure.

To estimate numerically the macroscopic strains, $\boldsymbol{\varepsilon}=[\nabla_{\mathbf{x}}\mathbf{u}+(\nabla_{\mathbf{x}}\mathbf{u})^{\mathrm{T}}]/2$, we replace the derivatives with finite differences. In the last equation, $\mathbf{x}$ is a radius-vector to an infinitesimal volume, and $\mathbf{u}$ is its displacement [26]. For a rectangular domain, the normal strain in the l-direction ($l=1,2,3$) reduces to $[L_l-L_{l(0)}]/L_{l(0)}$, where L_l and $L_{l(0)}$ are the current and the reference (undeformed) length of the domain in that direction, respectively. In our simulations, the strains determine the boundary conditions, enforced by displacing the container walls.

2.5.2. Elastic moduli. To describe the mechanical properties as they evolve with the deformation, we discretize the load path and assign a set of constant effective elastic moduli for each loading interval. The moduli for each interval are evaluated by fitting the stress–strain results with Hooke's law. Hooke's law for a homogeneous, isotropic medium is $\boldsymbol{\sigma}=\lambda\mathrm{tr}(\boldsymbol{\varepsilon})\hat{\mathbf{I}}+2G\boldsymbol{\varepsilon}$, where $\boldsymbol{\sigma}$ is the stress tensor, $\mathrm{tr}(\boldsymbol{\varepsilon})$ is the trace of $\boldsymbol{\varepsilon}$ and $\hat{\mathbf{I}}$ is a identity second-order tensor. The moduli λ and G are Lame's constant and the shear modulus, respectively. Other elastic moduli can be evaluated from λ and G [26].

The moduli evaluated using the procedure above are the bulk-averaged, effective moduli corresponding to an effective homogeneous and isotropic elastic medium. Because the moduli depend on the loads, stress-induced anisotropy can develop when loads in different directions are significantly different [34]. This phenomenon is observed in our simulations, see Section 3.3. To verify whether a grain pack is isotropic, we simulate a polyaxial test and compare the moduli for each pair of principal directions. If they are similar within a given tolerance, we consider the response isotropic. We minimize stress-induced anisotropy by applying relatively isotropic strains, evaluating the moduli at different loads by a uniaxial test.

Macroscopically isotropic systems may exhibit local anisotropy, if the number of grains within the selected volume is too small [15]. To avoid such scale-related anisotropy, we use packs with sides not smaller than $\sim$15 grain diameters. This length scale depends on the properties of the grains and their spatial arrangement, and was determined by trial and error. As a result of using the above measures, the estimates of the moduli in different directions are practically identical.

3. SIMULATIONS

3.1. Model parameters

To verify our model, we compare our simulation results with published experiments. In particular, we compare our results with experiments on glass beads, since they are relatively spherical and smooth. Thus, the elastic moduli of the grains are assigned mean values of $\bar{E}=70\,\mathrm{GPa}$ for Young's modulus and $\bar{\nu}=0.2$ for Poisson's ratio (corresponding to bulk and shear modulus of $\bar{K}=38.9\,\mathrm{GPa}$ and $\bar{G}=29.2\,\mathrm{GPa}$, respectively), similar to glass beads [35]. In other simulations, quartz sand is modeled by assigning $\bar{E}=100\,\mathrm{GPa}$ and $\bar{\nu}=0.15$ ($\bar{K}=47.6\,\mathrm{GPa}$ and $\bar{G}=43.5\,\mathrm{GPa}$) [36, 37]. The elastic moduli are normally distributed with a standard deviation of 10% of the mean. The radii of

DOI: 10.1002/nag

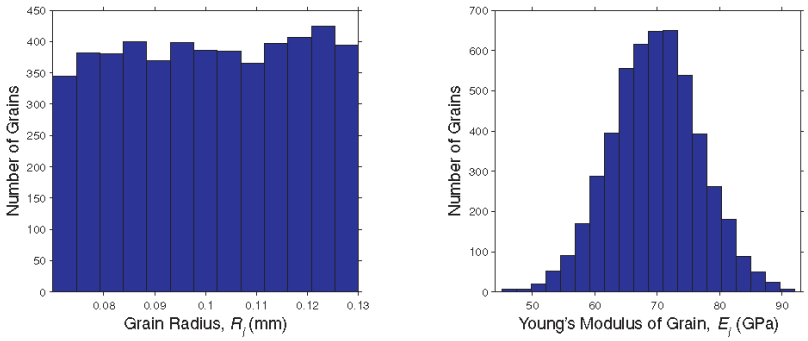

Figure 2. The distribution of grain sizes (left) and Young's modulus values (right) for pack *G5036*, representing a sample made of 5036 glass beads.

the grains used to generate the initial pack are distributed uniformly between 0.07 and 0.13 mm. Since the initial pack generation procedure involves expansion of the unstable grains, the final grain radii slightly deviate from this distribution. The density of glass and quartz grains is taken to be 2.42 and 2.65 g/cm^3 [36]. The number of grains is 5036 and 2654 for the glass beads and quartz sand, denoted by *G5036* and *Q2654*, respectively. The distribution of grain sizes and Young's modulus values for *G5036* are plotted in Figure 2.

3.2. *Macro-mechanical analysis*

3.2.1. Stress–strain. To capture hysteresis and stress-induced anisotropy, we simulated a loading–unloading cycle in a polyaxial test on sample *Q2654*. The porosity and mean coordination number varied as 35.8–30.5% and 7.23–8.26, accordingly, with stresses of $\sim$60–300 MPa. The stress–strain curves calculated for *Q2654* are plotted in Figure 3. The abrupt changes in the slopes are associated with variations in the complex network of contacts ('fabric') and contact forces. Some of these microstructural variations are irreversible, contributing to the hysteretic response observed in experiments [38]. This hysteresis is evident in Figure 3 as different loading and unloading curves.

3.2.2. Elastic moduli. To verify our model against experiments we simulated isotropic compression of sample *G5036*, evaluating the macroscopic elastic moduli for different loads by an incremental uniaxial loading. In these simulations, the porosity and mean coordination number were 37.4–35.1% and 6.24–7.15, accordingly, with confining stresses of $\sim$1–35 MPa. Our moduli estimates are plotted in Figure 4 vs. the confining stress σ_c, defined by the mean of the lateral stresses perpendicular to the principal loading direction. Figure 4 also shows results of acoustic experiments, DEM simulations and effective medium theory (EMT) by [35, 36, 39] using glass bead samples with micro-properties similar to those used in our simulations. The DEM and EMT calculations in [35] employed a contact law that prohibits sliding of grains, i.e. assigning infinitely large intergranular friction.

Our bulk modulus (K) estimates are in good agreement with the published experimental data, with some values slightly lower than the data. In addition, except at $\sigma_c < 2$ MPa, our evaluated shear modulus (G) growth agrees with the experimental data, showing faster growth rate than the power

DOI: 10.1002/nag

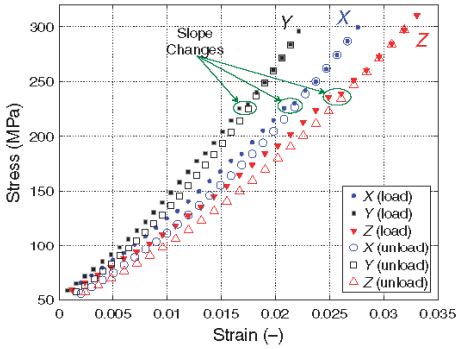

Figure 3. Stress–strain curves obtained from the simulations of a polyaxial loading–unloading cycle on sample *Q2654*. Hysteresis is evident as different loading and unloading curves. This hysteresis is related to the abrupt change in the slopes (encircled).

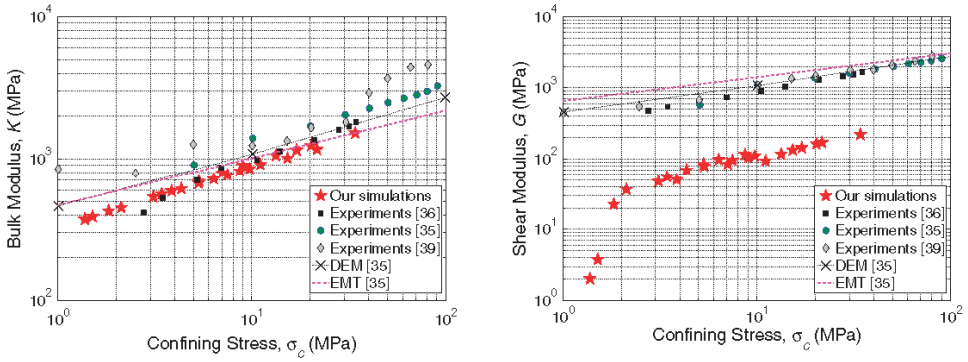

Figure 4. The effective bulk (left) and shear (right) modulus vs. confining stress, σ_c. The evaluated moduli from simulations on sample *G5036* are compared with published results of acoustic experiments in glass beads [35, 36, 39], in addition to DEM and effective medium theory (EMT) predictions [35]. The numerical values of data from [35, 39] have been obtained by digitizing Figure 1 in [35].

law $\sigma_c^{1/3}$ predicted by EMT [40]. The discrepancy between the EMT predictions and experimental data is discussed in [35, 41, 42].

At the same time, our shear modulus strongly underestimates the experimental data. In particular, the evaluated shear modulus drops sharply at low stresses. Loss of shear rigidity is observed as the mean coordination number approaches 6 and the porosity exceeds $\sim$37%. However, loss of rigidity is expected to occur at lower packing densities, as intergranular friction strengthens the pack [43]. We associate the discrepancies between our predictions and the data with the frictionless contact assumption. Unlike the bulk modulus, the shear modulus greatly depends on intergranular shear [43].

DOI: 10.1002/nag

3.3. *Micromechanical analysis*

Relating grain-scale parameters to macroscopic, continuum parameters can improve our understanding of the complex behavior of granular materials [14]. The effect of the spatial distribution of grain-scale parameters cannot be captured by averaged, macroscopic quantities. For example, by tracking the contact forces larger than a certain threshold, we observe force chains, as most of the load is carried by relatively few grains. This can lead to fracturing and failure of the material, which cannot be predicted from the average stress. Force chains have been observed in experiments using photoelastic disks (e.g. [44] and references within) and in DEM simulations (e.g. [3, 6, 12, 15, 43]).

Correspondence between abrupt changes in the slopes of the stress–strain curves and substantial variations in the contact network and the force chains is noticed in our simulations. A similar correlation was observed between deviator stress drops and microstructural variations [3]. Some of these variations are irreversible, contributing to the hysteretic bulk response. Tracking hysteresis via grain-scale parameters can be performed quantitatively using the fabric tensor [38]. Qualitatively, we observe that these noticeable variations are correlated to relatively large displacements experienced by several grains. These displacements are possible at particular combinations of contact forces and geometry, as grains are 'pushed' through constrictions. Following such events, the local sets of contacts and the shapes of these constrictions are altered significantly, so that a reverse perturbation of the boundary conditions cannot restore the original configuration. In loading, these rearrangements create an overall stiffer pack, which may be interpreted as strain hardening.

Stress-induced anisotropy is observed in simulations of highly anisotropic loading on sample *Q2654*. To investigate the mechanisms leading to such anisotropy, we analyzed the directions of the contact forces that were larger than the mean. Under isotropic loads these directions are uniformly distributed. In contrast, under anisotropic loads corresponding to anisotropic moduli, these forces are preferentially aligned with the main loading direction. Similar observations were made from experiments [44] and simulations [12].

4. IMPACT OF HYDRATE DISSOCIATION IN MARINE SEDIMENTS

4.1. *Modeling hydrate dissociation*

We apply our model to quantify the mechanical response to hydrate dissociation in HBS. Gas-hydrates are solid materials formed under a range of high pressures and low temperatures. Dissociation converts them into liquid water and free gas. The volumetric expansion of gas can lead to an appreciable increase in pore pressure [22], reducing the effective stress. Thus, dissociation impacts the mechanical properties of HBS by reducing both the solid fraction of the sediment and the effective stress. We quantify the effect of dissociation via the evolution of elastic moduli.

The pressure increase varies with factors such as dissociation rate, sediment permeability and initial pore pressure [22]. Predicting the excess pressure as a function of dissociation is outside the scope of this paper. Here, we consider a number of dissociation scenarios. A range of dissociation amounts and excess pressures, taken from other models [22], is used as input parameters in our simulations.

The distribution of hydrates within the pore space depends on their formation mechanism, among other factors, and a variety of distribution models exists [23]. To model interactions between the host sediment and the hydrate, we consider methane-hydrate formed preferentially in the larger

DOI: 10.1002/nag

pores, rather than in the pore-throats. This type of hydrate distribution can occur if small amounts of hydrate are slowly introduced in the aqueous phase [24]. Such a distribution makes hydrates a part of the solid skeleton, i.e. load-bearing solid particles.

We quantify the amount of dissociation by the decrease in hydrate saturation, from S to $S+\Delta S$, where $\Delta S<0$. The hydrate saturation is $S=V^{\mathrm{h}}/V$, where V^{h} is the volume occupied by hydrate and V is the total pore volume (including the hydrates). We model the reduction in solid fraction due to dissociation by shrinking the hydrate grains, assuming that all grains experience similar volumetric strains. The impact of the excess pore pressure, p_{ex}, is modeled at both the grain and the sample level. We assume uniform pore pressure within the sample. Since the contact area is much smaller than the surface area of the grains, we isotropically compress the grains, neglecting the net force applied by the fluid pressure. The volume of grain i, V_i, is changed by $\Delta V_i<0$. For small changes in volume, $\Delta V_i/V_i$ is approximately equal to the volumetric strain, and can be determined by $p_{\mathrm{ex}}=-K_i\Delta V_i/V_i$. Here K_i is the bulk modulus of grain i. At the sample scale, the reduction in effective stress is modeled by applying a tensile macroscopic strain, $\varepsilon_{kk}>0$, expanding the sample isotropically. This strain is determined from the poroelastic constitutive equation $\alpha_{\mathrm{b}}p_{\mathrm{ex}}=K\varepsilon_{kk}$, where α_{b} is the Biot–Willis coefficient [45].

4.2. *Elastic moduli following hydrate dissociation*

The initial state of an HBS sample is modeled as a dense arrangement of 2740 spherical grains, where some of the smallest grains are methane-hydrate. Hydrates are assigned the elastic moduli of $E_i=6.6\,\mathrm{GPa}$ and $\nu_i=0.32$ ($K_i=6.1\,\mathrm{GPa}$ and $G_i=2.5\,\mathrm{GPa}$), and a density of $0.9\,\mathrm{g/cm^3}$ [46]. To model quartz sand as the host sediment, the other grains are assigned the properties of quartz, see Section 3.1, and $\alpha_{\mathrm{b}}=0.8$ [47]. The initial porosity and hydrate saturation are $\phi\approx 45\%$ and $S=0.215$. The effective stress for this state, determined from the contact forces on the walls (see Section 3.2.1), is $\sim 21\,\mathrm{MPa}$. The initial pore pressure may be larger than hydrostatic pressure if the sediment is confined by a low-permeability layer. The resulting total stress, which is considered fixed in our simulations, can exceed the lithostatic stress if the sediment carries the weight of a nearby offshore platform.

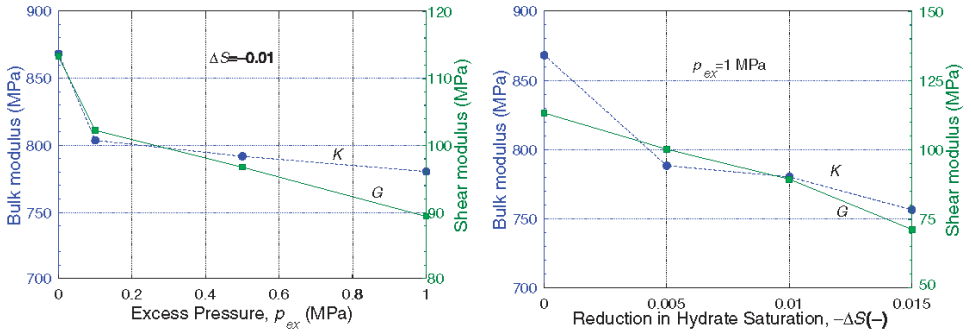

Figure 5. Reduction in bulk (dashed line) and shear (solid line) modulus vs. hydrate dissociation. Left: increasing excess pore pressure, p_{ex}, for a fixed saturation decrement, $\Delta S=-0.01$. Right: decreasing the saturation for a fixed excess pressure, $p_{\mathrm{ex}}=1\,\mathrm{MPa}$.

DOI: 10.1002/nag

By varying the excess pressure and the saturation decrement independently, we produce a series of configurations, covering a range of possible scenarios. For each configuration, the elastic moduli are evaluated by simulating a uniaxial test. In Figure 5 (left), these moduli are plotted against the excess pressure, for a fixed saturation decrement, $\Delta S = -0.01$. Conversely, Figure 5 (right) shows the moduli vs. ΔS, for a fixed excess pressure $p_{\text{ex}} = 1\,\text{MPa}$. The initial moduli prior to dissociation are plotted in the left-most parts of both figures.

Weakening of HBS is evident from a reduction in elastic moduli, as the sediment becomes looser and softer. This observation is in qualitative agreement with experiments [23, 24] and other numerical simulations [48]. Further dissociation may lead to a significant decrease in the solid support, with a possible loss of shear rigidity. In such a state, the sediment is more susceptible to landslides and subsidence, threatening the safety of adjacent offshore platforms.

5. DISCUSSION

A technique for estimating the mechanical properties of cohesionless granular materials from numerical simulations has been presented. We model granular matter as a 3D disordered packing of elastic spherical grains, bounded by a rectangular container. Using a quasi-static model, the pack is loaded by incremental displacements of the container walls. The contact forces are calculated using Hertzian contact theory. Each equilibrium configuration is found by minimizing the total potential energy of the system. A modification of the CG algorithm is used to obtain this minimum. This approach results in an efficient computational procedure, which is also used to generate a dense initial arrangement.

By micromechanical analysis we demonstrate mechanisms responsible for hysteresis, strain hardening and stress-induced anisotropy. Macroscopically, our results capture the nonlinear and path-dependent response observed in experiments. We have verified our physics-based model against published experimental data, using similar grain properties. All material parameters used in simulations are obtained from published experiments. The good agreement between predicted and measured values of the macroscopic bulk modulus is achieved with no adjustments of parameters.

These results confirm that the normal contact forces play an important role in determining the overall response, and that grain-scale elasticity is suitable to describe many features of the inelastic response of granular materials. The bulk modulus, for example, mainly depends on the normal contact forces, which are adequately described by the Hertzian theory. Nevertheless, our model underestimates the shear modulus. We attribute this deficiency to the frictionless contact model employed. Extension of our variational approach to account for shear and sliding at the contacts provides more accurate predictions of the moduli [21].

We apply our model to quantify the effect of hydrate dissociation in marine sediments. Hydrates are modeled as load-bearing solid particles within the pores. To model dissociation, we reduce the solid fraction by shrinking the hydrate grains. The effect of the related excess pore pressure is modeled by expanding the sample to account for the decrement of effective stress and compressing the grains. A series of possible dissociation scenarios has been simulated, showing degradation in sediment strength as a reduction in the macroscopic elastic moduli. This trend agrees qualitatively with the published results of experiments and simulations. Further dissociation might lead to loss of solid support of the skeleton, causing seafloor landslide and subsidence. To predict such instabilities and their impact on offshore platforms, our model can be used to provide constitutive

DOI: 10.1002/nag

relationships for large-scale simulations (e.g. [48]). To quantitatively verify our predictions, more experimental data are required.

APPENDIX A: MINIMIZATION ALGORITHM

Each equilibrium configuration is found numerically, using a modified CG algorithm. We seek displacements $\boldsymbol{\theta}$, which provide a local minimum of the functional Π. Iterative updates $\boldsymbol{\theta}^{k+1} = \boldsymbol{\theta}^k - \alpha^k \mathbf{p}^k$ are performed until the displacements converge to provide a local minimum of Π within a desired accuracy. Superscript k denotes the iteration index. The updates are performed in the so-called search directions $\mathbf{p}^k = \mathbf{R}^k - \beta^k \mathbf{p}^{k-1}$, where $\beta^k = -(\|\mathbf{R}^k\|/\|\mathbf{R}^{k-1}\|)^2$. The residual vector $\mathbf{R}^k$ equals the gradient of Π, $\mathbf{R}^k = -[\mathbf{F}_1^k \ldots \mathbf{F}_N^k]^{\mathrm{T}}$.

We use the steepest descent method, finding a value for the scaling coefficient α^k, which provides a minimum for $\Pi(\boldsymbol{\theta}^k - \alpha^k \mathbf{p}^k)$. To avoid nonphysical artifacts such as grain permutations, the value of α is restricted within each iteration. The iterations are stopped if at least one of the following holds true:

$$\Pi^k - \Pi^{k+1} < \varepsilon_1 \Pi^k \quad \text{or} \quad \|\mathbf{R}^{k+1}\|^2 < \varepsilon_2 N (\bar{E}\bar{R}^2)^2 \tag{A1}$$

where $\bar{R}$ is the mean grain radius. For example, for sample *Q2654*, $\bar{E} = 10^{11}$ Pa and $\bar{R} = 1.003 \times 10^{-4}$ m. The tolerance parameters were chosen to be $\varepsilon_1 = 10^{-10}$ and $\varepsilon_2 = 10^{-3}$. These values provide for each grain a residual force $\mathbf{F}_i$, which was smaller than the maximum contact force on that grain by at least 3 orders of magnitude. Note that due to inevitable round-off error, the chosen tolerance cannot be arbitrarily small.

For a linear system of the order $3N$ with a positive-definite matrix, CG is proven to yield an exact solution within $3N$ iterations [25]. However, the nonlinearities related to the force–displacement relation and variations in the fabric, in addition to accumulated round-off error, may cause loss of convergence, as updating $\boldsymbol{\theta}^k$ in the direction of $\mathbf{p}^k$ may not reduce the value of Π. To avoid this behavior, we refresh the CG algorithm by performing an update in the direction of the gradient $\mathbf{R}^k$. The frequency of this operation is determined by trial-and-error.

ACKNOWLEDGEMENTS

This work was supported by the Assistant Secretary for Fossil Energy, Office of Natural Gas and Petroleum Technology, through the National Energy Technology Laboratory, under the U.S. Department of Energy, Contract #DE-FC26-05NT42664.

REFERENCES

1. Bagi K. Granular mechanics special issue. *International Journal of Solids and Structures* 2004; **41**(21):5761–5762.
2. Kruggel-Emden H, Simsek E, Rickelt S, Wirtz S, Scherer V. Review and extension of normal force models for the discrete element method. *Powder Technology* 2007; **171**(3):157–173.
3. Peña AA, Lizcano A, Alonso-Marroquin F, Herrmann HJ. Biaxial test simulations using a packing of polygonal particles. *International Journal for Numerical and Analytical Methods in Geomechanics* 2008; **32**(2):143–160.
4. Walsh SDC, Tordesillas A, Peters JF. Development of micromechanical models for granular media. *Granular Matter* 2007; **9**(5):337–352.
5. Cole DM, Peters JF. A physically based approach to granular media mechanics: grain-scale experiments, initial results and implications to numerical modeling. *Granular Matter* 2007; **9**(5):309–321.

DOI: 10.1002/nag

6. Radjai F, Jean M, Moreau JJ, Roux S. Force distributions in dense two-dimensional granular systems. *Physical Review Letters* 1996; **77**(2):274–277.
7. Hertz H. Über die berührung fester elastischer körper (on the contact of elastic solids). *Journal reine und angewandte Mathematik* 1882; **92**:156–171. In German.
8. Johnson KL. *Contact Mechanics*. Cambridge University Press: Cambridge, MA, 1987.
9. Mindlin RD, Deresiewicz H. Elastic spheres in contact under varying oblique forces. *Journal of Applied Mechanics* 1953; **20**:327–344.
10. Vu-Quoc L, Zhang X. An accurate and efficient tangential force–displacement model for elastic frictional contact in particle-flow simulations. *Mechanics of Materials* 1999; **31**(4):235–269.
11. Rothenburg L, Bathurst RJ. Analytical study of induced anisotropy in idealized granular-materials. *Géotechnique* 1989; **39**(4):601–614.
12. Thornton C, Antony SJ. Quasi-static deformation of particulate media. *Philosophical Transactions of the Royal Society A: Mathematical, Physical and Engineering Sciences* 1998; **356**(1747):2763–2782.
13. Thornton C. Numerical simulations of deviatoric shear deformation of granular media. *Géotechnique* 2000; **50**(1):43–53.
14. Kruyt NP, Antony SJ. Force, relative-displacement, and work networks in granular materials subjected to quasistatic deformation. *Physical Review E* 2007; **75**(5):051308.
15. Goldenhirsch I, Goldenberg C. Stress in dense granular materials. In *The Physics of Granular Media*, Hinrichsen H, Wolf DE (eds). Wiley-VCH: New York, 2005.
16. Cundall PA, Strack ODL. A discrete numerical model for granular assemblies. *Géotechnique* 1979; **29**:47–65.
17. O'Sullivan C, Bray JD. Selecting a suitable time-step for discrete element simulations that use the central difference time integration approach. *Engineering Computations* 2004; **21**(2–4):278–303.
18. O'Sullivan C, Bray JD, Riemer M. Examination of the response of regularly packed specimens of spherical particles using physical tests and discrete element simulations. *Journal of Engineering Mechanics* 2004; **130**(10): 1140–1150.
19. O'Hern CS, Silbert LE, Liu AJ, Nagel SR. Jamming at zero temperature and zero applied stress: the epitome of disorder. *Physical Review E* 2003; **68**(1):011 306.
20. Renouf M, Alart P. Conjugate gradient type algorithms for frictional multi-contact problems: applications to granular materials. *Computer Methods in Applied Mechanics and Engineering* 2005; **194**:2019–2041.
21. Holtzman R, Silin DB, Patzek TW. Deformations of sediments via grain-scale simulations: a quasi static approach. *EOS Transactions, American Geophysical Union, Fall Meeting Supplement* 2007; **88**(52):Abstract T43E-04.
22. Xu W, Germanovich LN. Excess pore pressure resulting from methane hydrate dissociation in marine sediments: a theoretical approach. *Journal of Geophysical Research* 2006; **111**:B01 104.
23. Durham W, Stern L, Kirby S, Circone S. Rheological comparisons and structural imaging of sI and sII endmember gas hydrates and hydrate/sediment aggregates. *Proceedings of the 5th International Conference on Gas Hydrates*, 26–29 September 2004, Trondheim, Norway, 2005.
24. Yun TS, Santamarina JC, Ruppel C. Mechanical properties of sand, silt, and clay containing tetrahydrofuran hydrate. *Journal of Geophysical Research* 2007; **112**:B04 106.
25. Press WH, Flannery BP, Teukolsky SA, Vetterling WT. *Numerical Recipes in Fortran 77*. Cambridge University Press: New York, 1986.
26. Landau LD, Lifshitz EM. *Theory of Elasticity*. Course of Theoretical Physics, vol. 7, Elsevier: Burlington, MA, 1986.
27. O'Sullivan C. The application of discrete element modelling to finite deformation problems in geomechanics. *Ph.D. Thesis*, University of California, Berkeley, CA, 2002.
28. Bagi K. An algorithm to generate random dense arrangements for discrete element simulations of granular assemblies. *Granular Matter* 2005; **7**(1):31–43.
29. Ng TT, Wang C. Comparison of a 3-D DEM simulation with MRI data. *International Journal for Numerical and Analytical Methods in Geomechanics* 2001; **25**(5):497–507.
30. Fu Y. Experimental quantification and DEM simulation of micro–macro behaviors of granular materials using x-ray tomography imaging. *Ph.D. Thesis*, University of Louisiana, Baton Rouge, LA, 2005.
31. Jin G. Physics-based modeling of sedimentary rock formation and prediction of transport properties. *Ph.D. Thesis*, University of California, Berkeley, CA, 2006.
32. Christoffersen J, Mehrabadi MM, Nemat-Nasser S. A micromechanical description of granular material behavior. *Journal of Applied Mechanics* 1981; **48**(2):339–344.
33. Bagi K. Analysis of microstructural strain tensors for granular assemblies. *International Journal of Solids and Structures* 2006; **43**(10):3166–3184.

DOI: 10.1002/nag

34. Johnson DL, Schwartz LM, Elata D, Berryman JG, Hornby B, Norris AN. Linear and nonlinear elasticity of granular media: stress-induced anisotropy of a random sphere pack. *Journal of Applied Mechanics* 1998; **65**:380–388.
35. Makse HA, Gland N, Johnson DL, Schwartz LM. Why effective medium theory fails in granular materials. *Physical Review Letters* 1999; **83**(24):5070–5073.
36. Domenico SN. Elastic properties of unconsolidated porous sand reservoirs. *Geophysics* 1977; **42**(7):1339–1368.
37. Yong RN. *Soil Properties and Behaviour*. Developments in Geotechnical Engineering. Elsevier: Amsterdam, New York, 1975.
38. Liou JC, Pan YW. Fabric evolution of granular assembly under $K0$ loading/unloading. *International Journal for Numerical and Analytical Methods in Geomechanics* 2003; **27**(13):1099–1122.
39. Yin H. Acoustic velocity and attenuation of rocks: isotropy, intrinsic anisotropy, and stress-induced anisotropy. *Ph.D. Thesis*, Stanford University, Stanford, CA, 1993.
40. Walton K. The effective elastic moduli of a random packing of spheres. *Journal of the Mechanics and Physics of Solids* 1987; **35**:213–226.
41. Goddard JD. Nonlinear elasticity and pressure-dependent wave speeds in granular media. *Proceedings of the Royal Society of London, Series A* 1990; **430**:105–131.
42. Pride SR. Relationships between seismic and hydrological properties. In *Hydrogeophysics*, Rubin Y, Hubbard S (eds). Springer: Dordrecht, The Netherlands, 2005.
43. Makse HA, Gland N, Johnson DL, Schwartz L. Granular packings: nonlinear elasticity, sound propagation and collective relaxation dynamics. *Physical Review E* 2004; **70**:061 302.
44. Majmudar TS, Behringer RP. Contact force measurements and stress-induced anisotropy in granular materials. *Nature* 2005; **435**:1079–1082.
45. Biot MA, Willis DG. The elastic coefficients of the theory of consolidation. *Journal of Applied Mechanics* 1957; **24**:594–601.
46. Guerin G. Acoustic and thermal characterization of oil migration, gas hydrates formation and silica diagenesis. *Ph.D. Thesis*, Columbia University, New York, NY, 2000.
47. Hart DJ, Wang HF. Laboratory measurements of a complete set of poroelastic moduli for Berea sandstone and Indian limestone. *Journal of Geophysical Research* 1995; **100**(B9):17 741–17 751.
48. Rutqvist J, Moridis GJ. Numerical studies of geomechanical stability of hydrate-bearing sediments. *2007 Offshore Technology Conference*, 30 April–3 May, Houston, TX, 2007.

DOI: 10.1002/nag

National Energy Technology Laboratory

626 Cochrans Mill Road
P.O. Box 10940
Pittsburgh, PA 15236-0940

3610 Collins Ferry Road
P.O. Box 880
Morgantown, WV 26507-0880

One West Third Street, Suite 1400
Tulsa, OK 74103-3519

1450 Queen Avenue SW
Albany, OR 97321-2198

2175 University Ave. South
Suite 201
Fairbanks, AK 99709

Visit the NETL website at:
www.netl.doe.gov

Customer Service:
1-800-553-7681